UC San Diego

UC San Diego Electronic Theses and Dissertations

Title

T_2 tunable porous silicon iron oxide nanocomposites for magnetic resonance imaging guided drug delivey

Permalink

https://escholarship.org/uc/item/46q0690f

Author

Ananda Yogendran, Shalini

Publication Date

2012

Peer reviewed|Thesis/dissertation

eScholarship.org Powered by the California Digital Library
University of California

UNIVERSITY OF CALIFORNIA, SAN DIEGO

T_2 TUNABLE POROUS SILICON IRON OXIDE NANOCOMPOSITES FOR MAGNETIC RESONANCE IMAGING GUIDED DRUG DELIVERY

A dissertation submitted in partial satisfaction of the requirements for the degree

Doctor of Philosophy

in

Materials Science and Engineering

by

Shalini Ananda Yogendran

Committee in charge

Professor Robert F. Mattrey, Chair
Professor Michael J. Sailor, Co-Chair
Professor Sadik C. Esener
Professor Nathan C Gianneschi
Professor Rebecca J Thielmann
Professor Liangfang Zhang

2012

Copyright

Shalini Ananda Yogendran, 2012

All rights reserved

The dissertation of Shalini Ananda Yogendran is approved, and it is acceptable in quality and form for publication on microfilm and electronically:

_____

_____

_____

_____

_____

_____

University of California, San Diego

2012

DEDICATION

To my Grandfather

TABLE OF CONTENTS

Signature Page……...…iii

Dedication……..…..…iv

Table of Contents……..…...v

List of Abbreviations……...…..viii

List of Figures…….….….ix

List of Tables……..……...….….xii

Acknowledgements……..….….xiii

Vita…….….….xiv

Abstract of the Dissertation…….……..…….……..xv

Chapter 1. Introduction……..…..1

1.1 Scope…….….….2

1.2 Image guided drug delivery: Towards personalized medicine…….……..3

1.3 Nanosystems for image guided drug delivery……...…5

1.4 Porous silicon based theranostic nanoparticles……..10

1.5 Iron oxide based theranostic nanoparticles……11

1.6 Magnetic resonance imaging……20

1.7 Objectives of the thesis……...…31

Chapter 2. Toolbox…….38

2.1 Purpose…….……...…….39

2.2 Materials……41

2.3. Computational Tools……..51

2.4 MRI and NMR Tools……...58

Chapter 3. Constructing Iron oxide aggregates to increase R2* relaxation rate: A Monte Carlo Study……..…71

3.1 Abstract……..……...72

3.2 Introduction……...73

3.3 Theory……..…….……76

3.4 Methods……..……..…….……..….82

3.5 Results and discussion…….……..……84

3.6 Conclusion ……..…….90

Chapter 4. A mesoporous matrix for tuning R_2 AND R_2* properties of superparamagnetic iron oxide aggregates …….……...96

4.1 Abstract……..……..……97

4.2 Introduction…….……..……98

4.3 Methods……..…102

4.4 Results and Discussion……107

4.5 Conclusion……..…117

Chapter 5. T2 tunable biodegradable nanocomposites for quantifying drug release on nuclear magnetic resonance imaging……..……...122

5.1 Abstract……...123

5.2 Introduction……124

5.3 Methods……..129

5.4 Results and discussion …….…...134

5.5 Conclusion……..……139

CHAPTER 6. Conclusion and Future Directions…….……...145

6.1 CONCLUSION……...146

6.2 Future Directions: Improvements to chemical design of contrast agents….158

6.3 Potential applications: Applying physiologically based pharmacokinetic modeling towards screening contrast agents…….....162

6.4 Potential application of porous silicon iron oxide nanocomposites for diagnosis and treatment for diseases……..……163

Appendix……...……181

LIST OF ABBREVIATIONS

MRI	Magnetic Resonance Imaging
IGDD	Image Guided Drug Delivery
T2	Transverse relaxation time
R2	Relaxation rate
r2	Relaxivity coefficient
pSi	Porous silicon
pSiNC	Porous Silicon Iron oxide nanocomposite
PEG	Poly Ethylene Glycol
T2*	Transverse relaxation
R2*	Transverse relaxation rate
MAR	Motion averaged regime
SDR	Static dephasing regime
EPR	Enhanced permeation and retention
HPLC	High performance liquid chromatography
SPIO	Superparamagnetic iron oxide
IONP	Iron oxide nanoparticle
SEM	Scanning Electron Microscope
TEM	Transmission Electron Microscpe
STEM	Scanning Transmission Electron Microscope

LIST OF FIGURES

Figure 1.1: Inverse spinel structure of magnetite (a) The front side of the cube is shown(b) Ferrimagnetic organization in magnetite……..…..13
Figure 1.2: Model of uniaxial anisotropy for a magnetite (or maghemite) nanoparticle. The graph shows the probability of alignment of the magnetic moment in one direction with respect to the angle between this direction and the anisotropy axis(for sphere with a radius R =5nm and an anisotropy constant =K =13,500Jm− 3)……..……13
Figure 2.1: This is a representation of iron oxide synthesized via thermal decomposition. The average size of the above nanoparticles were calculated to be 9.6nm. A plug-in on Image J was used to calculate average size of the nanoparticles ……..……45
Figure 2.2 Schematic of the etch cell used to prepare porous silicon……48
Fig. 2.3 Mechanism of Si oxidation during the formation of porous Si……..…49
Figure 2.4 SEM images of a) size distribution of porous silicon nanoparticles b) Porous nanostructure of porous silicon (average pore size of 18.7nm)…….....…49
Figure 2.5 describes the main variables measured from the projected image to infer three dimensional structural properties……..……...56
Figure 2.6 A CPMG sequence to measure T2……..66
Figure 3.1: In this figure, Plot a describes the R2* of 9nm nanoparticles constructed in a linear configuration in sets of 1, sets of 2 and sets of 3. The linear configuration is described by particles whose centers are collinear to each other. In Plot b, we compare nanoparticles in a circular configuration arranged in sets of 1, sets of 2 and sets of 3. The angle between the centers of neighboring nanoparticles in the aggregate is 45^0. Plot c explores the transition from motion averaged regime to the static dephasing regime and R2* is presented as each set is added to the system. Plot d describes the maximum number of particle in each of the geometrical configurations describe to exit the MAR. The fractal dimensions for all structures were calculated separately using methods described previously……..……..……...91
Figure 3.2 Plot a describes the simulated R2* of different aggregate constructed to experience a relaxation mechanism between MAR and SDR. Plot b describes the static limit or the transition from MAR to SDR in a system where the number aggregates in the system was increased……..……..…….92
Figure 4.1: a) This plot describes the percentage drop in R2* once the thickness of coating (oleic acid and polyethylene glycol) of iron oxide nanoparticles is increased as observed via simulation with particle of radius 9nm.Oleic acid was assumed to be impermeable and polyethylene glycol has a D_i/D_0 of 0.1 where D_0 of $2.5x10^{-9}m^2/s$ b) This figure describes the modeling process of protons in a porous silicon cylindrical matrix. The pore size of the materials are 15nm and 23 nm on average according nuclear magnetic resonance spectrosocopy. c) R2* and R2 values of a cluster of nanoparticles were simulated at different diffusion coefficient. For this simulation, M = 2.58 x 10^5 T/m^3 and f = 3.14 x 10^{-6}. The

simulations show a diffusion coefficient of 0.2 as the optimal diffusion coefficient. The simulations were done with r =9nm and a D_0 of $2.5x10^{-9}m^2/s$. d) This plot describes the simulation results for R2 and R2* in a scenario where nanoparticles were systematically added to a system. The fractal dimension for pSi23 was calculated to be 2.2 and pSi15 to be 1.6 for sets of 2-3 nanoparticles. A fractal dimension of 1.6 suggests collinear chains with overall moderate compaction, as per analysis of microscopy images ……..107
Figure 4.2 a) This plot describes the % iron oxide released from porous silicon iron oxide nanocomposites at room temperature with different pore sizes as measured by ICP-OES. This evidence accounts for the complete degradation of both materials in a time frame of 8 hours b) The schematic describes the release of iron oxide following the degradation of the porous silicon matrix. c) This plot describes the MR relaxation measurements performed at 0hr and 8hr after degradation at 3T d) The increase in number of aggregates was simulated by increasing the volume fraction as a proportion to the number of aggregates.……..……..…..108
Figure 5.1 : Plot a describes the change in size as the nanocomposite degrades, the hydrodynamic diamter was measured by Dynamic Light scattering at different points during the degradation process. b) This plot describes the percentage porous silicon degrades at 37C in PBS in the time frame of 0-24 hours. The degradation profile for porous silicon and porous silicon iron oxide nanocomposites were compared. c) This plot describes the release of iron during the degradation process as measured by ICP-OES. The ratio of pSi: Fe304 in the nanocomposite and the % of iron released from pSi were shown in this figure…..……..….140
Figure 5.2 Plot a describes the change in size as the nanocomposite degrades, the hydrodynamic diamter was measured by Dynamic Light scattering at different points during the degradation process. b) This plot describes the percentage porous silicon degrades at 37C in PBS in the time frame of 0-24 hours. The degradation profile for porous silicon and porous silicon iron oxide nanocomposites were compared. c) This plot describes the release of iron during the degradation process as measured by ICP-OES. The ratio of pSi: Fe304 in the nanocomposite and the % of iron released from pSi were shown in this figure……140
Figure 5.3: a) This schematic describes the change in regime experienced by protons confined within a porous silicon matrix before and after degradation. b) describes the change in r2 once the nanocomposites degrade in the presence of water at 37^0C. The r2 of degraded nanocomposites were compared against degraded nanocomposites……..……..…141

Figure 5.4 a) This figure shows the percentage change in r2 with percentage sorafenib tosylate released over 8 hours. b) The direct relationship between percentage sorafenib tosylate released and percentage change in r2 is shown here. c) This figure shows the percentage change in r2 and percentage change in 5-fluorouracil released over time. d) The direct relationship between percentage 5 fluorouracil released and percentage change in r2 is shown here……142

LIST OF TABLES

Table1.1 Comparing various imaging modalities ……..…22
Table 2.1 Comparing techniques for the synthesis of iron oxide ……..…41
Table 2.2 Choice of TR and TE for conventional spin echo….....64
Table 2.3 Choice if TR, TE and flip angle for gradient echo sequences……..65
Table 5.1 shows the hydrodynamic size of the porous silicon nanoparticles at different stages in the preparation of the nano-composite……....135
Table 6.1 uses the imaging feasibility criteria described in Chapter 6 to determine the imaging feasibility under different situations involving target concentration, renal and biliary clerance and plasma protein binding……..…….149

ACKNOWLEDGEMENTS

My thesis would have been impossible without all the great help I had along the way. When I started my thesis project in April 2009, Luo Gu showed me how to etch porous silicon. Matt Kinsella and Jennifer Andrew taught me how to make magnetic nanoparticles.

I worked with Dr Rebecca Thielmann and I certainly thank her for giving me support to work on the 1.5 Tesla MRI. She always motivated me and dispensed valuable advice when I needed it.

I thank Dr Olivier Girard for working with me from April 2011 to August 2011 to obtain measurements for my thesis on the 3Tesla magnet. Olivier was a great friend and also a mentor. I would like to thank Dr Mark Bydder for going through the difficult MRI physics with me and working with me on T1, T2 and T2* measurements/maps. I thank Ms Sabine Faulhaber for the STEM images. I thank Dr Anthony Mrse for the NMR time, the training and explaining with enthusiasm whenever I had questions.

I would especially like to thank Dr Mike Sailor for taking me into his lab to start my thesis project. I thank Dr Mike Sailor and Dr Robert Mattrey for being advisors on my thesis.

Last, but not the least, I thank Dr Esener, Dr Zhang and Dr Gianneschi for being on my committee and providing valuable advice.

VITA

November 2004 Bachelor of Science, University of Sydney

June 2005 Masters of Applied Science, University of Sydney

December 2012 Doctor of Philosophy, Materials Science and Engineering, University of California, San Diego

ABSTRACT OF THE DISSERTATION

T_2 Tunable Porous Silicon Iron oxide nanocomposites for Magnetic Resonance Imaging guided drug delivey

by

Shalini Ananda Yogendran

Doctor of Philosophy in Materials Science and Engineering

University of California, San Diego, 2012

Professor Robert F Mattrey, Chair

Professor Michael J Sailor, Co-Chair

Two materials in particular: porous silicon nanoparticles and iron oxide nanoparticles have already produced technologies geared towards the treatment of disease. The objective of this thesis is to harness the combined properties of porous silicon and iron oxide nanoparticles and investigate the suitability of this nanocomposite as T2 tunable materials for magnetic resonance imaging guided drug delivery.

In the first two chapters, the tools and methodologies necessary for the development and study of porous silicon iron oxide nanocomposite based IGDD (image guided drug delivery) agents are identified and described.

The optimization of transverse relaxation rate is crucial to building agents for magnetic resonance imaging. In this regard, in Chapter 3 the effects of the structural properties of iron oxide aggregates on transverse relaxation were studied. The transverse relaxation of several shapes of iron oxide nanoparticle clusters were analysed through monte carlo simulations. A shape described by a combination of circular and linear clusters was found to produce optimal transverse relaxation. Then, in Chapter 4 we investigate another mechanism to increase transverse relaxation. Here, the effect of tuning self diffusion coefficient of protons on transverse relaxation is studied by confining iron oxide aggregates into porous silicon matrices of two different pore sizes. Iron oxide nanoparticles loaded into 15nm porous silicon increased R2 to a greater extent than iron oxide nanoparticles loaded into a 25nm porous silicon matrix.

In Chapter 5, the utility of the above mentioned porous silicon iron oxide nanocomposites as image guided drug delivery agents is studied. Nanoparticle formulations with an imaging and a therapeutic agent could allow non invasive assessment of low molecular weight drugs releasing from nanoparticles. In this regard, release of a hydrophobic drug and a hydrophilic drug from biodegradable porous silicon iron oxide nanocomposites were studied *invitro*. Quantification of drug release, self-diffusion coefficient of protons during degradation of the matrix

and transverse relaxation times during 0-8 hours revealed the change in self-diffusion coefficient during degradation of the matrix as the mechanism for tuning transverse relaxation of porous silicon iron oxide nanocomposites. A linear relationship was observed for hydrophobic drugs between the percentage change in transverse relaxation and percentage drug released and a non linear relationship for hydrophilic drugs. Therefore, porous silicon iron oxide nanocomposites can be used to determine concentration of drug released from transverse relaxation measurements for hydrophobic drugs.

1 INTRODUCTION

Chapter 1 INTRODUCTION

1.1 Scope

1.2 Image guided drug delivery: Toward personalized medicine

1.3 Nanosystems for image guided drug delivery

1.4 Porous silicon based theranostic nanoparticles

1.5 Iron oxide based theranostic nanoparticles

1.6 Magnetic resonance imaging

1.7 Research objectives

1.1 Scope

Nanoparticles have impacted medicine in the last decade with differentiating and novel properties compared to their bulk counterparts [1]. Two materials in particular: porous silicon nanoparticles and iron oxide nanoparticles have already produced technologies geared toward the treatment of disease. Porous silicon nanoparticles have tremendous potential to impact medicine with unique electromagnetic and structural properties such as quantum confinement and high surface area for drug loading. [2] Properties of iron oxide nanoparticles including superparamagnetism and Neel relaxation have resulted in the use of these nanoparticles for magnetic resonance imaging and interventional oncology. The field of image guided drug delivery has recently advanced to use nanoparticles with a therapeutic and imaging ability or ‘theranostic nanoparticles’ to monitor

treatment efficacy with minimal systemic involvement. [3] The objective of this thesis is to build a nanosystem for image guided drug delivery by harnessing the combined properties of porous silicon and iron oxide nanoparticles.

1.2 IMAGE GUIDED DRUG DELIVERY: TOWARD PERSONALIZED MEDICINE

Cancer therapy is limited by the inability of chemotherapeutics to bypass biological barriers, the seemingly non-specific delivery and poor biodistribution of drugs, observed ineffectiveness against metastatic disease, drug resistance of cancers, and relative lack of an effective modality for treatment monitoring. [1, 4]

By definition, personalized medicine is a medical model where practices and decisions on a person's therapy are individualized based on genetic and information related to a person's response to therapy. [5] Personalized medicine in cancer would provide the ability to monitor treatment in real-time to allow physicians to adjust the type and dosing of drug for each patient to prevent overtreatment that would result in harmful side-effects, or undertreatment that would lead to incomplete cancer remission. Furthermore, the ability to see when a drug reaches a maximum tolerable concentration in off-target organs and a sufficient concentration in the tumor would provide a cost-effective advantage over separate treatment and monitoring systems for an individual undergoing cancer treatment.[6]

Presently, nanoparticles can be used for imaging or therapeutic delivery. With respect to medical imaging, many different types of nanomaterials have been

developed to provide contrast. [7] Some of these materials incorporate an imaging moiety into their design, while others provide contrast as a result of their intrinsic material properties. Multiple imaging modalities can also be implemented into a single nanotheranostic design by incorporating multiple moieties to provide a more complete picture of the disease. [8] Molecular imaging can identify tumor cell location within the body, and aims to provide information such as metabolism, expression profile, and stage of the disease. Furthermore, molecular imaging can reveal early tumor response to therapy that will aid in improving treatment regimens.[9]

NP-based therapy can provide a significant advantage over standard chemotherapies by increasing the drug delivery specifically to the tumor site through either passive or active means. [10] Passively targeted nanoparticles may passively accumulate in the tumor site due to the EPR effect, with PEGylation enhancing this effect. The attachment of a targeting ligand (active targeting) can promote cellular uptake and distribution of the NP throughout the tumor, and proper engineering of the NP can ensure the desired intracellular trafficking. [11] The NP design can also utilize light, pH, ultrasound, and magnetic fields for targeting and distribution throughout the tumor. [8]

Theranostic nanomedicines, mostly nanoparticles (NPs) carrying therapeutics, are designed to improve current cancer therapies by addressing the specific existing limitations. Recently, in this regard a variety of nanotheranostic technologies have been developed and studied for assessing target site

accumulation of drugs, facilitate triggered drug release, assess drug distribution at target site and visualize drug release.

In the context of personalized medicine, these technologies aim to provide real-time feedback on the efficacy of targeted therapeutic interventions; theranostic nanoparticles can also be used to facilitate clinical efficacy analysis, to prescreen patients, and to realize the potential of personalized medicine. [12] The clinically most relevant applications of theranostic nanomedicines relate to their use for validating and optimizing the properties of drug delivery systems, and to their ability to be used for pre-screening patients. Furthermore, the combination of diagnostic and therapeutic agents within a single formulation provides real-time feedback on the pharmacokinetics, the target site localization and the (off-target) healthy organ accumulation of nanomedicines. [13]

Ultimately, it can be reasoned that only in patients which show high levels of target site accumulation, and which respond well to the first couple of treatment cycles, targeted therapy should be continued, and that in those in which this is not the case, other therapeutic options should be considered. [13] Hence, treatment is personalized for each patient.

1.3 NANOSYSTEMS FOR IMAGE GUIDED DRUG DELIVERY

This section will provide examples of nanosystems used to assess target site accumulation, assessing drug distribution, visualize drug release and facilitating triggered drug release.

1.3.1 Target site accumulation of drugs

Presently, there are nanosystems that assess accumulation of drugs at the target site. In an animal model of rheumatoid arthritis, comparable observations were made using technetium-99m-labeled PEGylated liposomes. Like tumors, also severely inflamed arthritic joints are characterized by an enhanced vascular leakiness, enabling long-circulating nanomedicines to extravasate into these lesions by means of EPR. [14] Similar findings have recently been reported by Wang and colleagues, who instead of PEGylated liposomes used HPMA copolymers as long-circulating and passively disease site-targeted nanocarriers. To provide proof-of-principle for target site accumulation, they developed a theranostic nanomedicine formulation containing gadolinium, and they demonstrated by means of magnetic resonance imaging (MRI) that Gd-DO3A-modified poly(HPMA) effectively accumulates in the ankles of rats suffering from adjuvant-induced arthritis, whereas no accumulation was observed in the ankles of healthy rats. [15] In line with this, and in line with the above results on the efficacy of liposomal prednisolone phosphate, follow-up experiments showed that conjugating the corticosteroid drug dexamethasone to a long-circulating HPMA copolymer yielded a substantial improvement in disease inhibition, [16] indicating that also this passively targeted anti-inflammatory nanomedicine formulation might hold significant clinical potential.

1.3.2 Assessing drug distribution at target site

Assessing drug distribution at the target site has been undertaken using gadolinium-labeled liposomes. Mulder, Nicolay and colleagues, for instance, have recently shown in this regard that RGD-modified endothelial cell-targeted liposomes and RAD-modified control liposomes distribute quite differently within tumors [17]. It was found that liposomes targeted to endothelial cells accumulated much more strongly in the angiogenic rim of subcutaneously transplanted B16 tumors, whereas control liposomes distributed much more evenly within these tumors. This finding was confirmed using immunohistochemistry.

1.3.3 Visualizing drug release

An approach to this challenge involved the use of manganese sulfate ($MnSO_4$) both to load doxorubicin into liposomes (by means of a method comparable to that used in ammonium sulfate/pH gradient loading) and to generate a significant increase in MR signal upon drug and contrast agent release. [18] Standard (nonthermosensitive; NTSL) and temperature-sensitive liposomes (TSL) were used in these studies, which included both in vitro and in vivo experiments, and it was shown that the relaxivity—i.e. the potential for MR signal enhancement—of TSL at temperatures below the transition temperature (T_g) was comparable to that of NTSL, but that it substantially increased upon heating to temperatures exceeding the T_g (i.e., > 39.5 °C), indicating release of Mn^{2+} from the liposomes. [19] These findings were confirmed in two follow-up analyses, in which contrast

agent release from TSL was correlated with doxorubicin release, and in which drug dose painting was performed on the basis of MRI. [18] TSL rapidly released their contents upon iv administration to rats bearing preheated fibrosarcoma tumors, and they primarily did so in the well-vascularized and well-perfused periphery of the tumors Contrast agent release was determined noninvasively by means of MRI, correlated well with doxorubicin release, which was analyzed invasively using HPLC and fluorescence. When the $MnSO_4$ and doxorubicin coloaded TSL were—as in the above example—injected into rats during steady-state hyperthermia, i.e. at a time point when the tumors were already homogeneously heated, then release was mainly observed in the periphery. In this case, the vast majority of drug and contrast agent was apparently already released before the TSL could penetrate into the central regions of the tumor. Rats injected with TSL before the initiation of hyperthermia, on the other hand, displayed a release and signal enhancement pattern that followed the initial wave of heat as it emanated from the hyperthermia-generating catheter in the middle of the tumor resulting in a central enhancement. In this case, injection of the liposomes before hyperthermia apparently enabled the TSL to perfuse throughout the tumor toward the central heating source before releasing their contents. Finally, rats were treated with two equal doses of TSL and with a combination of the two above-mentioned heating regimens, and as expected, the first fraction of liposomes released their contents at the center of the tumor, and the second at the periphery, together leading to a very uniform enhancement pattern. These examples convincingly demonstrate the suitability of this MRI-

based methodology to visualize and quantify drug release with high temporal and spatial resolution [20] . Alternative methods to achieve this goal, based for instance on optical (i.e., near-infrared) imaging agents and quenching−dequenching effects, might also enable a real-time visualization of drug release, but no such efforts have been undertaken thus far, and their in vivo applicability is expected to be limited, due to the limited penetration depth of optical imaging probes and/or to problems associated with quantification. [21]

1.3.4 Facilitating Triggered drug release

An elegant example of such a theranostic nanomedicine formulation that can be used for facilitating triggered drug release has recently been developed by Langereis, Gruell and colleagues, who have prepared thermosensitive liposomes containing two different MR contrast agents. [22] This system contains both a CEST agent (i.e., chemical exchange saturation transfer; [Tm(HPDO3A)(H_2O)]) and a ^{19}F probe (i.e., NH_4PF_6), both of which are coloaded into the aqueous interior of the liposomes. At temperatures below the T_g, when the liposomal bilayer is intact and when there is no free access to surrounding water molecules, the CEST agent generates a signal that can be used to track the biodistribution and the target site accumulation of the formulation, and it at the same time quenches the ^{19}F signal. Upon heating to temperatures exceeding the T_g, and upon release of both the CEST agent and the ^{19}F probe from the aqueous interior of the liposome, the CEST signal disappears, and the ^{19}F signal appears.

A single system that could target site accumulation of drugs, assess drug distribution at target site, visualize drug release and triggering drug release could prove cost effective and take us closer to personalized medicine. Nanoparticles such as iron oxide nanoparticles, gold nanoparticles, quantum dots and carbon nanotubes have been previously investigated for imaging and drug delivery [23]. These NPs can enable treatment monitoring by either attaching different imaging/ drug moieties or taking advantage of the intrinsic properties of some NP materials [11]. The next two sections focuses on nanoparticles relevant to this thesis: porous silicon nanoparticles and iron oxide nanoparticles and proceeds to highlight some of the theranostic technologies developed.

1.4 POROUS SILICON BASED THERANOSTIC NANOPARTICLES

This section provides a brief overview of porous silicon theranostic nanoparticles. An in-depth discussion of synthesis and characterization can be found in Chapter 2 of this thesis.

Porous silicon nanoparticles exhibit porosity or ‘molecular sieve’ structure that can be controlled via chemical methods. Such mesoporous nanostructures consist of empty channels and provide a large surface area that may act as excellent reservoirs for small molecules or imaging agents. With the molecular-sieve structure, porous silicon nanoparticles can load a variety of small molecule pharmaceuticals via covalent attachment, spontaneous adsorption and trapping by oxidation [24] .

Porous silicon nanoparticles are made using physical methods. A typical preparation consisted of HF etching of single-crystal silicon wafers, lifting-off of the porous silicon film, ultrasonication, filtration of the formed particles through a 0.22-μm filtration membrane and finally activation of luminescence in an aqueous solution. The luminescence was generated by quantum confinement effects and the defects localized at the $Si–SiO_2$ interface. Such luminescent porous nanoparticles were loaded with DOX and their drug release and cytotoxicity were studied in vitro. One unique feature of such nanoparticles is that they can degrade in vivo and be renally cleared within a relatively short period of time[2].

1.5 IRON OXIDE BASED THERANOSTIC NANOPARTICLES

1.5.1 Magnetic nanoparticles

Magnetite (Fe3 O4) belongs to the iron oxide family. Magnetite has the particularity of containing both Fe2+ and Fe3+ ions, within an inverse spinel structure. Thirty-two oxygen anions form a face-centered cubic unit cell, with an edge length a = =0.839 nm. In this unit cell, iron ions are located on 8 tetrahedral sites (surrounded by four oxygen ions) and 16 octahedral sites (surrounded by 8 oxygen ions). The tetrahedral sites are exclusively occupied by Fe3+ ions, while Fe2+ and Fe3+ ions alternately occupy octahedral sites (Figure 1a). This organization is sometimes expressed in another formula for magnetite Fe3+ [Fe2+ Fe3+]O and maghemite Fe3+ [Fe3+V13]O4 where V represents a cation vacancy.

Magnetite is ferrimagnetic; because of superex-change oxygen-mediated coupling, all the magnetic moments of the tetrahedral iron ions are aligned in a specific direction, while all the octahedral iron mag-netic moments are aligned in the opposite direction. Since there is the same number of octahedral and tetra-hedral Fe3+ ions, they compensate for each other, and the resulting moment of a magnetite crystal arises only from the uncompensated octahedral Fe2+ ions (Fig-ure 1b). The magnetic properties of maghemite are due to the uncompensated octahedral Fe3+ ions.

The resulting magnetic moment of a magnetite (or maghemite) crystal is not directed arbitrarily; it is preferentially aligned along specific directions, called anisotropy axes. These axes are principally determined by the magneto-crystalline anisotropy field, which depends on the composition and crystallographic structure of the magnetic compound. The coupling energy between this field and the crystal magnetic moment is minimal when the magnetic moment is directed along some particular directions.

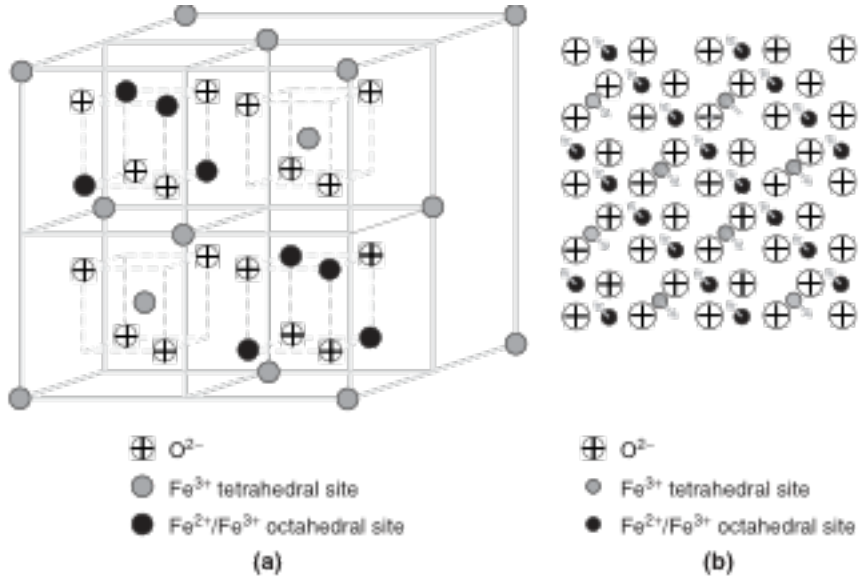

Figure 1.1: Inverse spinel structure of magnetite (a) The front side of the cube is shown(b) Ferrimagnetic organization in magnetite. (Adapted from reference [25])

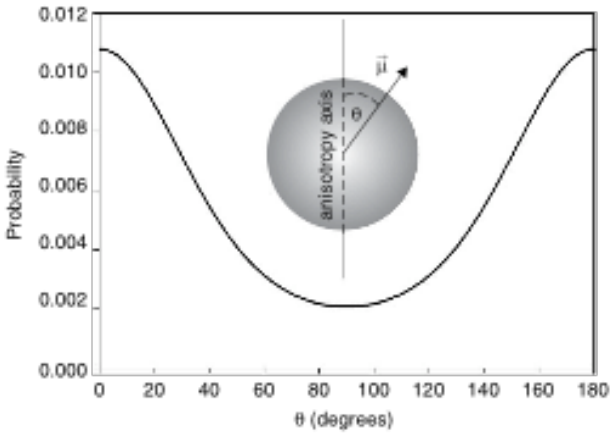

Figure 1.2: Model of uniaxial anisotropy for a magnetite (or maghemite) nanoparticle. The graph shows the probability of alignment of the magnetic

moment in one direction with respect to the angle between this direction and the anisotropy axis(for sphere with a radius R =5nm and an anisotropy constant =K =13,500Jm− 3) For these single domain crystals, a flip of the magnetic moment from one direction of anisotropy to another can be observed. If the thermal energy, given by kBT, is sufficient to overcome the anisotropy energy barrier, the magnetization will fluctuate between the different anisotropy directions, with a characteristic time called the Neel relaxation time. (Adapted from reference [25])

1.5.2 Neel relaxation time.

Neel relaxation refers to the relaxation of the global electronic moment of a superparamagnetic crystal constituted by a ferri, ferro, or antiferromagnetic compound. It does not concern the nuclear relaxation of water protons. However, the relaxation of the particle's huge magnetic moment will, of course, influence water proton relaxation rates. For a superparamagnetic particle of volume V, with a constant of anisotropy K, the N´eel relaxation time is given by :

$$\tau = \tau_0 e^{(KV)/(k_b T)}$$ (Equation 1)

where τ_0 is the pre-exponential factor and kb the Boltzmann constant. The Neel relaxation time thus increases as an exponential function of the volume of the particle. Therefore, the flipping of the magnetic moment of a magnetite crystal is observed only for nanoparticles. For magnetite $\tau_0 \approx 10^{-9} s$ and $K \approx 13500 Jm^{-3}$. So, when the particle radius is about 15 nm, τ is approximately equal to 700 years, which explains why magnetite has been used for magnetic data recording. Even

when the radius is larger than 10 nm, τ becomes greater than 1 ms. Because the diffusive rotation time of the particles in the colloid and the diffusion time of water molecules around the particles are far shorter than 1 ms, it seems clear that Neel relaxation has no effect on the nuclear relaxation induced by large magnetic particles.

Stable aqueous suspensions of magnetite (or maghemite) nanoparticles are said to be superparamagnetic because they show no remanence: when they are submitted to a magnetic field, their global magnetic moment aligns in the direction of the field, but when the field is set to zero, the sample magnetic moment also returns to zero. This behavior is the same as paramagnetism, but with a huge particle magnetic moment (compared to that of a paramagmetic ion, for example): this phenomenon is therefore called superparamagnetism. This nonremanence is due to the return to equilibrium of the magnetic moments (compared to that of a paramagnetic ion, for example): this phenomenon is therefore called superparamagnetism. This nonremanence is due to the return to equilibrium of the magnetic moments through Neel relaxation, when the particle is small enough, or through the diffusive rotation of the particle in the solvent in the case of larger particles. Macroscopically, the magnetization of a magnetite (or

maghemite) nanoparticle suspension is described by a Langevin function, whose shape depends on the saturation magnetization (Msat) and the size of the magnetite crystals.

$$M(B) = M_{sat} L(x) = M_{sat}\left(\coth(x) - \frac{1}{x}\right)$$ (Equation 2)

with $x = \frac{\mu_{sat} B}{kT}$

1.5.2 Superparamagnetic Iron oxide nanoparticles in theranostics

IONPs with appropriate coatings can be easily coupled with drug molecules. For instance, the Zhang group coupled methotrexate (MTX), an anti-cancer drug, onto an aminated IONP surface. In vitro studies demonstrated that the particles, after internalizing into cells, accumulated in lysosomes, where the drug molecules were released due to the low pH and the presence of proteases. [26] Hwu et al. reported on coupling paclitaxel (PTX) to IONP surfaces through a phosphodiester moiety at the (C-2′)-OH position. The average number of PTX molecules per nanoparticles was evaluated to be 83, and the release of the PTX was found to be more effective when exposed to phosphodiesterase. [27] The Cheon group used meso-2,3-dimercaptosuccinic acid (DMSA) to modify IONPs, and used SMCC as the crosslinker to couple Herceptin antibody molecules onto the particle surface, although Herceptin was harnessed as a targeting agent rather than a therapeutic agent in the study [28].

Aside from covalent coupling, drug molecules can also be co-capsulated with IONPs into polymeric matrices. Jain et al. loaded doxorubicin (DOX) and PTX, along with oleic acid coated IONPs, into pluronic-stabilized nanoparticles. [29] Similarly, Yu et al. [30] loaded DOX into anti-biofouling polymer coated IONPs.

When applied in a Lewis lung carcinoma xenograft model, such DOX loaded nanoconjugates showed better pharmacokinetics and therapeutic effects than DOX alone. It is known that small molecules can be loaded into porous nanostructures via physical absorption. In parallel, there have been efforts to achieve hollow iron oxide nanostructures. One such effort was reported by the Hyeon group.[31] Starting from spindle-shaped β-FeOOH NPs made from $FeCl_3$ hydrolysis, they performed a three step, so-called “wrap-bake-peel” treatment to achieve hollow IONPs. In a proof-of-concept study, they found that DOX could be loaded into such hollow nanoparticles via simple physical absorption and then released from the nanostructures in a sustained manner under physiologic conditions.

Another example by the Sun group: By controlled oxidation and acid etching of Fe particles, they were able to achieve porous IONPs with a sizable cavity. They then loaded cisplatin into the cavities of the particles, and coupled Herceptin onto the particle surfaces to confer targeting specificity. The resulting conjugates showed selective affinity to ErbB2/Neu-positive breast cancer cells and a sustained cytoxicity attributable to the controlled release of cisplatin from the particle carriers [32].

IONP can itself play an imaging/therapy dual role, due to its potential in hyperthermia. The underlying mechanism is that IONPs can act as antennae in an external alternating magnetic field (AMF) to convert electromagnetic energy into heat. [33] This feature holds promise in tumor therapy for tumor cells that are

more susceptible to elevated temperature than normal cells. In one example, phospholipid coated IONPs were injected into a subcutaneous tumor model in F344 rats, and were exposed to an AMF. The AMF in conjugation with IONPs raised the temperature of tumor above 43 °C and caused tumor regression, but had no effect on the control group where no IONPs were given. Also, Fab fragment of anti-human MN antigen-specific antibody was chemically anchored onto IONP surfaces and the INOPs were administrated systemically into tumor-bearing mice. The particles showed high tumor uptake, presumably due to an antibody-antigen interaction, and induced efficient tumor hyperthermia when exposed to an AMF. [33]

In another study, Zn-Pc, a photodynamic therapeutic (PDT) agent, was loaded onto $CoFe_2O_4$ nanoparticles, which showed better hyperthermia effects than IONPs. When evaluated in vitro with J774-A1 macrophage cells, a combined toxicity from both PDT and magnetohyperthermia was observed; however, more work needs to be done to elucidate the synergy of such combinational in vivo therapy. [34]

Concerns regarding toxicity still remain in iron oxide-based nanomedicine, such as magnetic resonance imaging (MRI) and magnetic force drive drug/gene delivery. Recent studies have shown the possibilities of iron oxide nanoparticles affecting normal cell functionalities, instead of simply being carriers [35]. It has been widely accepted that uncoated iron oxide nanoparticles elicit massive cellular internalization associated with significant cell death, however, iron oxide

nanoparticles coated with hydrophilic and biocompatible substances have shown less cytotoxicity in a range of cell lines [36]. Gupta demonstrated a dose-dependent reduction in cell adhesion and viability of bare iron oxide nanoparticles, while pullulan, lactoferrin, and ceruloplasmin coated nanoparticles showed no significant cell detachment or morphology changes on human fibroblasts [37].

A proposed mechanism of nanoparticle-mediated cytotoxicity is that it is attributed to the generation of reactive oxidative species (ROS) and cellular internalization [35]. Transition metal or transition metal oxide nanoparticles can generate ROS as catalysts in a Fenton-type reaction, in which hydrogen peroxide is reduced by ferrous ions to form extremely active hydroxyl-free radicals and lead to biological damage within the diffusion range.

$$^{\bullet}O_2^- + H_2O_2 \xrightarrow{Fe(II)/Fe(III)} {}^{\bullet}OH + OH^- + O_2$$ (Equation 3)

Studies of the intracellular destination of iron oxide nanoparticles are particularly important in determining the cytotoxicity of such nanomaterials and designing effective nanomaterials for biomedical applications. Most of the work has focused on receptor mediated internalization and the endocytic pathway of such nanostructures, including the effect of the physico-chemical properties of nanoparticles, i.e. size, shape, chemical composition, surface-to-volume ratio, and surface charges, on the cellular response of different cells [38]. It has been established that receptor-mediated internalization strongly depends on the size of the particles. Both clathrin- and caveolae-mediated endocytosis has been

reported, however, controversial results on the effect of particle size and surface coating on the endocytosis pathway has also been reported [36].

The magnetic properties of iron-oxide makes it suitable for magnetic resonance imaging.

1.6 MAGNETIC RESONANCE IMAGING OF IRON OXIDE

1.6.1 History of NMR

In 1939 Rabi and his co-workers conducted the following experiment: A beam of hydrogen molecules were sent, first through an inhomogeneous magnetic field, and then through a homogeneous one in which radio frequency electromagnetic energy was applied to the molecules. At a sharply-defined frequency, this energy was absorbed by the molecular beam. Consequently the beam underwent a small deflection. This was the first observation of nuclear magnetic resonance (NMR), but it was performed under very high vacuum. It was not until 1946, that Purcell, Torrey and Poundat Harvard University, and Bloch, Hansen and Packard at Stanford University, simultaneously demonstrated the phenomenon of NMR in bulk materials, such as paraffin wax and water, in the liquid state. [39] Both groups received the Nobel Prize in 1952 for this discovery. Shortly after this, Purcell and Bloch discovered the phenomenon of NMR in solids and liquids; it was found that the precise resonance frequency of a nucleus depends upon the state of its chemical environment. In1951, separate resonance lines were observed for chemically different protons in the same molecule.

Since then, NMR has become increasingly important in all chemical analysis. For example, the combination of proton (1H) and carbon-13 (13C) NMR spectroscopy provides a valuable tool widely exploited by organic chemists for solving structural problems of organic molecules. The NMR technique has also been applied to the studies of complex molecules with biological significance, providing, for example, structural information on proteins and nucleic acids. In 1971, the potential of NMR to discriminate between different tissues was recognized by Damadian. In 1973, Lauterbur successfully produced the first MR image from a conventional NMR spectrometer with addition of linear magnetic field gradients to incorporate the spatial information of protons for magnetic resonance imaging (MRI; Lauterbur 1973). The potential of such a technique for diagnostic medicine was immediately realized. During the past two decades, facilitated by further improvements in instrumentation (superconducting magnets and faster computers) and imaging techniques (back-projection or two-dimensional Fourier image reconstruction (Housefield and Ambrose 1973), MR imaging and spectroscopy techniques have become available for non-invasive clinical studies of human anatomy and metabolism. MR imaging techniques have the advantage over other imaging techniques, such as Computed Tomography (CT), provide high soft tissue contrast while not employing ionizing radiation [40]. For these reasons, MRI has become a routine clinical tool for the diagnosis of many pathological conditions and for evaluating metabolic functions.

Table1.1: Comparing various imaging modalities

Modality	Spatial Resolution mm (clinical)	Sensitivity (mole/L)	Target	Depth	Cost	Probe	Primary Small Animal Use	Clinical Use
MRI	0.025 - 0.1 (0.2)	10^{-3} to 10^{-5}	A,P,M	No limit	$$$	Gadolinium, iron oxide particles	Versatile; high soft-tissue contrast	Yes
CT	0.05 - 0.2 (0.5 - 1)	not well characterized; 10^{-3} to 10^{-5}	A,P	No limit	$$	Iodine	lung & bone imaging	Yes
Ultrasound	0.05 - 0.5 (0.1 - 1)	not well characterized	A,P	mm - cm	$$	microbubbles	vascular and interventional imaging	Yes
PET	1 - 2 (6 - 10)	10^{-11} to 10^{-12}	P, M	No limit	$$$	^{18}F, ^{11}C, ^{15}O	Versatile; many different tracers	Yes
SPECT	1 - 2 (7 - 15)	10^{-10} to 10^{-11}	P, M	No limit	$$	^{99m}Tc, ^{111}In chelates	commonly used to image labelled antibodies, peptides and so on	Yes
Optical: Fluorescence Imaging	2 - 3	not well characterized, ~ 10^{-9} - 10^{-12}	P, M	< 1 cm	$ - $$	Photoproteins, NIR fluorochromes	rapid screening of molecular events in surface-based tumors	Development
Optical: Bioluminescence Imaging	3 - 5	not well characterized, ~ 10^{-13} - 10^{-17}	M	1 - 2 cm	$$	Luciferins	Gene expression, cell and bacterial tracking	No

Nomenclature:

$ < 100,000, $$ 100 –300,000, $$$ > 300,000;

A = anatomic; P = physiologic, M = molecular

1.6.2. Magnetic Resonance Imaging (MRI)

MRI makes uses of a unique physical property of nuclei with odd mass number which have the property of spin . The spin angular momentum can be expressed as follows [39]:

$$\mu_N = \gamma_N \frac{h}{2\pi} I \quad \text{(Equation 4)}$$

Where: μ_N is the magnetic moment of the nucleus, N is the magnetogyric ratio of the nucleus, which is a unique constant for each type of nucleus

($\text{radians} \bullet \text{sec}^{-1} \bullet \text{Gauss}^{-1}$), h is Plank's constant, and I is the nuclear spin quantum number of the nucleus.

For example, protons (^{1}H) have a nuclear spin quantum number =1/2, $=2.67\text{x } 10^4 \textit{radians} \bullet \text{sec}^{-1} \bullet \text{Gauss}^{-1}$ (or $42.58 \text{ MHz} \bullet \text{Tesla}^{-1}$). Only the nuclei with spin can be detected by NMR techniques.

In the following discussion, the proton (1H) will be used as an example because it is the most abundant nucleus in the body, used in MRI and therefore most relevant to this thesis. In the absence of a magnetic field, the magnetic moments of protons in the body are oriented randomly. However, in the presence of a constant magnetic field, (Bo with direction z), the nuclear spin states allowed (E_m) are quantized (equation 2), and the quantum number m_I can only take up a set of discrete values from +I, (I- 1), ...-I [41].

$$E_m = -\gamma \frac{h}{2\pi} m_I B_0 \quad \text{(Equation 5)}$$

In the case of protons, with I = 1/2, ml can only take values of + 1/2 and - 1/2. Therefore, only two nuclear spin directions, for two energy levels that the protons occupy, are allowed. The lower energy level (m = +1/2) corresponds to the situation that the nuclear moment aligns parallel to the steady field, and the higher energy level

(m = -1/2) represents the anti-parallel situation. . At equilibrium, the protons are distributed over the two possible energy states according to The Boltzmann distribution law [41]:

$$\frac{N_{-1/2}}{N_{+1/2}} = e^{-\Delta E / kT} \quad \text{(Equation 6)}$$

Where ΔE is the energy difference between the two levels, k is Boltzmann's constant, and T is the temperature in Kelvin. When an electromagnetic field perpendicular to the constant field Bo is applied to a system with a frequency v satisfying equation 4, absorption of energy occurs in the spin system and transitions take place between the two nuclear spin levels [42].

$$\Delta E = v \bullet h = \gamma \frac{h}{2\pi} B_0 \quad \text{(Equation 7)}$$

The frequency is defined as resonance frequency of the nucleus. For examples, at 1.5T, the resonant frequent would be 64MHz and so on.

1.6.3 RF Pulses

The energy causing the transition of protons between the nuclear spin states can be applied in a package of radio frequency oscillations, called a radio frequency (RF) pulse. Macroscopically, the vector sum of the magnetic dipole moments of the nuclear spin system at equilibrium in the presence of Bo can be represented as M. Various types of RF pulses have been used in MR imaging, and the following are most common ones: An "excitation pulse" changes the equilibrium

magnetization (M) into the transverse plane (XY). It is therefore often called a 90° pulse. A pulse which converts M into -M is a 180° pulse, also called an inversion pulse. This pulse is employed at the beginning of an inversion recovery sequence, which is commonly used to measure relaxation times. Another type of 180° pulse is employed to convert the precessing magnetization vectors of the XY plane to their mirror-image position with respect to the pulse axis. If this pulse is applied at time after a 90° pulse, the magnetization vectors of the spins precessing at different frequencies will start to precess in the opposite direction. Thus, at time 2x, the magnetization vectors of the spins will refocus along the original magnetization vector, generating an echo. This pulse is often referred to as a refocusing pulse, commonly used in spin-echo experiments [43] .

1.6.5 Spin-Spin Relaxation (T2)

When this RF pulse is applied, the moments in the xy plane begin to lose their precessing phase coherence, due to the natural processes that cause nuclei to exchange energy with each other. As a result of this process, called spin-spin relaxation, the net Mxy magnetization decays to zero exponentially with time (equation 6), characterized by the time constant T2 which is often measured by a CPMG sequence [44] .

$$M_{XY}(t) = M_{XY}(0) \bullet e^{-t/T_2}$$ (Equation 9)

1.6.6 Image Contrast

The tissue contrast to noise ratio (CNR, equation 7) appearing on an MR image forms the basis for medical diagnosis. The CNR can be altered by the choice of specific pulse

sequences and the associated timing parameters [43].

$$CNR = \frac{SI_1 - SI_2}{Noise} \quad \text{(Equation 10)}$$

SI_1 and SI_2 represent the signal intensities of two adjacent regions on an MR image. The magnitude of the detected signal depends upon the spin density (number of protons available), T2 characteristics of tissues, chemical shift, temperature, and flow phenomena. Among these parameters, the relaxation characteristics are most influential to the signal intensity. Therefore the tissue contrast of an MR image can be T2weighted. In the spin-echo imaging sequence (the most common pulse sequence), for example, the type of image weighting can be manipulated by the repetition time (TR) and the echo time (TE). A 90°excitation pulse is followed by a 180° refocusing pulse, generating an echo at TE. The signal intensity of the image can be approximated by equation 8 [44]:

$$SI = M_Z(0)[1 - e^{(-\frac{TR}{T_1})}] \bullet e^{(-\frac{TE}{T_2})} \quad \text{(Equation 11)}$$

where SI is signal intensity on an MR image, TR is the repetition time, and TE is the echo time in a pulse sequence. The initial 90^0 excitation pulse completely tips the longitudinal magnetization into the transverse plane, and a time interval (TR)

is allowed to elapse between excitations, during which time the spins undergo relaxation. Similarly, TE determines the extent of T2 relaxation. The longer the time interval TE, the greater the extent of T2 relaxation. The short TE value diminishes the importance of tissue T2 differences. On the other hand, images acquired with long TR and long TE (TE ~ T2) are T2-weighted. Therefore, tissues with long T2, such as tumors, edema, and cysts, appear bright, whereas tissues that have short T2, such as muscle and liver, appear dark. In summary, the MR image contrast is a function of several parameters including T2 relaxation times, proton density, chemical shift, temperature, magnetic susceptibility, and motion. Image contrast between tissues with different physicochemical properties is determined by the different image signal intensities each tissue produces in response to TR and TE in the case of a spin echo pulse sequence. This in return is determined by Mz (0), directly corresponding to the proton density, T2 relaxation times [43].

The T2 relaxation times are therefore crucial parameters in MR imaging experiments. With conventional MR imaging techniques, however, the relaxation

characteristics of the normal and pathological conditions are often very small. This makes the accurate diagnosis based on the contrast from the MR image difficult. For example, due to the lack of inherent difference between tumor and normal tissues, up to 20% of metastases of the liver can escape detection[45]. Therefore it is important to increase the contrast between the normal tissue and pathological conditions on an MR image to improve the diagnostic accuracy.

Since the variation of relaxation characteristics has a profound effect on the tissue contrast, the selective enhancement of tissue contrast can be achieved by the administration of magneto pharmaceuticals, i.e. Contrast agents, which change the local environment of protons and thereby change their relaxation characteristics.

1.6.6 Imaging with Iron oxide

Based on the magnitude of their R1 and R2, MR contrast agents can be classified T2-dominant [46]. On the other hand, T2 agents largely increase l/T2 of tissue, hence lead to decreases in signal intensity and classified as "negative" contrast agents. Super paramagnetic agents predominantly increase 1/T2.

The efficiency by which MR agents enhance the proton relaxation rate is defined as Relaxivity [47]:

$$R_i = \frac{\Delta M}{\Delta T_i}$$ (Equation 12)

where T_i represents T2, M is concentration of the MR contrast agent, and Ri is T2 relaxivity. Relaxivities provide quantitative measurements of the effects of contrast agents on T2 relaxation times. In a typical relaxivity plot of a conventional contrast agent, inverse relaxation times are plotted against the concentration of contrast agents. The slopes of these curves represent the relaxivity and are expressed in (mM-sec)- or (mmol/L- sec)- 1.

Research on superparamagnetic pharmaceuticals, representing a second class of MR contrast agents, started in 1986. These agents are particles with a much higher magnetic moment due to electron spin coupling in the crystal lattice, and they can significantly enhance the proton T2 relaxation rate ("T2-agents"). Superparamagnetic agents include different types of inorganic iron particles which contain iron in different valency states and vary in their chemical composition, crystal structure, size and coating [47].

Superparamagnetic nanoparticles have a strong effect on the spin-spin (transverse) relaxation process of the nearby protons. The relaxation mechanism of these agents is a complex process, which has been the topic of several papers, and remains an active area of research. Different from paramagnetic chelates, the superparamagnetic nanoparticles have much higher magnetic moment and longer correlation time. The large magnetic moments of such nanoparticles in a magnetic field generate local field inhomogeneities. It is thought that as the protons diffuse through these field inhomogeneities, their larmor frequencies lose coherence of phase, therefore, causing an increase in transverse relaxation rate of protons. The high magnetic susceptibility, i.e. the ability to cause strong inhomogeities in the magnetic field, is desirable for a MR contrast agent because it can significantly reduce the dosage required for sufficient contrast enhancement, thereby reducing it toxicity [44].

Deoxyhemoglobin, an endogenous T2 contrast agent and an exogenous blood-pool contrast agent (mononuclear SPIO or MION) have been studied in dynamic

functional body imaging experiments (fMRI), where contrast and temporal resolution are governed by hemodynamic effects.[48] SPIO agents also produce magnetic susceptibility variations that may be visualized even at fairly low spatial resolution by T2*-weighted imaging.[47]

The relative T2-weighted signal in a single-echo (GRE) sequence is given by [43]:

$$I_n \propto \exp\left[-\int_{t_n}^{t_n+TE} \frac{1}{T2(t)}\,dt\right] \quad \text{(Equation 13)}$$

where T2 is affected by the T2 contrast agent's relaxivity (R2) according to [44]:

$$\frac{1}{T_2(t)} = \frac{1}{T_2(0)} + \left[R_2(0) + \Delta R_2(t)\right]\left[M\right] \quad \text{(Equation 14)}$$

where $T_2(0)$ is the background T2, and $R_2(0)$ and $\Delta R_2(t)$ are the static and time-dependent components of T2 relaxivity, respectively. On the other hand, unless CPMG or phase-locking strategies are used, the image sampling rate is still limited by TR, and very short T2 changes may be missed entirely with probability (1−TE/TR), even if they would be likely to produce a signal change when sampled optimally [44] . A clear advantage of scan series data obtained with T2-weighted imaging sequences, however, is that their time dependence does not depend on the RF flip angle [44] .

1.7 Objectives of the thesis

This thesis employs a physical approach to building nanoparticles for MRI based image guided drug delivery. The ultimate objective of the thesis is to apply the combined properties of porous silicon and iron oxide nanoparticles towards creating materials for image guided drug delivery.

AIM 1: PHYSICAL CONSIDERATIONS FOR OPTIMIZING RELAXIVITY OF POROUS SILICON IRON OXIDE NANOCOMPOSITES

- Characterization of porous silicon nanoparticles, iron oxide nanoparticles, porous silicon iron oxide nanocomposites, drug load porous silicon iron oxide nanocomposites, describing imaging methods to characterize T_2 and T_2* creating computational tools relevant to designing, building and testing an IGDD system. (Chapter 2)
- The effect of structural properties of iron oxide aggregates on transverse relaxivity (Chapter 3)
- Tuning pores size of porous silicon in porous silicon iron oxide nanocomposites to engineer T_2 and T_2* agents for magnetic resonance imaging (Chapter 4)

AIM 2: POROUS SILICON IRON OXIDE NANOCOMPOSITE FOR MONITORING DRUG RELEASE

- Biodegradability of porous silicon results in a signal change function on MRI to enable monitoring of drug released from drug loaded porous silicon iron oxide nanocomposite (Chapter 5)

REFERENCES

1. Anglin, E. J., L. Cheng (2008). "Porous silicon in drug delivery devices and materials." Advanced drug delivery reviews 60(11): 1266-1277.
2. Buzea, C., I. I. Pacheco (2007). Nanomaterials and nanoparticles: sources and toxicity, AVS.
3. Bydder, G., R. Felix (1990). "Contrast Media in MRI." Bussum, The Netherlands, Medicom.
4. Callaghan, P. T. (1993). Principles of nuclear magnetic resonance microscopy, Clarendon Press Oxford.
5. Cheng, K., S. Peng (2009). "Porous hollow Fe3O4 nanoparticles for targeted delivery and controlled release of cisplatin." Journal of the American Chemical Society 131(30): 10637-10644.
6. de Smet, M., E. Heijman (2010). "Magnetic resonance imaging of high intensity focused ultrasound mediated drug delivery from temperature sensitive liposomes; An in vivo proof-of-concept study." Journal of Controlled Release.
7. Delli Castelli, D., W. Dastr (2010). "In vivo MRI multicontrast kinetic analysis of the uptake and intracellular trafficking of paramagnetically labeled liposomes." Journal of Controlled Release 144(3): 271-279.
8. Fisher, M. R., S. D. Wall (1985). "Hepatic vascular anatomy on magnetic resonance imaging." American journal of roentgenology 144(4): 739-746.

9. Ginsburg, G. S. and J. J. McCarthy (2001). "Personalized medicine: revolutionizing drug discovery and patient care." TRENDS in Biotechnology 19(12): 491-496.
10. Gupta, A. K. and M. Gupta (2005). "Cytotoxicity suppression and cellular uptake enhancement of surface modified magnetic nanoparticles." Biomaterials 26(13): 1565-1573.
11. Hamburg, M. A. and F. S. Collins (2010). "The path to personalized medicine." New England Journal of Medicine 363(4): 301-304.
12. Hashemi, R. H., W. G. Bradley (2010). MRI: the basics, Lippincott Williams & Wilkins.
13. Hornak, J. P. (1996). "The basics of MRI." Disponvel em< http://www. cis. rit. edu/htbooks/mri>. Acesso em 8.
14. Hwu, J. R., Y. S. Lin (2008). "Targeted Paclitaxel by conjugation to iron oxide and gold nanoparticles." Journal of the American Chemical Society 131(1): 66-68.
15. Ito, A., M. Shinkai (2005). "Medical application of functionalized magnetic nanoparticles." Journal of bioscience and bioengineering 100(1): 1-11.
16. Jain, T. K., J. Richey (2008). "Magnetic nanoparticles with dual functional properties: drug delivery and magnetic resonance imaging." Biomaterials 29(29): 4012-4021.
17. Janib, S. M., A. S. Moses (2010). "Imaging and drug delivery using theranostic nanoparticles." Advanced drug delivery reviews 62(11): 1052-1063.

18. Jiang, W., B. Y. S. Kim (2008). "Nanoparticle-mediated cellular response is size-dependent." Nature Nanotechnology 3(3): 145-150.
19. Kohler, N., G. E. Fryxell (2004). "A bifunctional poly (ethylene glycol) silane immobilized on metallic oxide-based nanoparticles for conjugation with cell targeting agents." Journal of the American Chemical Society 126(23): 7206-7211.
20. Kumar, C. S. S. R. (2007). Nanomaterials for medical diagnosis and therapy, Vch Verlagsgesellschaft Mbh.
21. Langereis, S., J. Keupp (2009). "A temperature-sensitive liposomal 1H CEST and 19F contrast agent for MR image-guided drug delivery." Journal of the American Chemical Society 131(4): 1380-1381.
22. Lee, J. H., Y. M. Huh (2006). "Artificially engineered magnetic nanoparticles for ultra-sensitive molecular imaging." Nature medicine 13(1): 95-99.
23. Lewinski, N., V. Colvin (2008). "Cytotoxicity of nanoparticles." Small 4(1): 26-49.
24. Mansfield, P. and P. G. Morris (1982). NMR imaging in biomedicine, Academic Press New York.
25. McRobbie, D. W. (2003). MRI from picture to proton, Cambridge Univ Pr.
26. Mulder, W. J. M., G. J. Strijkers (2005). "MR molecular imaging and fluorescence microscopy for identification of activated tumor endothelium using a bimodal lipidic nanoparticle." The FASEB journal 19(14): 2008-2010.

27. Onuki, Y., I. Jacobs (2010). "Noninvasive visualization of in vivo release and intratumoral distribution of surrogate MR contrast agent using the dual MR contrast technique." Biomaterials 31(27): 7132-7138.
28. Palmer, G. M., R. J. Boruta (2010). "Non-invasive monitoring of intra-tumor drug concentration and therapeutic response using optical spectroscopy." Journal of Controlled Release 142(3): 457-464.
29. Park, J. H., L. Gu (2009). "Biodegradable luminescent porous silicon nanoparticles for in vivo applications." Nature materials 8(4): 331-336.
30. Park, J. H., G. Von Maltzahn (2010). "Cooperative nanomaterial system to sensitize, target, and treat tumors." Proceedings of the National Academy of Sciences 107(3): 981.
31. Peer, D., J. M. Karp (2007). "Nanocarriers as an emerging platform for cancer therapy." Nature Nanotechnology 2(12): 751-760.
32. Pekar, J. J. (2006). "A brief introduction to functional MRI." Engineering in Medicine and Biology Magazine, IEEE 25(2): 24-26.
33. Piao, Y., J. Kim (2008). "Wrap bake peel process for nanostructural transformation from FeOOH nanorods to biocompatible iron oxide nanocapsules." Nature materials 7(3): 242-247.
34. Ponce, A. M., B. L. Viglianti (2007). "Magnetic resonance imaging of temperature-sensitive liposome release: drug dose painting and antitumor effects." Journal of the National Cancer Institute 99(1): 53-63.
35. Sawyers, C. (2004). "Targeted cancer therapy." Nature 432(7015): 294-297.

36. Shinkai, M., B. Le (2001). "Targeting hyperthermia for renal cell carcinoma using human MN antigenspecific magnetoliposomes." Cancer Science 92(10): 1138-1146.
37. Steckel, R. J. and A. R. Kagan (1976). Diagnosis and staging of cancer: a radiologic approach, WB Saunders Company.
38. Sun, D. (2010). "Nanotheranostics: integration of imaging and targeted drug delivery." Molecular Pharmaceutics 7(6): 1879.
39. Viglianti, B. L., M. W. Dewhirst (2010). MRI imageable liposomes for the evaluation of treatment efficacy, thermal distribution, and demonstration of dose painting, Google Patents.
40. Viglianti, B. L., A. M. Ponce (2006). "Chemodosimetry of in vivo tumor liposomal drug concentration using MRI." Magnetic resonance in medicine 56(5): 1011-1018.
41. Weissleder, R. (2006). "Molecular imaging in cancer." Science 312(5777): 1168.
42. Westbrook, C., C. K. Roth (2005). MRI in Practice, Wiley-Blackwell.
43. Woodcock, J. (2007). "The prospects for personalized medicine in drug development and drug therapy." Clinical Pharmacology & Therapeutics 81(2): 164-169.
44. Xie, J. and S. Jon (2012). "Magnetic Nanoparticle-Based Theranostics." Theranostics 2(1): 122.
45. Xie, J., S. Lee (2010). "Nanoparticle-based theranostic agents." Advanced drug delivery reviews 62(11): 1064-1079.

46. Yu, M. K., Y. Y. (2008). "Drug Loaded Superparamagnetic Iron Oxide Nanoparticles for Combined Cancer Imaging and Therapy In Vivo." Angewandte Chemie International Edition 47(29): 5362-5365.
47. Zou, P., Y. YU (2010). "Superparamagnetic iron oxide nanotheranostics for targeted cancer cell imaging and pH-dependent intracellular drug release." Molecular Pharmaceutics

2 TOOLBOX

Chapter 2 TOOLBOX

2.1 Purpose

The purpose of this toolbox is to describe the tools and methodologies necessary for the development and study of porous silicon iron oxide nanocomposite based IGDD (image guided drug delivery) agents. The materials section describes the synthesis of the materials used, computational tools were built for design related analysis of the IGDD system and MRI/NMR tools were used to characterize the nanomaterials. Specifically, NMR (nuclear magnetic resonance) was used to characterize properties of porous silicon. Nuclear magnetic resonance allows the characterization of more multiple properties of this material with a small amount of sample in a matter of minutes.

In the chapters to follow, the below described tools are used to accomplish the following:

1. Synthesize iron oxides, porous silicon, porous silicon iron oxide nanocomposites (2.1, 2.4)
2. Design and simulate characteristics of agents that produce high relaxivity (Sections: 2.5, 2.6)
3. Study the relaxivity effects of loading iron oxide into porous silicon (Sections: 2.1, 2.3, 2.5)

SECTION A: MATERIALS

2.1IRON OXIDE

2.1.1Comparing synthesis methods

2.1.2 Iron oxide synthesis via thermal decomposition

2.1.3Characterization: size distribution

2.2POROUS SILICON

2.3 POROUS SILICON IRON OXIDE NANOCOMPOSITE

SECTION B: COMPUTATIONAL TOOLS

2.4Monte Carlo methods for measuring T2 & T2*

2.5Calculating fractal dimension

SECTION C: MAGNETIC RESONANCE IMAGING

2.6 Considerations in MR imaging

2.7 Measuring T2 on NMR

SECTION A: MATERIALS

2.1- IRON OXIDE

2.1.1 Comparing synthesis techniques

Over the last decade various synthesis techniques have been employed to synthesize monodisperse iron oxide nanoparticles. The table below compares the various synthesis techniques.

Table 2.1: Comparing techniques for the synthesis of iron oxide [49]

Synthetic method	Co-precipitation	Thermal decomposition	Microemulsion	Hydrothermal synthesis
Reaction temp. [°C]	20-90	100-320	20-50	220
Reaction period	Minutes	hours-days	hours	hours ca. days
Solvent	Water	organic compound	organic compound	water-ethanol
Surface-capping agents	needed, added during or after reaction	needed, added during reaction	needed, added during reaction	needed, added during reaction
Size	narrow	very narrow	relatively	Very narrow

Hence, the thermal decomposition method was chosen for synthesis of iron oxides.

2.1.2 Iron oxide synthesis via thermal decomposition

Inspired by the synthesis of high-quality semiconductor nanocrystals and oxides in non-aqueous media by thermal decomposition, similar methods for the synthesis of magnetic particles with control over size and shape have been developed [49]. Monodisperse magnetic nanocrystals with smaller size can essentially be synthesized through the thermal decomposition of organometallic compounds in high-boiling organic solvents containing stabilizing surfactants [50]. The organometallic precursors include metal acetylacetonates, [M(acac)n], (M=Fe, Mn, Co, Ni, Cr; n=2 or 3, acac=acetylacetonate), metal cupferronates [MxCupx] (M=metal ion; Cup=N-nitrosophenylhydroxylamine, $C_6H_5N(NO)O$-),or carbonyls. Fatty acids, oleic acid, and hexadecylamine are often used as surfactants. In principle, the ratios of the starting reagents including organometallic compounds, surfactant, and solvent are the decisive parameters for the control of the size and morphology of magnetic nanoparticles. The reaction temperature, reaction time, as well as aging period may also be crucial for the precise control of size and morphology [49].

If the metal in the precursor is zerovalent, such as in carbonyls, thermal decomposition initially leads to formation of the metal, but two-step procedures

can be used to produce oxide nanoparticles as well. For instance, iron pentacarbonyl can be decomposed in a mixture of octyl ether and oleic acid at 100 °C, subsequent addition of trimethylamine oxide $(CH_3)_3NO$ as a mild oxidant at elevated temperature, results in formation of monodisperse γ-Fe_2O_3 nanocrystals with a size of approximately 13 nm [25]. Decomposition of precursors with cationic metal centers leads directly to the oxides, that is, to Fe_3O_4, if $[Fe(acac)_3]$ is decomposed in the presence of 1,2-hexadecanediol, oleylamine, and oleic acid in phenol ether.

Iron pentacarbonyl ($[Fe(CO)_5]$, also denoted as iron carbonyl) is a metastable organometallic compound whose facile decomposition has made it an extremely useful reagent. The fact that the standard enthalpy of formation of iron pentacarbonyl is only $-185\ \text{kcal mol}^{-1}$ and that the five carbon monoxide subunits each have an enthalpy of formation of $-110.5\ \text{kcal mol}^{-1}$ account for its tendency to dissociate. The molecule is easy to decompose, but the decomposition reaction is extraordinarily complicated. There have been a number of studies on the decomposition of iron pentacarbonyl, but they are of limited use in designing a synthetic system. The decomposition does not always follow a simple pathway, and a range of intermediate iron carbonyls and iron clusters can form and catalyze the decomposition (Figure 1.1). A great many surfactants and other species can also catalyze the decomposition. The result is that the decomposition frequently changes rate and even order during the course of a reaction. This is always a complicating factor when attempting to grow

nanoparticles of controlled size and shape [51].

Despite these complications, the decomposition of iron pentacarbonyl is frequently used in the formation of nanoparticles. This is largely due to the ease of use and the lack of byproducts of this reaction.

Hyeon and co-workers have also used a similar thermal decomposition approach for the preparation of monodisperse iron oxide nanoparticles. They used nontoxic and inexpensive iron(III) chloride and sodium oleate to generate an iron oleate complex in situ which was then decomposed at temperatures between 240 and 320 °C in different solvents, such as 1-hexadecene, octyl ether, 1-octadecene, 1-eicosene, or trioctylamine. Particle sizes are in the range of 5–22 nm, depending on the decomposition temperature and aging period. In this synthesis, aging was found to be a necessary step for the formation of iron oxide nanoparticles [52]. The nanoparticles obtained are dispersible in various organic solvents including hexane and toluene. However, it is unclear whether the particles can also be dispersed in water. The same group found that sequential decomposition of iron pentacarbonyl and the iron oleate complex at different temperature results in the formation of monodisperse iron nanoparticles (6–15 nm) which can be further oxidized to magnetite. The overall process is similar to seed-mediated growth, which can be explained by the classical LaMer mechanism. [53] That is, a short burst of nucleation from a supersaturated solution is followed by the slow growth of particles without any significant additional nucleation, thereby achieving a complete separation of nucleation and growth. In

Hyeon's synthesis, the thermal decomposition of iron pentacarbonyl at relatively low temperature induces nucleation, and the decomposition of the iron oleate complex at a higher temperature leads to growth. The above-mentioned nanoparticles are dispersible in organic solvents. However, water-soluble magnetic nanoparticles are more desirable for applications in biotechnology. For that purpose, a very simple synthesis of water-soluble magnetite nanoparticles was reported recently. Using $FeCl_3 \cdot 6\ H_2O$ as iron source and 2-pyrrolidone as coordinating solvent, water soluble Fe_3O_4 nanocrystals were prepared under reflux (245 °C). The mean particles size can be controlled at 4, 12, and 60 nm, respectively, when the reflux time is 1, 10, and 24 h. With increasing reflux time, the shapes of the particles changed from spherical at early stage to cubic morphologies for longer times.

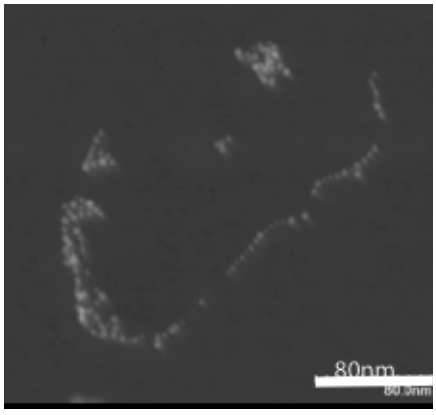

Courtesy: Sabine Faulhaber, Shalini Ananda

Figure 2.1: This is a representation of iron oxide synthesized via thermal decomposition. The average size of the above nanoparticles were calculated to be 9.6nm. A plug-in on Image J was used to calculate average size of the nanoparticles.

2.2: POROUS SILICON

The electrochemical synthesis of porous silicon allows controllable pore sizes making it a suitable material for IGDD application. The below description and figures were modified and obtained from [24] and porous Si in practice.

2.2.1 Preparation and mechanism

Porous Si is a product of an electrochemical anodization of single crystalline Si wafers in a hydrofluoric acid electrolyte solution. Pore morphology and pore size can be varied by controlling the current density, the type and concentration of dopant, the crystalline orientation of the wafer, and the electrolyte concentration in order to form macro-, meso, and micropores [54]. Pore sizes ranging from 1 nm to a few microns can be prepared.

The mechanism of pore formation is not generally agreed upon, but it is thought to involve a combination of electronic and chemical factors [54] Porous silicon can be classified into four groups based on the type and concentration of the dopant: n-type, p-type, highly doped n-type, and highly doped p-type. Highly doped p-type implies that the dopant levels at which the conductivity behavior of the material is more metallic than semiconducting. For n-type silicon wafers with a relatively moderate doping level, exclusion of valence band holes from the space charge region determines the pore diameter. For both dopant types the reaction is crystal face selective, with the pores propagating primarily in the <100>

direction of the single crystal [55].

As shown in Figure 2, the electrochemically driven reaction requires an electrolyte containing hydrofluoric acid. Application of anodic current oxidizes a surface silicon atom, which is then attacked by fluoride. The net process is a 4 electron oxidation, but only two equivalents are supplied by the current source. The other two equivalents come from reduction of protons in the solution by surface SiF_2 species. Pore formation occurs as Si atoms are removed in the form of SiF_4, which reacts with two equivalents of F^- in solution to form SiF_6^{2-}.The porosity of a growing porous Si layer is proportional to the current density being applied, and it typically ranges between 40 and 80%. Pores form only at the Si/porous Si interface, and once formed, the morphology of the pores does not change significantly for the remainder of the etching process. [54].

2.2.2 Optimizing pore size

With porous Si, control over porosity and pore size is obtained by adjusting the current settings during the etch. Typically, larger current density produces larger pores. Large pores are desirable when incorporating sizable molecules or drugs within the pores. Pore size and porosity is important not only for drug loading; it also determines degradation rates of the porous Si host matrix . Smaller pores provide more surface area and expose more sites for attack of aqueous media. The smaller porous filaments within the film yield greater dissolution rates, providing a convenient means to control degradation rates of the porous Si host [55].

2.2.3 Preparation of nanoparticles (Methodology adapted from reference [2]

To prepare particles, the porous layer can be removed from the Si substrate with a procedure is called “electropolishing. The etching electrolyte is replaced with one containing a lower concentration of HF and a current pulse is applied for several seconds. The lower concentration of HF results in a diffusion limited situation that removes silicon from the crystalline Si/porous Si interface faster than pores can propagate. The result is an undercutting of the porous layer, releasing it from the Si substrate. The freestanding porous Si film is subject to ultrasonic fracture to create nanoparticles.

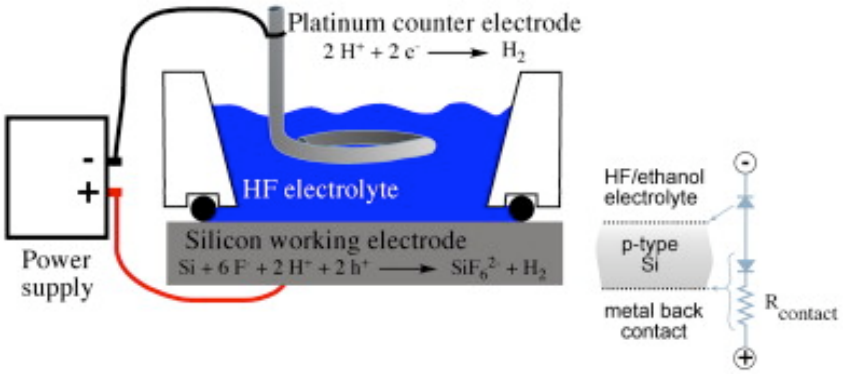

Figure 2.2: Schematic of the etch cell used to prepare porous silicon

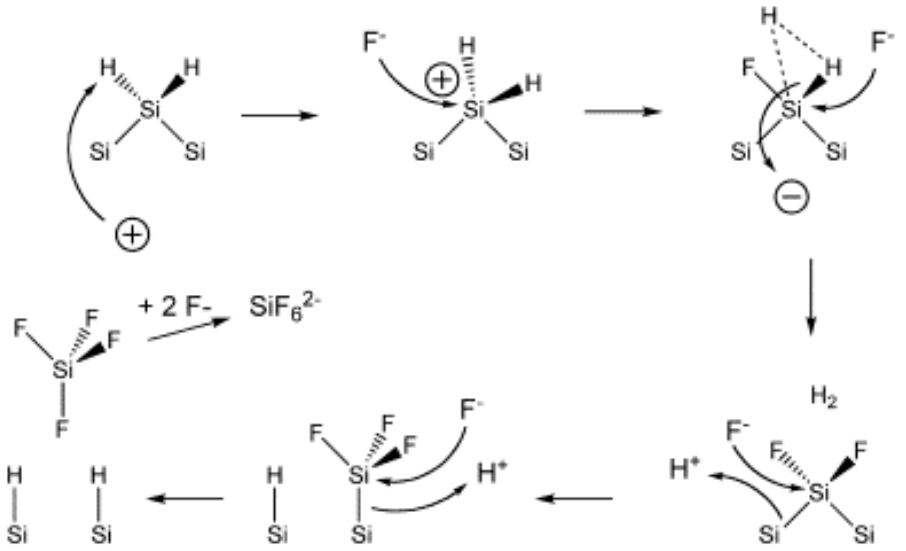

Fig. 2.3. Mechanism of Si oxidation during the formation of porous Si (adapted from [24]).

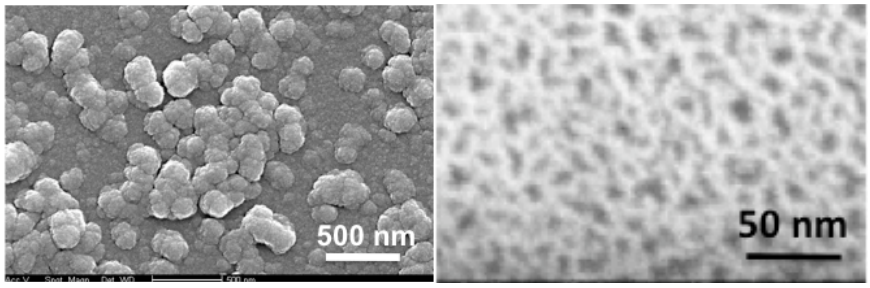

Courtesy: Ryan Anderson, Shalini Ananda

Figure 2.4: SEM images of a) size distribution of porous silicon nanoparticles b) Porous nanostructure of porous silicon (average pore size of 18.7nm)

2.3: POROUS SILICON IRON OXIDE NANOCOMPOSITE

2.3.1 Preparation of porous silicon iron oxide nanocomposites

Porous silicon nanoparticles were prepared as described in previous study [2]. Nanoparticles were generated by sonicating the freestanding pSi film in a sealed vial of ethanol (≈10 mg mL^{-1}) for 16 h at room temperature.

The solution was then centrifuged at 10 000 RPM and the pellet was resuspended in ethanol to create a 10 mg mL^{-1} solution. The resuspended solution was then filtered through a 0.22 μm PVDF syringe filter (Millipore, USA). A solution (1 mL) of oleic acid-coated Fe_3O_4 particles (2 mg mL^{-1}) in choloroform (Fisher, USA), were added to the pSi suspension (2 mg mL^{-1}) in chloroform and the solution was gently agitated for 12 h. After removing the suspension from agitation, the chloroform was evaporated and the film was redispersed in ethanol and purified by successive centrifugation three times at 14 000 RPM for 30 min. The product was collected as a pellet and then thermally oxidized at 180 °C for 4 h. The Fe_3O_4:pSi nanocomposite particles were then coated with methoxy PEG-silane (MW = 5,000, Laysan Bio, USA) chloroform solution (10 ml) that was agitated on a vortex at RT overnight. The solution was purified by centrifugal filtration against a 100 kDa MW (Millipore Amicon Ultra-4, Billerica, MA) filter for 30 min at 6000 RPM.

Section B: COMPUTATIONAL TOOLS

2.4. Simulating T2 and T2* for aggregates: Monte carlo simulation

2.5. Morphology of an aggregate

2.4. Monte Carlo Simulation of tranverse magnetization

Nomenclature:

D- diffusion coefficient

d- distance between two nanoparticles

f - fractal volume

R – particle radius

$\frac{\tau_D R^2}{D}$ - diffusion correlation time

γ - proton gyromagnetic ratio

τ_{CP} - echo time

R- radius of gyration

Monte Carlo simulations were carried out in order to predict R_2 and R2*. Prior to this study, authors used this method to study the effect of size on IONP's on relaxivity. [56]. The tool box describes the algorithm, the equations used and simulation parameters.

The algorithm is composed of:

a) Water proton spins diffuse within the system and their dephasing is calculated.
b) The FID decay is calculated from the evolution of the mean value of the magnetic moment component that produces the signal.

The simulation space is composed of a central cubic space whose dimension is determined by the volume fraction and the number of IONP particles simulated. An overlap between adjacent aggregates is allowed.

Random walk simulates water proton translations for randomly distributed IONP particles; at each time step $t_n = n\Delta t$ (where n is an integer), the corresponding water proton position is determined by adding a random step to the previous position:

$$\vec{r}(t_n) = \vec{r}(t_n - 1) + \vec{\delta}_n \quad \text{(Equation 1)}$$

with $\left|\vec{\delta}_n\right| = \sqrt{6D\Delta t}$

is a randomly oriented vector on a sphere with radius r . The initial position is placed randomly in the central cube. Any jump leading to the positioning of the water proton inside a magnetic particle is not allowed.

If $\vec{r}(t_n)$ is located outside of the central cube, it is instantaneously relocated to the position corresponding to the opposite face of the cube.

During the diffusion, the local magnetic field felt by the proton spin induces a local Larmor precession of its magnetic moment, which results in a rotation in the xy-plane: dephasing. This dephasing is proportional to the z-component of the local magnetic field felt by the proton, which is itself the sum of all dipolar magnetic fields produced by the IONP particles:

$$B_{tot}(\vec{r}) = \sum_i B(r_i, \theta_i) \quad \text{(Equation 2)}$$

Then we can infer:

$$B(r;\theta) = R^3 B \frac{3\cos^2\theta - 1}{r^3} \quad \text{(Equation 3)}$$

where R is the IONP radius, r is the distance between the proton spin, the IONP particle and θ the inclination angle of the vector joining the proton spin to the IONP particle. Thus the dephasing for the jth proton spin is given by

$$\Delta\phi_n^j = \gamma_1 B(\vec{r}_j(t_n))\Delta t \quad \text{(Equation 4)}$$

where is the position of the jth proton spin at time t_n. For an initial pulse around the y-axis in the rotating frame, the normalized transverse magnetic moment of the j water proton in the rotating frame is thus

$$\vec{\mu}_j(t_n) = (\cos\theta_n^j, \sin\theta_n^j, 0) \quad \text{(Equation 5)}$$

The magnetic moment must rigorously be interpreted as the average spin of a pack of protons following the same diffusion trajectory.

The normalized FID is then reconstructed by taking the modulus of the transverse magnetic moment average over all the $N_{protons}$ proton spins for each tn:

$$\langle \mu(t_n) \rangle = \frac{1}{N} \sqrt{(\sum_j \cos \phi_n^j)^2 + (\sum_j \sin \phi_n^j)^2} \quad \text{(Equation 6)}$$

The resulting FID is then fitted by a mono-exponential, giving the simulated R_2. If the corresponding reduced chisquare is greater than 0.0001, a double-exponential is used and R_2 is given by the relaxation rate of the mode with the largest amplitude.

Simulation parameters are:

- The diffusion coefficient of water at 310°K: D = $3 * 10^{-9} m^2 / s$
- A volume fraction f of 3.14×10^{-6} .
- An inter-echo time (time between two 180° pulse) of 2τCP=1ms.
- Number of protons : from 5000 to 20,000.

For each set of parameters, three different simulations are made: each data point is the mean of three simulated values.

2.5: Morphology of an aggregate

Calculating radius of gyration and fractal dimension of aggregates determine the morphology of an aggregates and is used in conjunction with using Monte Carlo simulations to determine R2 and R2*. Computing the Fractal dimension of 2D shapes can be useful in accurately determining the radius of gyration for nanoparticle aggregates

Nomenclature

A	Primary particle radius
A_a	Project area of an aggregate
A_p	cross sectional area of particle
C_{ov}	overlap coefficient
d_p	diameter of primary particle
d_{ij}	distance between two particles
d_p	Primary particle diameter
D_f	aggregate fractal dimension
k_g	fractal pre-factor
k_a	projected area pre factor
k_L	fractal pre-fractor based on L
L	projected maxium length of aggregate
N	Number of particles in an aggregate
R_g	radius of gyration of an aggregate
S_a	aggregate total exposed surface

Precalculation:

Cross sectional area of a primary particle:

$$A_p = \frac{\pi d_p^2}{4}$$

Greek symbol:

α_a is projected area exponent

In particular, for fractal-like aggregates, the number of primary particles in an aggregate, N, scales with the radius of gyration, R_g, as follows:

$N = k_g (R_g / a)^{D_f}$ v (Equation 1)

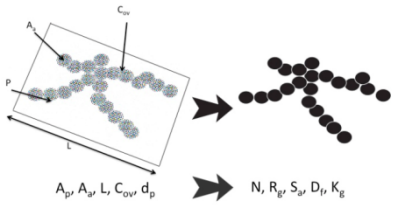

Figure 2.5 describes the main variables measured from the projected image to infer three dimensional structural properties

The following steps were taken to calculate structural properties of an aggregate:

(i) Measure L, a and A_a. The primary particle radius has to be measured after identifying several individual monomers and calculating the mean value.

(ii) Estimate N using equation . A_a, C_{ov} and a were input.

$N = k_a (A_a / A_p)^{\alpha_a}$ (Equation 2)

(iii) Estimate Rg with a and L

$L/(2R_g) = 1.50 \pm 0.05$ (Equation 3)

(iv) Estimate S using equation A_a, a N and C_{ov}

$S_a / S_{(C_{ov}=0)} = 1 - \phi Cov(1 - 1/N)$ here ϕ = 1.3 (Equation 4)

(v) Now, plot on a log-log scale N versus L/2a. Estimate the best fit and obtain D_{fl} (the slope) and KL (the magnitude of the least-square linear fit to the data).

(vi) Obtain fraction dimension D_f

$Df = D_{fL} = \ln(N / k_L) / \ln(L / 2a)$ (Equation 5)

(vii) Obtain k_g

$k_g = k_L (1.5)^{D_f}$ (Equation 6)

SECTION C: MAGNETIC RESONANCE IMAGING AND NMR:

Iron oxide is used as a contrast agent for magnetic resonance imaging. Principles of magnetic resonance imaging were described in Chapter 1.

2.6: Considerations for MR Imaging

2.6.1 Coils

The coils of wire used for detection are called RF coils because they are designed to resonate at radio frequencies—specifically, at the Larmor frequency. Specialized coils are crafted for different applications so that they are as small as possible for any given part of the body [58]. The coil should be compact and close to the area of interest because larger coils produce noisier images. Conversely, smaller coils can only detect signals from smaller regions [44].

The efficiency of detection can be increased by the proper choice of RF coils. Small coils are less noisy than large ones, but they can only detect signal from a limited area. Recent advances have led to phased array coils, sets of coils that act independently but together measure signal from a wide area. Signal detection with a large set of small coils is typically less noisy than that obtained with one large coil. The drawback of phased array coils is the added hardware and computer power necessary to process multiple signals [59]. The strength of the current that is measured as the MR signal is directly related to the amount of spin magnetization precessing in the scanner. After the spins are excited by the RF pulse and begin precessing, several things happen that affect the MR signal [44].

The spins immediately begin to precess at a Larmor frequency exactly proportional to the local magnetic field strength. The spins realign themselves with the magnetic field B_0 after a couple of seconds while the precessing magnetization (and the associated signal) fades in about 0.10 second. The second two processes are called relaxation and are characterized by the time constant T2, respectively [60].

2.6.2 SNR

a (voxel size)*(imaging time)1/2 [43]

where the size of a voxel (short for volume element, the three-dimensional equivalent of a picture element, or pixel) is given by the product of the two in-plane resolutions multiplied by the slice thickness [44]. For example, if an MR image is collected with in-plane resolution decreased from 1.0 mm2 to 0.5 mm2, SNR is reduced by a factor of four but can be restored by increasing imaging time sixteen fold.

The equation represents an unbreakable physical barrier. Technological barriers, however, lower the SNR from its optimal state for a given voxel size and imaging time and limit the minimum resolution and imaging time [59] .

2.6.3 Increasing SNR

A high SNR for a fixed voxel size and imaging time can be obtained by increasing in vivo magnetization or the efficiency of detection [44]. Magnetization can be increased by increasing the magnetic field B_0 in which the patient is being

scanned. The fraction of parallel, or detectable spins (roughly 10/million), is proportional to B0. Doubling the magnet strength of a scanner doubles this fraction and doubles the MR imaging signal to a first approximation [60]. Higher manufacturing costs, patient safety, and other field strength-related phenomena are hindrances to using higher field strengths, but the simple notion that doubling the SNR can reduce scan time by a factor of four (from the above equation) for many scans is a powerful motivator.

2.6.4 Imaging Time

Imaging time is limited by how fast all the spatial waves in k-space necessary to complete an image with the desired resolution can be collected. These waves are produced by turning on the field gradients. Stronger field gradients can produce a greater variety of waves in a shorter amount of time than can weaker field gradients [59]. To measure a two-dimensional set of waves, these gradients must be able to change direction rapidly so that the signal can be sampled over all of k-space. Thus, larger gradient amplitudes and gradients with higher slew rates (the rate at which the gradient can change direction) allow data to be collected more rapidly. Smarter sampling strategies (e.g., sampling trajectories through k-space) also help reduce imaging time.

2.6.5 Resolution

Other than limited SNR, which is a significant limitation to high-resolution MR images, other barriers are surmountable. Higher resolution scans require more computer memory and faster computer processing. A set of 128 slices, each producing a 512 x 512 pixel image and sampled from a four-element phased array coil set, requires about a gigabyte of memory. This is now possible but was less feasible just 5 years ago. [44].

Another barrier to improved resolution is physiologic motion from bulk motion, peristalsis, respiratory motion, and cardiac motion. The different time scales of these motions present different challenges for collecting data. Physiological motion can be circumvented in three ways. First, the motion can be monitored and the imaging data collected only during a quiescent period when tissues are assumed to return to the same state [43]. Second, the motion can be monitored and corrected when the image is reconstructed. Finally, the image data can be collected fast enough to avoid the motion. The first scheme has been the basic way to obtain routine images in the abdomen, with the use of cardiac and respiratory gating [43].

2.6.6 Repetition Time(TR) and Spin realignment

MR images take time to collect. Typically, spins must be excited many times, each time producing a slightly different measurement. The first relaxation mechanism, namely the longitudinal realignment of the excited spins with B0,

must be allowed to occur (to some degree) between each excitation. Otherwise, there is insufficient `realigned' magnetization available for the excitations that follow and the resulting signal is diminished [43]. The cause of this spin realignment is known as spin-lattice relaxation [44]. As nuclei oscillate and tumble in their molecular sea, they pass through locally changing magnetic fields. When a component of that motion is at the Larmor frequency through one of these changing magnetic fields, the nucleus `sees' an effective resonant RF pulse that rotates it out of its current state [59]. The collection of these randomly oriented RF pulses serves to speed the nuclear spin states toward their preferred alignment much like shaking a box of balls moves heavy balls to the bottom and light ones to the top.

2.6.7 Echo Time(TE) and Signal Loss

The realignment of spins toward a direction parallel to B0 naturally removes them from the plane transverse to B0, in which they precess to form the MR image signal. Therefore, the signal decays as the spins realign due to spin-lattice relaxation [59]. An additional mechanism, however, dominates this transverse decay and can be explained by recalling that the frequency of spin precession is proportional to the local magnetic field. The molecular environment in which protons move has variations in the magnetic field[43]. Thus, the precession of each spin is always speeding up and slowing down as it moves through these fields, slowly losing magnetic alignment with neighboring spins. This loss of spin coherence on a molecular scale is called spin-spin relaxation [44]. The total loss of

precessing (signal-producing) magnetization due to spin-lattice and spin-spin relaxation (the latter being the dominant mechanism) is characterized by the time constant T2, the time required for 63% of the precessing magnetization to decay [43]. The amount of signal decay depends on T2 and the time between the spin excitation and the measurement of the induced current in the coil, known as echo time (TE). The TE/T2 ratio indicates the relative fraction of precessing magnetization (and therefore of the available signal) that remains at the time of measurement [43].

2.6.8 Dephasing and Spin Echo

As excited spins move about the molecular landscape, the final phase angle that their magnetism is directed at the time of signal measurement reflects the average frequency at which they have precessed. In turn, this value reflects the average magnetic field strength to which they have been exposed. This magnetic field not only changes on a molecular scale (responsible for T2 relaxation), it also changes more slowly on a macroscopic scale [43]. Thus, any region will have variations in the final phase of its spins, and its composite signal from all of these spins will be reduced. This signal loss is typically referred to as spin dephasing, and its rate, along with the less significant (in this context) mechanisms of spin-lattice and spin-spin relaxation, is characterized by the time constant T2*[43]. Although the loss of signal strength from T2 relaxation is unavoidable, the loss of signal from spin dephasing (T2*) can be reversed. The same applied resonant RF pulse that excited the spins can reverse the phase of all spins in the

transverse plane [44]. This 180º refocusing RF pulse puts the faster-precessing spins behind the slower ones. If 10 msec elapse after the initial spin excitation before this refocusing pulse is applied, the fast spins will catch up to the slow spins 10 msec after the refocusing pulse. Once again a coherent set of spins is created in what is called a spin echo [43]. Data collection schemes with and without this refocusing pulse are called spin-echo and gradient-echo pulse sequences, respectively. The use of this rephasing is very important in regions of magnetic field inhomogeneity if TE is very long. Rephasing works only if `fast' spins remain fast before and after the refocusing pulse. These RF pulses do not refocus the dephasing that creates spin-spin (T2) relaxation, because it is caused by field changes on a molecular scale, and spins are speeding up and slowing down far too quickly to be refocused coherently [44].

2.6.9 T2, T2* weighted images and relaxation times.

This section summarizes the acquisition of T2 and T2* weighted images and provides equations to be used to measure T2 relaxation times.

Table 2.2: Choice of TR and TE for conventional spin echo [43],[44]

TR	TE – short Less than 40ms	Long TE More than 45ms
Long – more than 1500ms		T2 weighted

Table 2.3: Choice if TR, TE and flip angle for gradient echo sequences

Flip angle	TE less than 15ms	Long more than 30ms
Small less than 40		T2* weighted

The T2 relaxation time constant characterizes the rate at which the Mxy component decays.

$$M_{xy}(t) = M_{xy}(0)\exp^{-t/T2} \quad \text{(Equation 3)}$$

$$\frac{dM_{xy}(t)}{dt} = -\frac{M_{xy}(t)}{T2} \quad \text{(Equation 4)}$$

T2* decay depends on both the external magnetic field and spin –spin interaction while T2 decays depends primarily on spin-spin interactions.

$$\frac{1}{T_2*} = \frac{1}{T_2} + \gamma\Delta B \quad \text{(Equation 5)}$$

2.6.10: NMR for characterizing porous silicon

This thesis used T2 measurements from a nuclear magnetic resonance spectrometer to characterize properties of porous silicon such as pore size, pore volume. The PSG sequence can be used to characterize diffusion coefficient. An

advantage of using nuclear magnetic resonance to study porous characteristics of materials over conventional techniques is the relatively small quantity of sample needed and quick data acquisition.

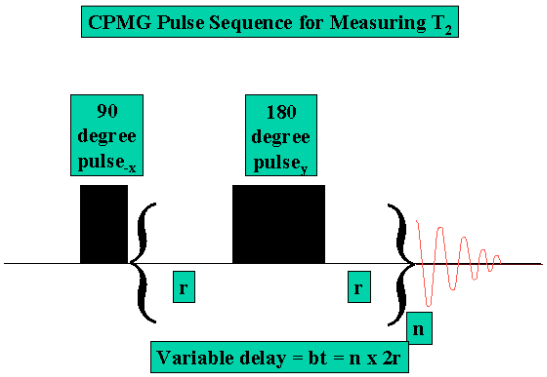

Figure 2.6: A CPMG sequence to measure T2 [61]

The sequence consists of a 90° rf followed by a series of 180° rf pulses each followed by acquisition. The first pulses excites the magnetization vector and tilts magnetization into the transverse plane. The magnetization is affected by T2 NMR relaxation during the time periods, τ, before and after the second pulse. The 2D cpmg calls a list known as “vclist” found in the Topspin/exp/lists folder. This is a list of integers which refers to the number of vc loops that are completed before the signal is acquired. Looping over this part of the sequence essentially extends the time period in which T2 NMR relaxation affects the signal. The reduction of signal due to relaxation can then be measured as a function of t = 2n τ, where n is the number of vc loops.

The relationship between this reduction of signal or attenuation (Ψ), τ, and the T2 NMR relaxation time would be:

$$\Psi \propto \exp\left(-\frac{\tau}{T_2}\right)$$ (Equation 1)

So an exponential fit of the attenuation data as a function of τ will yield the T2 NMR relaxation time for the sample. The values of D20 should be determined such there is both sufficient attenuation over the course of the 2D experiment. At the same time, D20 should be short enough to prevent all signal from attenuating before the end of the 2D sequence.

REFERENCES:

1. Laurent, S.; Forge, D.; Port, M.; Roch, A.; Robic, C.; Vander Elst, L.; Muller, R. N., Magnetic iron oxide nanoparticles: synthesis, stabilization, vectorization, physicochemical characterizations, and biological applications. Chemical reviews 2008, 108 (6), 2064-2110.

2. Corot, C.; Robert, P.; Idee, J. M.; Port, M., Recent advances in iron oxide nanocrystal technology for medical imaging. Advanced drug delivery reviews 2006, 58 (14), 1471-1504.

3. Kim, D.; Zhang, Y.; Voit, W.; Rao, K.; Muhammed, M., Synthesis and characterization of surfactant-coated superparamagnetic monodispersed iron oxide nanoparticles. Journal of magnetism and Magnetic Materials 2001, 225 (1), 30-36.

4. Bronstein, L. M.; Huang, X.; Retrum, J.; Schmucker, A.; Pink, M.; Stein, B. D.; Dragnea, B., Influence of iron oleate complex structure on iron oxide nanoparticle formation. Chemistry of materials 2007, 19 (15), 3624-3632.

5. Park, J.; An, K.; Hwang, Y.; Park, J. G.; Noh, H. J.; Kim, J. Y.; Park, J. H.; Hwang, N. M.; Hyeon, T., Ultra-large-scale syntheses of monodisperse nanocrystals. Nature Materials 2004, 3 (12), 891-895.

6. William, W. Y.; Falkner, J. C.; Yavuz, C. T.; Colvin, V. L., Synthesis of monodisperse iron oxide nanocrystals by thermal decomposition of iron carboxylate salts. Chemical communications 2004, (20), 2306-2307.

7. Anglin, E. J.; Cheng, L.; Freeman, W. R.; Sailor, M. J., Porous silicon in drug delivery devices and materials. Advanced drug delivery reviews 2008, 60 (11), 1266-1277.

8. Canham, L., Properties of porous silicon. IEE Books: 1997; Vol. 4.

9. Searson, P.; Macaulay, J.; Prokes, S. M., The formation, morphology, and optical properties of porous silicon structures. Journal of The Electrochemical Society 1992, 139, 3373.

10. Park, J. H.; Gu, L.; von Maltzahn, G.; Ruoslahti, E.; Bhatia, S. N.; Sailor, M. J., Biodegradable luminescent porous silicon nanoparticles for in vivo applications. Nature materials 2009, 8 (4), 331-336.

11. Granitzer, P.; Rumpf, K.; Roca, A.; Morales, M.; Poelt, P.; Albu, M., Magnetite nanoparticles embedded in biodegradable porous silicon. Journal of Magnetism and Magnetic Materials 2010, 322 (9-12), 1343-1346.

12. Gillis, P.; Moiny, F.; Brooks, R. A., On T2,Äêshortening by strongly magnetized spheres: A partial refocusing model. Magnetic resonance in medicine 2002, 47 (2), 257-263.

14. Washington, C., Drug release from microdisperse systems: a critical review. International journal of pharmaceutics 1990, 58 (1), 1-12.

15. Edelman, R. R.; Warach, S., Magnetic resonance imaging. New England Journal of Medicine 1993, 328 (10), 708-716.

16. Hashemi, R. H.; Bradley, W. G.; Lisanti, C. J., MRI: the basics. Lippincott Williams & Wilkins: 2010.

17. Westbrook, C., MRI at a glance. Wiley-Blackwell: 2009; Vol. 17.

18. Mitchell, D. G.; Cohen, M. S., MRI principles. Saunders: 1999.

19. McRobbie, D. W., MRI from picture to proton. Cambridge Univ Pr: 2003.

20. Fukushima, E.; Roeder, S. B. W., Experimental pulse NMR: a nuts and bolts approach. Addison-Wesley Reading, MA:: 1981.

21. Callaghan, P. T., Principles of nuclear magnetic resonance microscopy. Clarendon Press Oxford: 1993.

22. Morris, P. G., Nuclear magnetic resonance imaging in medicine and biology. Clarendon Press Oxford, UK: 1986.

23. Strange, J.; Rahman, M.; Smith, E., Characterization of porous solids by NMR. Physical review letters 1993, 71 (21), 3589-3591.

24. Timur, A., Pulsed nuclear magnetic resonance studies of porosity, movable fluid, and permeability of sandstones. Journal of Petroleum Technology 1969, 21 (6), 775-786.

25. Bovey, F. A.; Jelinski, L.; Mirau, P. A.; Telephone, A.; Company, T., Nuclear magnetic resonance spectroscopy. Academic Press New York: 1969.

3 CONSTRUCTING IRON OXIDE AGGREGATES TO INCREASE R2* RELAXATION RATE: A MONTE CARLO STUDY

CHAPTER 3 CONSTRUCTING IRON OXIDE AGGREGATES TO INCREASE R2* RELAXATION RATE: A MONTE CARLO STUDY

3.1 Abstract

3.2 Introduction

3.3 Theory

3.4 Methods

3.5 Results and Discussion

3.6 Conclusion

3.1 Abstract

The transverse relaxation of protons diffusing among magnetic particles depends on the size of magnetic particle aggregates. Two distinct regimes for R2* or transverse relaxation measurements are: 1) a mechanism where R2* increases with the radius of the particle (motion averaged regime - MAR) and 2) R2* stays constant after a critical size (static dephasing regime - SDR). Using Monte-Carlo simulations, this study compares R2* induced by nanoparticle aggregate systems of uncoated 9nm nanoparticles with different geometrical configuration to determine the nanoparticle aggregate configuration that generates the maximum R2*.

3.2 INTRODUCTION

Superparamagnetic iron oxide nanoparticles are used as contrast agents in magnetic resonance imaging (MRI) to enhance the image contrast. These agents introduce inhomogeneities in the magnetic field causing protons to rapidly lose their phase coherence[62], thereby leading to signal voids in areas where SPIO aggregate.[63]. Previous studies have described agents made up of superparamagnetic iron oxide nanoparticles of size 25nm encapsulated in a polymer or in silica [64]. New methods of preparing clusters of densely packed superparamagnetic nanoparticles have been reported [65]. Clusters of nanoparticles retain their superparamagnetic properties despite their overall large diameters (i.e., 30–200 nm)[66]. A look into the mechanisms that governs the performances of these contrast agents should help us move closer towards constructing agents with higher R2* [64].

The rate of dephasing can be roughly broken into two regimes: 1) the motion averaged regime (MAR) in which proton diffusion is the dominant factor affecting contrast and applies to nanoparticles under 30nm and 2) the static dephasing regime (SDR) in which the relaxation rate is independent of diffusion because the scale of the magnetic field inhomogeneities is large. At large particle sizes in SDR, the distance traveled by diffusion is negligible compared with the magnetic field inhomogeneity introduced by the particle. [67]

The dynamics of intermediate sizes were examined in 2002 by Brooks, who divided space around the particles into inner zones of rapid dephasing and outer

zones of quiet [68]. Protons that reach the inner zone are rapidly dephased while those outside dephase only minimal amounts. [69].

With regards to optimal size of nanoparticles for in vivo application, it is currently thought that the diameter of nanoparticle therapeutics for cancer should be greater than 10 nm [70]. This estimation is based on the measurement of sieving coefficients for the glomerular capillary wall, as it is estimated that the threshold for first-pass elimination by the kidneys is 10 nm (diameter)[71]. The vasculature in tumors is known to be leaky to macromolecules. The lymph system of tumors in mouse models is poorly operational and macromolecules leaking from the blood vessels accumulate — a phenomenon known as "enhanced permeability and retention (EPR) effect". It has been shown that entities on the order of hundreds of nanometer in size can leak out of the blood vessels and accumulate within tumors. However, large macromolecules or nanoparticles could have limited diffusion in the extracellular space [71]. These nanoparticles will be restricted from exiting normal vasculature (that requires sizes less than 1–2 nm); however they will still be able to access the liver, as entities up to 100–150 nm in diameter are able to do so [35].

A number of theoretical and experimental studies devoted to examining the effect that iron oxide nanoparticles have on the transverse relaxation rate (R^*_2) of water protons have demonstrated that the size of the SPION (superparamagnetic iron oxide nanocomposite) aggregates are key factors influencing the relaxation rate [64, 72]. In this study, we look into the effect of the geometrical structure of iron

oxide nanoparticle aggregates on relaxation rates. We start by systematically studying single iron oxide nanoparticles in a linear and circular configuration. It has been reported previously that a nanoparticle aggregate of size >18.4nm exits the motion averaged regime[73]. To explore this understanding with regard to generating aggregates, we compare the relaxation rates of two systems when their respective single 'units' are added to the system one at a time in a linear, circular and cluster configuration. The single units of the different systems are: 1) Two 9nm nanoparticles (18nm in x-axis and 9nm in y-axis), 2) Three 9nm nanoparticles (18nm in x and y axis). Obtaining the static limit of above described systems provided insight into specifications for creating naoparticle aggregate clusters with high relaxation rate. Then, based on these specifications, 200nm clusters of different geometrical configurations were generated and relaxation times of the clusters were compared.

3.3 Theory:

Measuring R2* and dephasing of protons:

Iron oxide nanoparticles introduce inhomogeneities into a uniform magnetic field. We can model the particles as dipoles of radius R.

The z component of the magnetic field is

$$B = \frac{\mu_0 M}{3}\left(\frac{R}{r}\right)^3\left(3\cos^2(\theta)-1\right)$$ (Equation 1)

where μ_0 is the permeability of free space at $4\pi \times 10^{-7} H/m$, M is the magnetization of the particle, r is he distance from the particle center and θ is the angle in the z direction.

Following the application of a radio frequency pulse at 90^0 in the direction of the field of the magnet, the protons precess in phase at the Larmor frequency which is:

$$\omega = \gamma B_0$$ (Equation 3)

where γ is the gyromagnetic ratio of protons and is 2.67 x 10^8 s^{-1} T^{-1}. Without iron oxide nanoparticles, the protons will gradually go out of phase due to proton-proton interactions and inhomogenieities in the magnet. These processes are slow and generally yield a low R2*. Iron oxide nanoparticles accelerate this process and held produce a high characteristic R2*.The protons precessing in phase at the Larmor frequency due to the external magnetic field, experience

change in the phase of the individual protons due to the presence of magnetic nanoparticles. If, we quite simply consider the protons precessing in phase at the Larmor frequency as determined by the external magnetic field, the effect of particles can be seen as local perturbations which continuously change the phase of individual protons. Then, the evolution of the phase of a single protons during the time Δt is given by:

$\Delta\phi = \gamma B \Delta t$ (Equation 3),

where γ is the gyromagnetic ratio and is $2.67*10^8$ for water protons.

Dephasing mechanisms: Spin dephasing is understood by two mechanisms: motion averaged regime and static dephasing regime. The range of particle sizes and the dephasing mechanism that corresponds to them can be accounted for by the following parameters: the static limit, the relative distance traveled by diffusion and the effective radius near an iron oxide nanoparticles where the field magnitude created by iron oxide nanoparticles is greater than the external field.

In motional averaged regime, the relaxation rate is given by the outer sphere theory:

$$\frac{1}{T_2} = \left(\frac{4}{9}\right) v \tau_D \left(\Delta\omega_r\right)^2 \text{ (Equation 4)}$$

where v is the volume occupied by the magnetizes spheres. The condition is valid as long as mean Larmor frequency shit at the particle surface and time constant for water diffusion $\left(\Delta\omega_r \tau_D < 1\right)$ is satisfied provided that relaxation in not

interrupted by refocusing echo pulses. This condition is satisfied for uncoated iron oxide nanoparticles smaller than approximately 30nm.

The static dephasing regimes considers the protons as moving very minimal distances. The characteristics of such a system is given by:

$R_D = \sqrt{6D\tau_{sl}}$ where D is the diffusion coefficient taken to be 2.5 x 10^{-9} m^2/s corresponding to bulk water, R_D is the distance traveled by diffusion and τ_{sl} is the shortest possible relaxation time. If the particles are large enough that diffusion of protons are small compared to the interparticle distance between aggregates or $R_D / l << 1$, then the majority of the protons each experience a common magnetic environment. As a consequence, the relaxation rate is unaffected by the diffusio of protons and the rate remains near the value given at the static limit.

Exploring parameters relevant to constructing aggregates:

The relaxation rate behavior of nanoparticles at different size and aggregate configurations will be determined by several other parameters: distance traveled by diffusion, MAR/SDR critical size, the visit limited mechanism and static limit. These parameters are described below:

The static limit. The static limit describes the protons as being fixed in a place. In this scenario, the protons would experience a constant magnetic field. The value for R2* can be obtained using the following equation[67]:

$R_2^* = 1.21 f \Delta\omega_0$ (Equation 5)

where f is the volume fraction of particles and $\Delta\omega_0$ is the Larmor shift on the particle surface. As the protons are confined, the static limit would be the upper limit for the R2* value. The * indicates the absence of a refocussing pulse and corresponds to the T2* relaxation time.

Distance traveled by diffusion: To explore this further: letting τ_{sl} as the distance traveled by a proton in a given relaxation time and R_D (distance traveled due to diffusion), the average distance traveled by a protons in a given relaxation time can be written as:

$$R_D = \sqrt{6D\tau_{sl}} \quad \text{(Equation 6)}$$

Here, D is the diffusion coefficient of the proton and D= 2.5 x 10^{-9} m^2/s.

We are able to see here that R_D is independent on the size of the size of the particle if the input value for τ_{sl} is really small. However, the distance travelled by diffusion relative to the distance separating the particles changes with particle size.

To calculate this, a characteristic interparticle distance can be described in the following manner: letting f as volume fraction, l as the distance between particles and R as the radius of the particle, we can write the relationship between interparticle distance and radius of a particle as:

$$l = \left(\frac{\frac{4}{3}\pi}{f} \right)^{\frac{1}{3}} R \quad \text{(Equation 7)}$$

where f, the volume fraction is fixed and $f = \frac{Nv}{V}$.

Here N is the number of particles, v is the volume per particle and V is the total volume of the system The separation between particles increases as radius of the particle increases. Also, R_D/l will scale as 1/R showing that relative distance travelled by diffusion decreases with increasing particle size.

The critical size to transition from MAR/SDR: We now look at a third parameter that's relevant towards designing constructs.

The upper boundary of motion averaging regime was calculated using the intersection between MAR and static limit and was calculated to be 18.4 nm [5]

This can be found by finding the intersection between R2* curve of the motion averaged regime and the static limit (Equation 5) and then solving from the critical size:

$$R_{criticalsize} = \sqrt{\frac{3.4D}{\Delta\omega_0}}$$

This yields an answer of 17nm and is close to 18.4nm calculated previously.

The visit limited mechanism: In the static dephasing regime, protons diffuse minimal distance. R2* remains at the static limit independent of the interparticle

distance (l) and independent of R (radius). In MAR, the proton visits many magnetic environments before being fully dephases. In this process, it undergoes refocusing and R2* drops with increasing R and l. In a previous study[68], a nanoparticle of R= 30nm was studies and the characteristic separation between particles was l = 3.3um. The average distance traveled by a proton by diffusion is R_D = 11.7um and hence R_D/l ~ 3.5. This protons would experience different magnetic environments and it is unlikely that it will be fully dephased while within its initial magnetic environment as in static dephasing. The measuring R2* value is still near the static limit indicating that the dephasing mechanism is not that of the MAR because diffusion induced refocusing does not have an effect here. Therefore, it seems evident that there is another dephasing mechanism or a transition mechanism between MAR and SDR. Brooks defined the cross over from MAR to SDR as the visit limiting mechanism. In this mechanism, protons are fully dephased before reaching a significantly different magnetic environment and R2* remains at the static limit independent of the interparticle distance.

Through monte carlo simulation, this study explores the static limit of aggregates of uncoated iron oxide nanoparticles arranged in a linear, circular and clustered configuration. This knowledge is utilized to construct aggregates with a configuration that would place their relaxation mechanism between MAR and SDR. Since the upper boundary of the MAR is defined at 18.4nm, we chose a cluster of 3 nanoparticles with a radius of gyration <18.4nm as the basic building block for our constructs. The size of this aggregate would place it in the upper

boundary of motion averaging regime. We then compare the R2* of the constructs to determine the configuration of nanoparticles with the highest R2*.

3.4 Methods: Simulation

In this study, the parameters are chosen as magnetization of the particle (M) = $2.58 \times 10^5 T/m^3$ and volume fraction, f = 3.14×10^{-6} and a relaxation time of τSL = 0.009s. Note that these values are chosen based on previous experimental studies[63].

3.4.1 Calculating average R^*_2

For each system realization, N = 100 nanoparticles are placed within a cubic simulation cell with length, L, determined by the volume fraction f and particle size R according to

$$L = N^{\frac{1}{3}} l = \left(\frac{N \frac{4}{3} \pi}{f} \right)^{\frac{1}{3}} R \quad \text{(Equation 9)}$$

The nanoparticles are placed at random positions, but are not allowed to overlap. A proton is then placed at a random location within this system (overlapping with a nanoparticle is explicitly excluded). The trajectory of the proton is evolved in

time steps of Δt = 1 ns where at each time step, the proton jumps a distance d_r given by

$$dr = \sqrt{6D\Delta t} \quad \text{(Equation 10)}$$

in a random direction. In the case of a collision with a nanoparticle, the jump is rejected and the proton is left in the place the jump originated. Periodic boundary conditions are used to wrap the proton back into the central cell when the proton jumps out of the system [74].

At each step of the trajectory, the net magnetic field from the nearby nanoparticles is calculated. Periodic boundary conditions are used to replicate the system in x, y and z to avoid artifacts at the simulation cell edges. The associated change in phase during the step is approximated by [75]

$$\Delta\phi = \gamma B\Delta t \quad \text{(Equation 11)}$$

with the accumulated phase producing the phase trajectory φ(t) for the proton. This process was repeated across four independent nanoparticle setups with 2000 protons simulated for each setup. The decay signal corresponding to the dephasing among the protons is then calculated for each setup, and the final R^*_2 value is the average among the four setups [75]. In calculating the net magnetic field due to nearby nanoparticles, only particles within distance (l) of the proton are considered.

3.4.2 Radius of gyration analysis of microscopy images is in Toolbox 2.2.1

3.5 RESULTS AND DISCUSSION

System of single nanoparticles: The predicted R2* for each of the aggregates described in Figure 1 are an average of relaxation rates obtained from three simulations. In plot 1a), R2* relaxation predicted for a linear system of nanoparticles are presented. Systems of 9nm nanoparticles in a linear configuration were studied as 1) single nanoparticles in a linear configuration, 2) compact aggregates of two nanoparticles arranged in a linear configuration and 3) compact aggregates of three nanoparticles arranged in a linear configuration. The rationale for this as follows: at sizes under 18.4nm the time to relax at a given distance is greater than the time to diffuse to a new environment. The maximum R2* generated by a system of 50 nanoparticles arranged in a linear configuration is $49s^{-1}$. The R2*max is lower than systems of aggregates previously described[65] and can be explained by $\tau_R < \tau_D$ as in the case of nanoparticles of size 9nm, resulting in incomplete dephasing of protons coming in contact with this system.

System of nanoparticles with two or three 9nm nanoparticles as a single unit. To obtain a system with $\tau_D < \tau_R$ and protons dephased in a single encounter, compact aggregates of two and three 9nm nanoparticles were substituted for a single nanoparticle and arranged in a linear configuration as described in Figure 1a. In a system of two or three nanoparticles arranged in this manner, we see a drastic change in R2* with R2*max of $73s^{-1}$ and $92s^{-1}$ As a consequence the number of particles needed to transition from MAR to SDR is 40 nanoparticles

for system of single nanoparticles, 30 nanoparticles for a systems of two nanoparticles and 10 nanoparticles for system of three nanoparticles. R2max is reached when particles are dephased greater that $\pi/2$ and while this does not result in any further decrease in signal, this merely overdephases the protons and places them in the static dephasing regime. The differences in the number of nanoparticles needed for transition between the 3 systems results from the overlapping of magnetic fields primarily due to the size and number of nanoparticles.

In plot 1b, R2* of 9nm nanoparticles in a circular configuration is described. Previous studies have indicated that the distance between two small particles must be greater than 8r for the particles to be described by R2* of a single particle [75] In the circular configuration nanoparticles are arranged such that the addition of nanoparticles to the system increases the diameter of the circle and therefore also increase the distance between nanoparticles. Hence, the effect observed as R2*max is the net effect of neighboring particles and particles of distance d_{circle} away. In this scenario, all particles within the range of r to d_{circle} (diameter of the circle) are likely to exert an effect on any particle in question. Also, in a circular configuration of single 9nm nanoparticles, the diameter of the nanoparticle can be in the range of 9 to 50nm. This means that until sufficient nanoparticles are added to increase the effective diameter to 18nm, the time for the proton to diffuse away is much lower than the time for complete relaxation. Therefore, any particle in the vicinity is only likely to be partially dephased. The

R2* of the system increases with addition of nanoparticles, most likely in the motion averaging regime. However, this particular system fails to reach static dephasing regime: the diameter of the circle increases, increasing the distance between particles. Two factors are at play here: the interactions between neighboring particles maintain R2* greater than that of a single nanoparticle at a distance >8r and at a distance <8r there is no interactions between particles, so R2* does not increase. In this scenario, protons travel to new magnetic environments more frequently than in single nanoparticle systems and are therefore unlikely to be fully dephased in a single encounter. The R2* max is $47^{-1}s^{-1}$. It was previously shown that the interaction between two nanoparticles is at a maximum when the magnetic moment of nanoparticles are perpendicular to each other. Once the nanoparticles are grouped into two, where the two particles are perpendicular to each other, we see an increase in R2* of 58% at R2*max. At this point, the magnetic field according to Equation 1 is outside the particle. The increase in frequency of encounters results in an increased R2* max. In a system of three nanoparticles in a circular configuration, the R2* max increased by 52 %. The reason for this is as follows: the size of the nanoparticle is 27nm. At this aggregate size, the time for a proton to diffuse away is less than the time for the particle to fully dephase the proton, considering the large magnetic field of the particle ascertained from Equation 1. This increases the frequency of encounters between protons and magnetic particles resulting in higher R2*. This phenomenon also leads to the abrupt change from motion averaged to static dephasing regime once the magnetic fields of the particles

overlap. Here, it is interesting to note that R2max is about 50% greater than initial R2*. In this line of thought, a system of 4 nanoparticles produced an R2* of 87s-1 at 50 nanoparticles. Constructing circular aggregates of of 5 nanoparticles or greater would eventually lead to a clustered configuration and hence was not considered in this study.

In plot 1c, R2* relaxation for linear aggregates, circular aggregates and random clusters are compared and plotted vs. number of particles in the aggregate. The shape of the graph agrees with findings of earlier studies and conforms with theoretical prediction of SDR and MAR. It shows, increases in R2* in the MAR region and continuous dephasing in the static dephasing regime. In addition, in the MAR region, the R2* depends on the size of the aggregates. At sizes just above the MAR, the discrete process yields high relaxation rates independent of particle size. Beyond this regime with increasing particle size, a steady high R2* rate is maintained until at large particle sizes continuous dephasing is observed in the static dephasing regime

The transitional phase between the MAR and SDR is called the visit limiting regime (VLR) by Brooks. The importance of this transitional regime (VLR) needs to be explored because the R2* of the circular configuration increased by approximately 21% while that of the clustered configuration rose by only 8%.

The visit limiting mechanism is characterized by the ability of the aggregate to fully dephase a proton in a single encounter, as described by Equation 3. The relaxation rate that corresponds to the frequency of complete dephasing is

sufficient to yield an R2* rate near the static limit - hence, refocusing does not occur and R2* is high. From Equation 10, it is evident that the aggregate size corresponding to the dephasing region is therefore a critical size governed by D and ω.

The crossover from visiting limited mechanism to static dephasing mechanism is described by reaching the optimal aggregate size where particles are able to completely dephase protons surrounding them. With respect to the characteristic distance between particle, the radius of the full dephasing zone grows as the square of the particle size. At a particle size of 9nm, the full dephasing zone is small and the protons in the full dephasing zone are near the particle being described. Hence, itis desirable to design aggregates at the border between MAR and SDR or in the visit limit mechanism. In this region, R2* is maximized for the particular geometrical configuration of the aggregates. This region was found at 7 nanoparticlesfor linear, 10 nanoparticles for cluster and 14 nanoparticles for circular configuration

We then applied the Monte-Carlo simulation to study the effect of combining systems with different configurations. As indicated in Figure 2, we explored three combinations of the three configurations of nanoparticles: linear and cluster, cluster and circular and linear and circular.

Monte Carlo simulation of 200nm constructs: A combination of linear and cluster is represented in Figure 2a. With an R2*max of 84s^{-1} we note that although this is a 3% decrease compared to linear and an 18% increase compared to cluster. The transition from MAR to SDR is abrupt at less than 10 nanoparticles. We can infer from this data, that a combination of linear and cluster does not increase frequency of encounter with protons and creates overlapping magnetic fields resulting in instant overdephasing of protons.

In aggregate 2, the clusters around the circle resulted in a 7% increase in relaxivity. The R2* max is 2% greater than R2* max for circular and 6% greater than R2* max for linear. We also observe that static dephasing regime is maintained without any increase in the motion averaged regime.

The next combination explored is the combination of circular and cluster. An aggregate was constructed with clusters in a circular configuration. We found a 3% increase compared to circular and 26% increase compared to the clustered configuration. We also observed that R2* grows with the number of aggregates to ~ 20 aggregates. It can be thus inferred that addition of clusters around nanoparticles in circles increases frequency of encounters between protons and the magnetic particle, extending the effective radius of the nanoparticle aggregate.

From these results, we go on to study the effects of a combination of a circular and a linear configuration with an overall diameter of 150nm. We observe that the relaxivity increase by 13% compared to the combination of cluster and

circular. Plot B describes the increase in R2* until about 30 aggregates. Hence, again we can infer that the frequency of encounters between protons and magnetic particles are increased. The combination of circular and linear chains means that this type of aggregates creates zones with complete dephasing without overdephasing.

3.6 CONCLUSION

This study demonstrates that the configuration of nanoparticle aggregates determines the maximum relaxation induced. The difference in geometric configurations between aggregates also creates distinct differences in the number of nanoparticles needed to transition from MAR to SDR. While noting that the number of protons and aggregate is able to dephase is directly proportional to its size, considerations in constructing aggregates should also include the increase in the frequency of encounters between protons and magnetic particles while avoiding overlapping of magnetic fields. Immobilizing iron oxide nanoparticles in static matrices such as polymers or inorganic matrices can ensure aggregation in specific geometrical configuration. It is important to bear in mind that R2*max will decrease in systems with a higher diffusion coefficient [65]. Also, if the iron oxide core is coated with a hydrophobic coating, it is likely to exclude protons from coming within a distance necessary to achieve complete dephase.

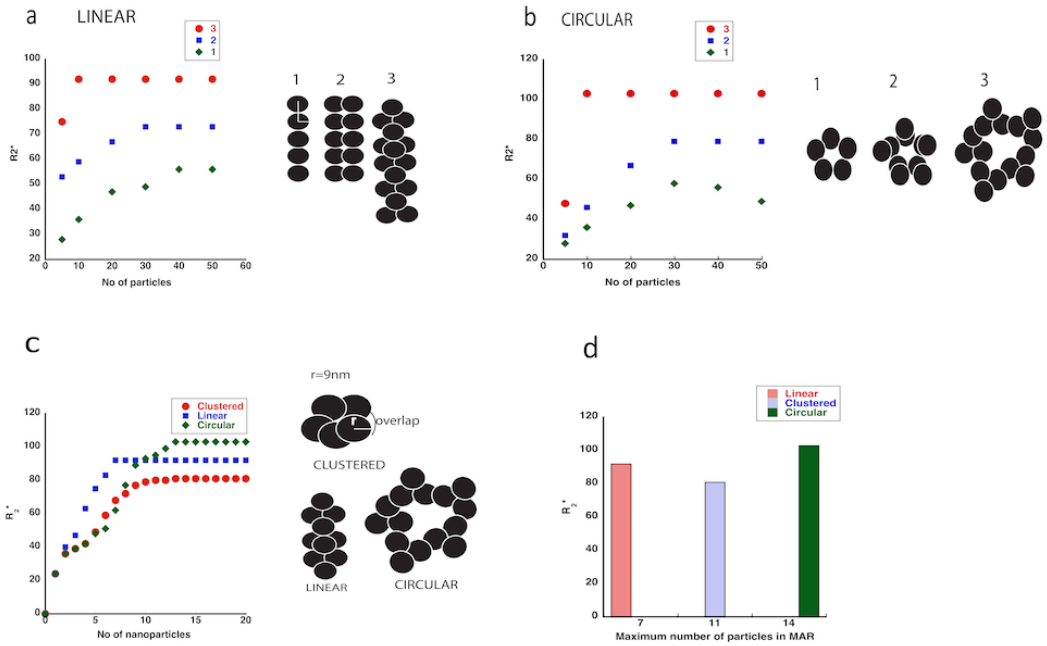

Figure 3.1: In this figure, Plot a describes the R2* of 9nm nanoparticles constructed in a linear configuration in sets of 1, sets of 2 and sets of 3. The linear configuration is described by particles whose centers are collinear to each other. In Plot b, we compare nanoparticles in a circular configuration arranged in sets of 1, sets of 2 and sets of 3. The angle between the centers of neighboring nanoparticles in the aggregate is 45^0. Plot c explores the transition from motion averaged regime to the static dephasing regime and R2* is presented as each set is added to the system. Plot d describes the maximum number of particle in each of the geometrical configurations describe to exit the MAR. The fractal dimensions for all structures were calculated separately using methods described previously.

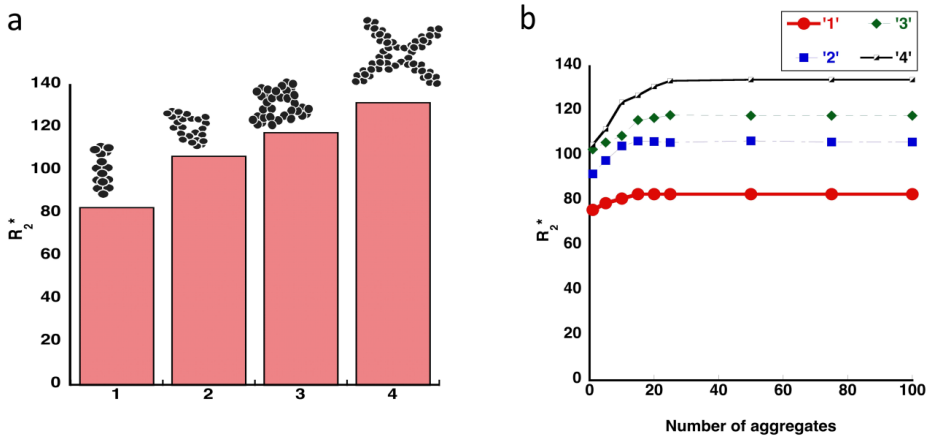

Figure 3.2: Plot a describes the simulated R2* of different aggregate constructed to experience a relaxation mechanism between MAR and SDR. Plot b describes the static limit or the transition from MAR to SDR in a system where the number aggregates in the system was increased.

REFERENCES

1. Kim, J.; Kim, H. S.; Lee, N.; Kim, T.; Kim, H.; Yu, T.; Song, I. C.; Moon, W. K.; Hyeon, T., Multifunctional uniform nanoparticles composed of a magnetite nanocrystal core and a mesoporous silica shell for magnetic resonance and fluorescence imaging and for drug delivery. Angewandte Chemie International Edition 2008, 47 (44), 8438-8441.

2. Gossuin, Y.; Roch, A.; Muller, R. N.; Gillis, P., An evaluation of the contributions of diffusion and exchange in relaxation enhancement by MRI contrast agents. Journal of Magnetic Resonance 2002, 158 (1-2), 36-42.

3. Roch, A.; Gossuin, Y.; Muller, R. N.; Gillis, P., Superparamagnetic colloid suspensions: water magnetic relaxation and clustering. Journal of Magnetism and Magnetic Materials 2005, 293 (1), 532-539.

4. Berret, J. F.; Schonbeck, N.; Gazeau, F.; El Kharrat, D.; Sandre, O.; Vacher, A.; Airiau, M., Controlled clustering of superparamagnetic nanoparticles using block copolymers: design of new contrast agents for magnetic resonance imaging. Journal of the American Chemical Society 2006, 128 (5), 1755-1761.

5. Chen, D. X.; Sun, N.; Huang, Z. J.; Cheng, C. M.; Xu, H.; Gu, H. C., Experimental study on T2 relaxation time of protons in water suspensions of iron-oxide nanoparticles: effects of polymer coating thickness and over-low 1/T2. Journal of Magnetism and Magnetic Materials 2010, 322 (5), 548-556.

6. Gossuin, Y.; Gillis, P.; Hocq, A.; Vuong, Q. L.; Roch, A., Magnetic resonance relaxation properties of superparamagnetic particles. Wiley Interdisciplinary Reviews: Nanomedicine and Nanobiotechnology 2009, 1 (3), 299-310.

7. Brooks, R. A.; Moiny, F.; Gillis, P., On T2 shortening by weakly magnetized particles: The chemical exchange model. Magnetic resonance in medicine 2001, 45 (6), 1014-1020.

8. Brooks, R. A., T2 shortening by strongly magnetized spheres: A chemical exchange model. Magnetic resonance in medicine 2002, 47 (2), 388-391.

9. Cho, K.; Wang, X.; Nie, S.; Shin, D. M., Therapeutic nanoparticles for drug delivery in cancer. Clinical Cancer Research 2008, 14 (5), 1310-1316.

10. Maeda, H.; Wu, J.; Sawa, T.; Matsumura, Y.; Hori, K., Tumor vascular permeability and the EPR effect in macromolecular therapeutics: a review. Journal of Controlled Release 2000, 65 (1-2), 271-284.

11. Lewinski, N.; Colvin, V.; Drezek, R., Cytotoxicity of nanoparticles. Small 2008, 4 (1), 26-49.

12. Duan, H.; Kuang, M.; Wang, X.; Wang, Y. A.; Mao, H.; Nie, S., Reexamining the effects of particle size and surface chemistry on the magnetic properties of iron oxide nanocrystals: new insights into spin disorder and proton relaxivity. The Journal of Physical Chemistry C 2008, 112 (22), 8127-8131;

13. Gillis, P.; Moiny, F.; Brooks, R. A., On T2 shortening by strongly magnetized spheres: A partial refocusing model. Magnetic resonance in medicine 2002, 47 (2), 257-263.

14. Binder, K., Monte‚ÄêCarlo Methods. Wiley Online Library: 1979.

15. Matsumoto, Y.; Jasanoff, A.,T2 relaxation induced by clusters of superparamagnetic nanoparticles: Monte Carlo simulations. Magnetic resonance imaging 2008, 26 (7), 994-998.

4 A MESOPOROUS MATRIX FOR TUNING R_2 AND R_2* PROPERTIES OF SUPERPARAMAGNETIC IRON OXIDE AGGREGATES

Chapter 4 A MESOPOROUS MATRIX FOR TUNING R_2 AND R_2* PROPERTIES OF SUPERPARAMAGNETIC IRON OXIDE AGGREGATES

4.1 Abstract

4.2 Introduction

4.3 Methods

4.4 Results and Discussion

4.5 Conclusion

4.1 ABSTRACT

The tuning of transverse relaxation rate R2 and R2* of 9nm iron oxide aggregates by confining them in a porous silicon matrix is reported in this study. The transverse relaxation rate of protons in the absence (R2*) or presence (R2) of a refocusing pulse is affected by the relative distance between a proton and a magnetic nanoparticle that causes dephasing of a proton. The relaxation rate can then be tuned when the self-diffusion coefficient of protons in the vicinity of iron oxide aggregates is adjusted to accommodate complete dephasing of a proton. This adjustment is achieved by confining iron oxide aggregates in porous silicon nanoparticles with 15nm (pSi15) and 23nm (pSi23) pore size to reduce the self-diffusion coefficient of protons. The self-diffusion coefficient of protons inside the

porous matrix is 0.33 relative to bulk water in pSi15 and 0.35 relative to bulk water in pSi23 as measured by nuclear magnetic resonance spectroscopy. The lower self-diffusion coefficient of protons minimizes the relative distance between a proton and magnetic nanoparticles in the relaxation time to enable complete dephasing of protons by nanoparticle cluster in the size range of 9nm to 27nm. Magnetic resonance relaxivity measurements indicate a dramatic increase of 70.1% increase in R2* by pSi15 and 64.4% in R2* by pSi23 and 68.5% increase in R2 by pSi15 and 71.3% in R2 by pSi23 over nanoparticles that are not confined within a porous matrix. We demonstrate here that pSi15 increases R2* to a greater extent than pSi23 by 12.9% and pSi23 increases R2 to a greater extent that pSi15 by 6.4%. The difference in R2 and R2* between the materials is caused by the number of nanoparticles needed for the aggregates to reach static limit. We conclude that the number of nanoparticles and aggregate configuration to reach static limit is different with (R2) or without (R2*) the presence of a refocusing pulse.

4.2 INTRODUCTION

Superparamagnetic iron oxides nanoparticles (SPIO) are currently used as the preferred contrast agent in magnetic resonance imaging. They were introduced shortly after the use of gadolinium chelates and now appear to be the preferred material for contrast enhancement in magnetic resonance imaging [65] . The popularity of SPIO particle labeling is due to the following desirable properties: Firstly, they provide the most change in signal per unit of metal particularly on

T2* weighted images as they are composed of thousands of iron atoms and defeat the inherent low contrast agent sensitivity of MRI [43]. Iron oxides are biodegradable and biocompatible and can be reused and recycled by cells using normal biochemical pathways for iron metabolism [43]. The high anatomical spatial resolution of MRI allowing the potential for quantification coupled with the low cytotoxicity of SPIO monitoring biological processes with MRI make this material a promising tool. Superparamagnetic nanoparticles are mostly used because of their negative enhancement effect on T2 and T2* weighted sequences [66]. Generally, the efficacy of a SPIO nanoparticle can be determined through accurate characterization of information such as size of the iron oxide crystals, the charge, the nature of the coating and the hydrodynamic size of the coated nanoparticle [76].

In a magnetic resonance imaging measurement, the T2 relaxation signal results from the dephasing of proton spins in the sample [73]. Following the application of a radio frequency pulse at 90 to the direction of the field of the magnet Boz , the protons precess in phase at the larmor frequency:

$$\omega = \gamma B_0$$ (Equation 1)

Here is the gyromagnetic ratio for a particular atom (2.67 x 10/s/T for water protons). In the absence of magnetic particles, the protons will gradually go out of phase due to proton-proton interactions and inhomogeneity in the field of the magnet [64]. Both of these processes are relatively slow and yield a low characteristics dephasing rate R2*. A higher dephasing rate is desirable in most

circumstances [77]. The relaxation rate can be greatly enhanced by introducing magnetic particles into the sample.

A number of theoretical and experimental studies devoted to examining the effect that iron oxide nanoparticles have on the transverse relaxation rate (R_2) of water protons have demonstrated that the size of the SPIONs are key factors influencing the relaxation rate [72a]. The effect of particle size has been more difficult to assess due to difficulties in determining accurate sizes and size distributions. However, aggregates of SPIONs have been shown to have dramatically higher relaxation rates compared to single SPIONs. Strategies for preparing SPION-based contrast agents by control aggregation have yielded colloids suitable for MRI with diameters of a few tens of nanometers, a high concentration of SPIONs (i.e., high magnetization), and superparamagnetic properties [78].

The influence of the particle coating on relaxivity remains unclear as various studies report different effects [9]. One study on poly ethylene glycol coating on SPIONS found that the relaxation rate decreased with increasing PEG length, while their simulations predicted that the coating causes competing effects that can either increase or decrease relaxivities [76]. Other recent studies reported that relaxivity values are nearly independent of polymer coatings for large magnetic particles (100 nm), while the relaxation rates of smaller particles (10 nm) were dramatically reduced when coated with silica. Another report showed that increasing the hydrophilicity of the particle coating leads to enhanced interactions

between the protons with the magnetic core thereby increasing the relaxivity [79]. Recently, Monte Carlo simulations illustrated that some of these discrepancies in effects are attributed to differences in particle size (or dephasing mechanism) and coating composition [80].

Magnetic nanoparticles obtained with different chemical processes display huge differences in terms of magnetic properties and saturation magnetization. These differences are attributed to changes in crystallographic order, surface structure and impurities [66]. The coating may also affect the magnetization due to the quenching of surface effects. The colloids of magnetic iron oxide composed of crystals measuring 4 to 6nm, placed in an external magnetic field, align and create very high local magnetic field gradients inducing water proton spin dephasing and consequently reducing the T2 relaxation times of the surrounding water [67].

The efficiency by which a contrast agent can accelerate the proton relaxation rate in a homogeneous medium is called relaxivity of the agent and defined by [43]:

$$R_2 = R^0 + RC \quad \text{(Equation 2)}$$

where R2 is respective T2 proton relaxation rate in the presence of the contrast agent, R^0 is the relaxation rates in the absence of contrast agent and C is the contrast agent concentration. [43]. However, it is the significant capacity of SPIO nanoparticles to increase the so-called T2* effect that is used in MR imaging [64].

In this study, we examine the effect of aggregating 9nm iron oxide nanoparticles in pores of porous silicon of average size 15nm and 23nm on R2 and R2*. We start by simulating (i) the effect of coating on the iron oxide on R2/R2* (ii) the effect of diffusion coefficient of water on R2 and R2* (iii) effect of increasing the number of particles in an aggregate on R2 and R2*.

The results obtained by simulation were then tested experimentally. Iron oxide nanoparticles were loaded into porous silicon nanoparticles of size 15nm and 21nm. Magnetic resonance measurements were performed to compare the R2 and R2* of both constructs. Finally, to understand the implications of these materials for invivo imaging, we simulated the effect on R2 and R2* as the number of aggregates for both nanocomposite systems are systematically increased.

4.3 METHOD

4.3.1 Preparation of porous silicon iron oxide nanocomposites:

The porous silicon was generated using an electrochemical etch in ethanolic HF of a silicon chip with a current density of 400 or 200 mA cm^{-2} to yield pore sizes between 8-17nm and 18-31nm followed by ultrasonication of the lifted off porous silicon film. The products were filtered using a 0.22 mm membrane yielding irregularly shaped nanoparticles with ~ 180 – 220 nm dimensions. The pore size was analyzed using SEM to determine that the pores were 16 nm. The Si-H

terminated Si particles were then loaded with oleic acid coated 9 nm Fe_3O_4 NPs to form the Fe_3O_4:pSi nanocomposites.

4.3.2 Simulation of coated iron oxide nanoparticles

A system of particles is created by placing 1000 particles at random within a volume described by the volume fraction. A proton is then placed at random within this system. The trajectory of the proton is evolved in time steps of t =1ns with the proton moving a distance in a random direction at each step. Periodic boundary conditions are used to keep the proton in the central cell and reduce artifacts at the edges of the system. At each step, the net magnetic field at the location of the proton due to nearby particles is calculated from

$$B = \frac{\mu M}{3}\left(\frac{R}{r}\right)^3\left(3\cos^2(\theta)-1\right) \text{ (Equation 3)}$$

$$\mu_N = \gamma_N \frac{h}{2\pi} I \text{ (Equation 4)}$$

Where is the permeability of free space, M is the magnetization of the particle, r is the distance from the particle center and θ is the angle with respect to the z direction and the radius of the particle is R.

The phase change ϕ per time step is approximated by:

$$\Delta\phi = \omega\Delta t = \gamma B \Delta t \text{ (Equation 5)}$$

Finally, the decay signal corresponding to the loss of phase coherence is calculated by

$$S(t) = \frac{1}{N_p}\sum_{i}^{N_p}\cos\left(\phi_i(t)\right) \quad \text{(Equation 6)}$$

Where N_p is the number of protons.

A CPMG pulse sequence is simulated by inverting the previously accumulated phase φi → −φi at each pulse (t = τCP, 3τCP, 5τCP…). The ensemble average x-component of the moments is calculated at each spin-echo (t = 0, 2τCP, 4τCP, …) as the average cosine of the phases. The decay is fit to $42.58\ \mathrm{MHz \cdot Tesla^{-1}}$ to extract the T2 for the simulated CPMG pulse sequence. A gradient echo pulse sequence is simulated as φi → +φi at each pulse. The relaxation rate is given by fitting this decay with an exponential function. For each of these setups, the trajectories of 1000 protons are generated. The final data point represents the average of the relaxation rates determined for each setup and the error bars are generated from the standard deviation between the relaxation rates.

To describe the motion of water within the porous silicon, a separate diffusion coefficient is defined by Dp as opposed to D_0 corresponding to the bulk. A boundary is implemented between the inside of the porous silicon with D_{psi} and the bulk region with D_0. In the simulations, the proton moves the same distance l at each time step. A proton inside the pore of porous silicon, where the diffusion coefficient is lower moves a smaller distance. We do not assume that water

accumulates inside the pores. We account for movement of protons into and out the pores. So, we assume that flux of protons into the pores is similar to the flux of proton outside the pores. A significant accumulation of protons in the pores yields unphysical densities, the R2* values would be artificially inflated.

The effect of porous silicon holds protons in a high field region for a longer period of time. As already shown at d = 9nm, this can have the beneficial effect of greatly increasing the R2* rate. However, this dephasing of protons in the pores for a longer period comes at the cost of a lower exchange between these protons and those in the bulk. As we show, the balance between these factors can yield either an enhancement or a reduction in R2 and R2* depending on the particle size and the ratio of diffusion coefficient.

4.3.3 MRI Imaging

We performed both spin echo and gradient echo imaging on a GE 3T scanner. To quantify transverse relaxation, we acquired 8 images with increasing TE, starting with TE=25 and in increasing of 10 ms depending on the T2. The repetition time TR was 1s, slice thickness was 5mm. Images of 128x64 matrix, 3.1mm x 3.1mm in plane resolution were acquired. For gradient recalled echo imaging, the TE was varied in steps of 15ms. Other imaging parameters were the same as for the spin echoes.

4.2.3 Fractal dimension analysis of microscopy images is in Toolbox 2.2.1

4.3.4 Diffusion coefficient measurement with NMR.

The Hahn spin-echo sequence (Toolbox 2.3.1) was used to obtain the self-diffusion coefficient of the sample. The $\pi/2$ pulse width was 9.6 μs. The sequence time interval was 15 s. If the spin-spin relaxation time T_2 of the sample turns out to be short, this sequence is not suitable because the NMR signal would completely decay during the spin-echo time. Assuming T2 of water into porous silicon to be around 500ms is long enough for measurement by the Hahn sequence. The echo signal obtained from the PFG sequence is related to the diffusion coefficient D according to the following equation:

$$A = A_0 \exp(-\gamma^2 g^2 \delta^2 D(\Delta - \frac{\delta}{3})) \quad \text{(Equation 7)}$$

where A is the area of the echo signal, A_0 is the area of that without gradient pulses, γ is the gyromagnetic ratio, g is the amplitude of a gradient pulse of duration δ, and Δ is the time interval between the two gradient pulses. Therefore, the diffusion coefficient can be obtained from the slope of a plot of the logarithm of the signal area $\ln(A/A_0)$ as a function of $\gamma^2 g^2 \delta^2(\Delta - \delta/3)$. Time intervals Δ of 50, 100, and 150 ms were used to evaluate the effects of Δ on the measured diffusion coefficients. After this initial evaluation, Δ was set at 50 ms, and the gradient width δ was varied from 0.1 to 2.0 ms. The coefficients D were extrapolated to infinite dilution, C = 0, to obtain the diffusion coefficient D_0

4.4 RESULTS AND DISCUSSION

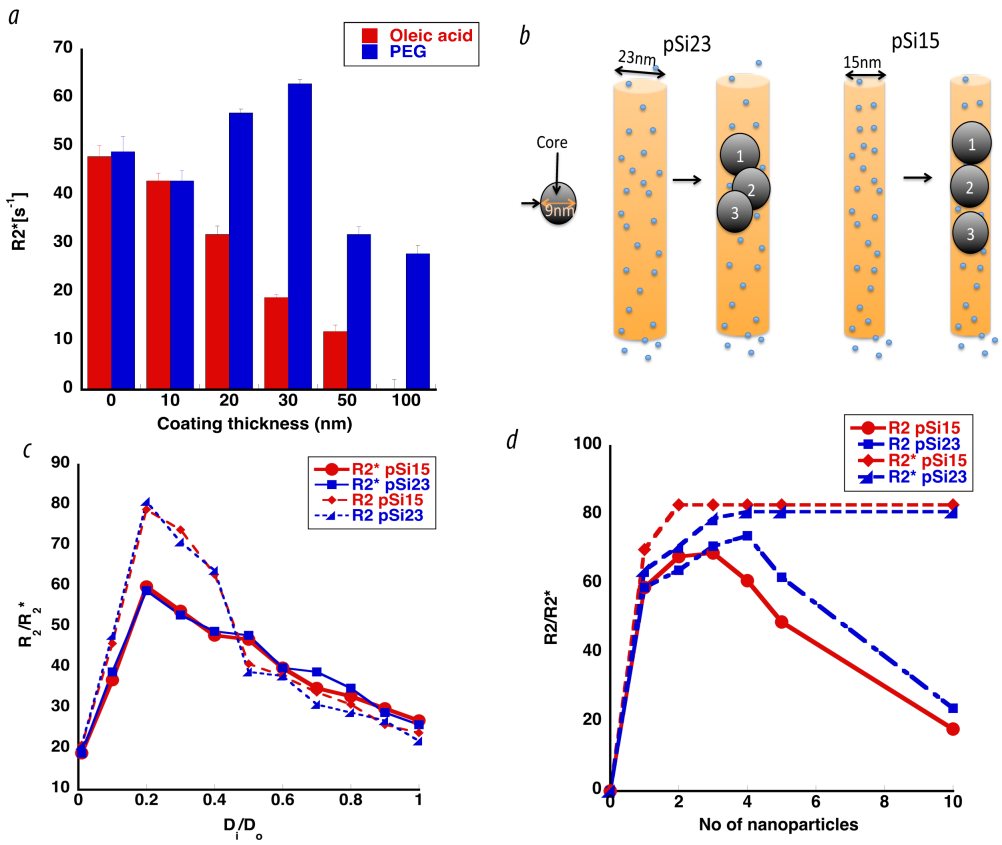

Figure 4.1: a) This plot describes the percentage drop in R2* once the thickness of coating (oleic acid and polyethylene glycol) of iron oxide nanoparticles is increased as observed via simulation with particle of radius 9nm.Oleic acid was assumed to be impermeable and polyethylene glycol has a D_i/D_0 of 0.1 where D_0 of $2.5x10^{-9}m^2/s$ b) This figure describes the modeling process of protons in a porous silicon cylindrical matrix. The pore size of the materials are 15nm and 23 nm on average according nuclear magnetic resonance spectrosocopy. c) R2* and R2 values of a cluster of nanoparticles were simulated at different diffusion coefficient. For this simulation, M = 2.58 x 10^5 T/m^3 and f = 3.14 x 10^{-6}. The simulations show a diffusion coefficient of 0.2 as the optimal diffusion coefficient. The simulations were done with r =9nm and a D_0 of $2.5x10^{-9}m^2/s$. d) This plot describes the simulation results for R2 and R2* in a scenario where nanoparticles were systematically added to a system. The fractal dimension for pSi23 was calculated to be 2.2 and pSi15 to be 1.6 for sets of 2-3 nanoparticles. A fractal dimension of 1.6 suggests collinear chains with overall moderate compaction, as per analysis of microscopy images.

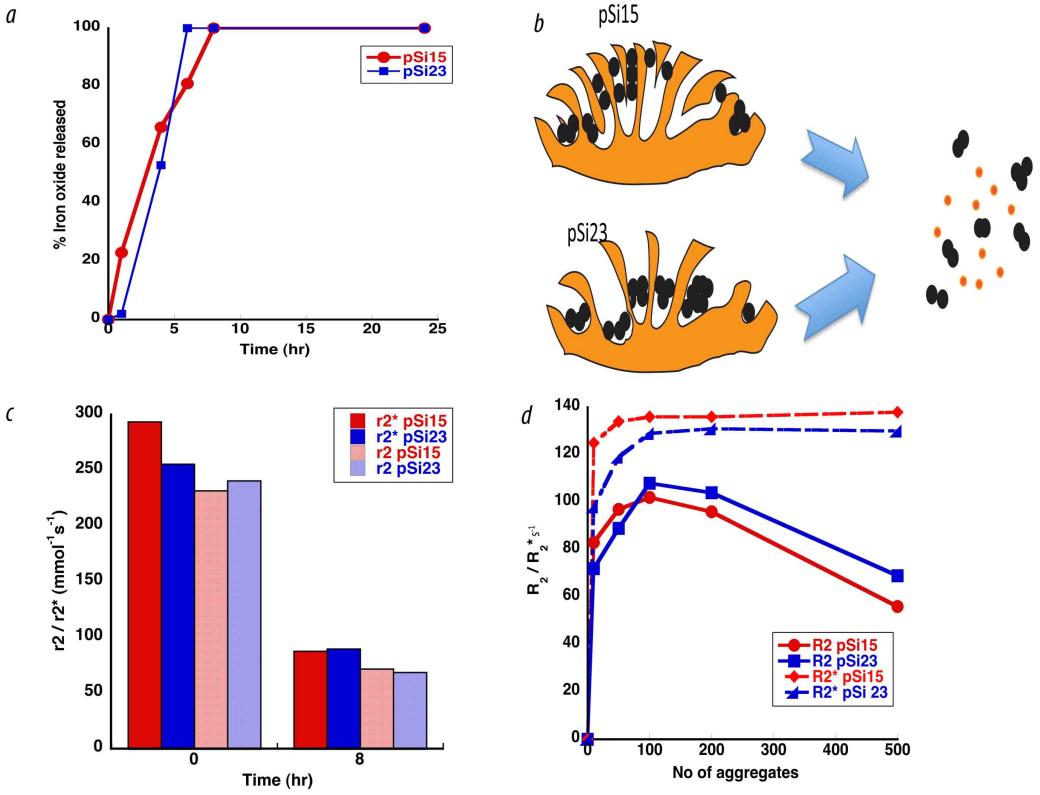

Figure 4.2: a) This plot describes the % iron oxide released from porous silicon iron oxide nanocomposites at room temperature with different pore sizes as measured by ICP-OES. This evidence accounts for the complete degradation of both materials in a time frame of 8 hours b) The schematic describes the release of iron oxide following the degradation of the porous silicon matrix. c) This plot describes the MR relaxation measurements performed at 0hr and 8hr after degradation at 3T d) The increase in number of aggregates was simulated by increasing the volume fraction as a proportion to the number of aggregates. The initial volume fraction is assumed to be f = 3.14 x 10^{-6}.

4.4.1 Proton diffusion inside the porous matrix:

The two factors that could affect spin dephasing around an iron oxide nanoparticle would be the nature of coating around the iron oxide nanoparticle and the self diffusion coefficient of protons. In this study, we analyze the details of spin dephasing mechanisms in the presence of a pegylated and oleic acid coating. Most iron oxide nanoparticle synthesis methods utilize a capping agent (such as oleic acid) or a stabilizing agents during or after synthesis. Capping agents exclude protons from reaching the core of the magnetic particles. Then, we look into the spin dephasing when iron oxide nanoparticles are surrounded by protons with a self-diffusion coefficient less than that in bulk water.

Polyethylene glycol coating: Polyethylene glycol (PEG) is traditionally used to stabilize iron oxide nanoparticle in aqueous solution. At sizes below 100,000 Da, PEG polymers are considered amphiphilic. This means they are soluble in water and organic solvents (acetone and chloroform). This allows PEG assembly at the SPION surface using a variety of chemistries that require use of either aqueous or organic solvents. In a recent study, Kohler et al grafted PEG to SPIONs via a silane group in the organic solvent, toluene. Hence, due to the relevance of pegylated SPIO nanoparticles, the ultimate effect of PEG on R2* was simulated in Figure 1a. The diffusion coefficient of polyethylene glycol used in the simulation was measured to be Di/Do = 0.1 according to NMR spectroscopy.

The effect of polyethylene glycol has three distinct impacts on relaxation rate depending on the size of the coating. In Figure 1a, we observe that an initial coating of polyethylene glycol increases the relaxation rate. This can be explained by the PEG holding protons in a high field region, maximizing dephasing. When this size increases to 20nm, the relaxation rate drops to a value lower than that of no coating. This can be explained by trapped protons now overdephasing and diffusion rate of protons into and out of the coating is fairly low. Hence, the number and frequency of protons being dephased are low and relaxation rate drops. Upon increasing the thickness of the coating, the relaxation rate (R2*) increases to 100nm. The enhancement increases as the particles now become more effective at holding a large number of protons within a high field region resulting in an increasing the number of protons that undergo full dephasing. The size of PEG in this experiment was calculated to be 3.26 nm (according to the Kuga relation) [81]. Hence, we expect a slight enhancement in relaxation rate (R2*).

Oleic acid coating: Then, we investigated the effect of an oleic acid coating. An impermeable coating such as oleic acid restricts access to the core and excludes a section of the magnetic field from protons. The thicker the coating, the greater the reduction in rate. The coating here restricts access to the high field region preventing protons from being dephased in a single encounter. From previous studies, we assume the oleic acid coating on iron oxide to be less than 2nm [82].

R2 vs lowering self diffusion coefficient of water: In the next step, we investigate the effect of placing iron oxide in a system of protons with low diffusion coefficient. To elucidate the role of lowering self-diffusion coefficient by confining small nanoparticles in a porous matrix, we study the R2 and R2* behavior of iron oxide nanoparticles in a porous silicon matrix through simulation and experimentation.

Porous silicon is a material obtained by anodic oxidation of monocrystalline silicon in concentrated hydrofluoric acid solutions. The properties of the material are very dependent on the type and resistivity of the original silicon substrate and on the electrochemical parameters used during the anodization processes. Porous silicon is often characterized by its pore size and porosity. In the case of heavily doped P-samples, the porosity and pore sizes increase with an increase in forming current density or a decrease in hydrofluoric acid concentration. a proper choice of the acid concentration and forming current density a layer of a given porosity can be obtained . Models to explain the formation mechanism of porous silicon, which at present remains unknown, should take into account this quantitative evolution of pore size and porosities. The pore size and porosity is likely to affect the diffusion and adsorption of water molecules [24].

Next, using NMR, we measured an effective diffusion coefficient of water, D_{H2O} (population average of free, intermediate and bound water), in porous silicon containing no superparamagnetic iron oxides. Figure 1b describes the nature of interaction between porous silicon matrix and iron oxide nanoparticles. The data shows that D_{H2O} from a bulk water value of 2.5×10^{-9} m^2/s drops to to 0.83 ×

10^{-9} and 0.89×10^{-9} m^2/s in the presence of porous silicon of pore size 23nm and 15nm respectively. A 78% porosity measured by gravimetric methods means the possibility of interpore connectivity and opening to the external surface.

To fully understand the effect of diffusion coefficients on relaxation times, dephasing mechanisms of protons need to be considered. Two main dephasing mechanisms have been defined and classified on the basis of particle size at constant volume fraction of particles. For small particles, protons dephase according to the motional averaging regime (MAR). In this regime, the distance traveled by a proton by diffusion is much larger than the average distance between particles and as a result, protons readily diffuse to a different magnetic environment before becoming fully dephased. As protons are not fully dephased in a single encounter with a particle, refocusing will occur when protons diffuse to a magnetic environment of opposite polarity, thereby retarding the overall relaxation rate [63]. At large particle sizes, the distance between particles is much larger than the distance traveled by the proton due to diffusion. Each proton thus experiences an almost constant magnetic environment and dephasing occurs as an approximately continuous process. As the protons are effectively fixed in place, this regime is named the static dephasing regime (SDR) [64].

Relaxation rates in MAR, therefore, decrease with decreasing particle sizes due to the greater frequency of diffusion-induced refocusing of protons at smaller sizes than at larger particle sizes. Above a critical particle size, the protons spend a sufficient amount of time near one particle to be fully dephased in a single

encounter with a particle. However, the proton must diffuse to within a relatively small distance of a particle to experience this full dephasing event. Brookes described the transition from MAR to SDR as visit limited regime. In this regime, the nanoparticles are completely dephased by the magnetic field without being over dephased. We suspect that lowering the diffusion coefficient places protons that would normally experience MAR in the visit-limited regime[63]. The visit limiting mechanism is the transition between motion averaged regime and static dephasing regime. In this regime, protons are dephased fully before reaching a new magnetic environment.

Also, the average distance traveled by a proton in the relaxation time τ_{SL} is given by

$$R_D = \sqrt{6D\tau_{SL}} \quad \text{(Equation 8)}$$

where D is the diffusion coefficient (D = 2.5 × 10^{-9} m^2/s as for bulk water).R_D is independent of the particle size and thus is the same at any particle radius R.

The characteristic interparticle distance can be defined by:

$$l = \left(\frac{\frac{4}{3}\pi}{f} \right)^{\frac{1}{3}} \quad \text{(Equation 9)}$$

If the separation between particles scales as l ~ R, then $R_D/l \sim 1/R$ demonstrating that the relative distance travelled by diffusion decreases with increasing particle size.

The distance at which relaxation time equals diffusion time can be described by the below equation:

$$R = \frac{\mu\gamma M}{3.75\pi D} r^3 \quad \text{(Equation 10)}$$

Placing a proton at a distance less than R would result in the proton being fully dephased before diffusing to a new environment while if placed at a distanced greater than R, the proton will diffuse to a new environment before being completely dephased. Simulations describing a drop in R2* in the presence of coating will guide in interpreting discrepancies between simulations and experimental values when studying nanoparticles under lower diffusion coefficients.

For Figure 1c, The results for the R2 and *R*2* values measured for a systems of particles with size of 9 nm are shown. As Di/D_o decreases from a value of 0.1, *R*2* increases. This enhancement reflects the effect when protons are held in a high field region. This increase continues until about Di/D_o = 0.2. After this point, *R*2* decreases with decreasing Di/D_o. At this point, protons in the diffusion layer have a low probability of diffusion, so it acts as an exclusion layer.

In Fig 1d, R2 and R2* were simulated as the number of particles (describing the configuration in Fig 1b) are systematically increased. The R2 values reach a maximum and then plateau, while R2* values remain at this high value. In the case of R2, for a refocusing pulse, a second RF is applied at 180° to the original pulse at a time τCP after the initial time. Being antiparallel to the initial pulse, the refocusing pulse inverts the phases of the protons and subsequent dephasing will then refocus the protons back toward being in phase. Hence while there is a rapid decay between $t = 0$ and $t = \tau CP$, the signal after τCP increases and culminates in a peak or "echo" of the original signal at $TE = 2\tau CP$. Fitting the decay over these peaks yields a decay much slower than the decay between peaks and the resulting R_2 is significantly lower than the static limit or the value for R2*.

The details of proton spin dephasing mechanism as the number of particles are increased in R2 and R2* following the slow motion regime and the static dephasing regime [73]. In the presence of fewer nanoparticles, the dynamics correspond to motion averaged regime where diffusion is dominant and protons move from one magnetic environment to another without being fully dephased.

In Figure 1d, we observe that pSi15 is expected to have a lower R2 value than pSi23. This is because the strength of the echo for R2 depends on the degree of refocusing. When iron oxide is arranged in a configuration as described in Figure 2d for pSi15, the more the protons are localized to a consistent magnetic field, the more effective the refocusing and hence R2 of the nanoparticles are lower

than pSi23. Also, the configuration of iron oxide nanoparticles in pSi15 accounts for the protons experiencing a nearly consistent magnetic environment. Consequently, the protons in pSi15 reach a static limit or the limit where we can consider the protons as fixed in a place and the magnetic field felt by each proton is independent of time.

4.4.2. Enhancement of R2 and R2* with the porous silicon matrix

Figure 2a describes the degradation properties of porous silicon iron oxide nanocomposites. As shown in Figure 2a, both pSi15 and pSi23 releases iron oxide nanoparticles in 8 hours. The nanoparticles are broken to 9nm iron oxide nanoparticles and hence can be easily removed through renal clearance. In Figure 2b the porous silicon breaks down into orthosilicic acid.

Given their measured size, the particles under study in this work are predicted to dephase according to the MAR. The fractal dimensions of iron oxide nanoparticles in the nanocomposites were measured to be 1.6 and 2.3. Figure 2c describes a 70.1% increase in R2* by pSi15 and 64.4% in R2* by pSi23 and 68.5% increase in R2 by pSi15 and 71.3% in R2 by pSi23 over nanoparticles that are not confined within a porous matrix. We also observe here that pSi15 increases R2* to a greater extent than pSi23 by 12.9% and pSi23 increases R2 to a greater extent that pSi15 by 6.4%. The porous nature of porous silicon allows the free diffusion of protons while lowering the self-diffusion coefficient of water [24]. Therefore, the matrix slows down water molecules inside of it and holds them in regions near the particle for longer periods than for particles located

outside the matrix. The high porosity accounts for the reduced residence time and also implies a constant diffusion of water molecules between the inside and outside of the porous matrix. These effects affect the dephasing of protons differently depending on the dephasing mechanism. In MAR, protons are not fully dephased in a single encounter when D_0 equals the free self-diffusion coefficient of water. From Equation 3, it can be ascertained that D_0 is inversely proportional to R (the distance at which full dephasing occurs). Consequently, the relaxation rate at small particle sizes is greatly enhanced by lowering diffusion coefficient.

In Fig 2d, it is evident that increasing number of aggregates (volume fraction) in a system behaves in similar ways to increasing the size of a nanoparticle [73]. Under these circumstance, the simulation describes the reaching of a static limit for R2 and R2* when number of aggregates in the system is systematically increased. In the presence of fewer aggregates, the dynamics correspond to that of the MAR where diffusion is dominant. In this regime, protons are dephased in a slow and incremental manner. Hence, due to diffusion induced refocusing, the resulting R2* rate is low. In a cluster of particles, the possibility of full dephasing of a proton in a single encounter is possible. Here protons fully diphase in discrete events. The number and frequency of such dephasing events is sufficient to yield a large R2* rate.

4.5 CONCLUSION:

In this study, proton trajectories within a system of nanoparticles in a porous silicon system with different diffusion coefficient and fractal dimension was build,

tested and compared with experimental observation. For systems where number of particles or aggregates are increased, the observed R2 and R2* agree with previous predictions made for particles in MAR, SMR and SDR. The enhancement in R2* when iron oxide nanoparticles were confined within porous silicon has the following implication on the design of R2 and R2* agents : Diffusion coefficient of the host material can be used to compensate when nanoparticles of small size to achieve complete dephasing. Furthermore, the comparison between two materials where self-diffusion of water is lowered than bulk and the two materials host iron oxide with different geometric configurations has two implications in the design of contrast agents for magnetic resonance imaging using porous materials. Firstly, R_2 was higher when nanoparticles were hosted in a clustered configuration implying that these materials can be used for applications to selectively increase R2. Also, R2* was higher when nanoparticles are hosted in a near linear configuration, implying that these materials can be used in applications to selectively increase R2*. Secondly, the modest, but noticeable difference between R2 and R2* can be exploited by furthering materials research to construct aggregates of different fractal dimensions to create porous materials specific to R2 relaxation rate or R2* relaxation rate.

REFERENCES:

1. Berret, J. F.; Schonbeck, N.; Gazeau, F.; El Kharrat, D.; Sandre, O.; Vacher, A.; Airiau, M., Controlled clustering of superparamagnetic nanoparticles using block copolymers: design of new contrast agents for magnetic resonance imaging. *Journal of the American Chemical Society* **2006,** *128* (5), 1755-1761.
2. McRobbie, D. W., *MRI from picture to proton*. Cambridge Univ Pr: 2003.
3. Chen, D. X.; Sun, N.; Huang, Z. J.; Cheng, C. M.; Xu, H.; Gu, H. C., Experimental study on T2 relaxation time of protons in water suspensions of iron-oxide nanoparticles: effects of polymer coating thickness and over-low 1/T2. *Journal of Magnetism and Magnetic Materials* **2010,** *322* (5), 548-556.
4. Nath, S.; Kaittanis, C.; Ramachandran, V.; Dalal, N. S.; Perez, J. M., Synthesis, magnetic characterization, and sensing applications of novel dextran-coated iron oxide nanorods. *Chemistry of Materials* **2009,** *21* (8), 1761-1767.
5. Qiu, P.; Jensen, C.; Charity, N.; Towner, R.; Mao, C., Oil phase evaporation-induced self-assembly of hydrophobic nanoparticles into spherical clusters with controlled surface chemistry in an oil-in-water dispersion and comparison of behaviors of individual and clustered iron oxide nanoparticles. *Journal of the American Chemical Society* **2010**.

6. Gossuin, Y.; Roch, A.; Muller, R. N.; Gillis, P.; Lo Bue, F., Anomalous nuclear magnetic relaxation of aqueous solutions of ferritin: An unprecedented first order mechanism. *Magnetic Resonance in Medicine* **2002,** *48* (6), 959-964.

7. Roch, A.; Gossuin, Y.; Muller, R. N.; Gillis, P., Superparamagnetic colloid suspensions: water magnetic relaxation and clustering. *Journal of Magnetism and Magnetic Materials* **2005,** *293* (1), 532-539.

8. Muller, R.; Vander Elst, L.; Roch, A.; Peters, J.; Csajbok, E.; Gillis, P.; Gossuin, Y., Relaxation by metal-containing nanosystems. *Advances in Inorganic Chemistry* **2005,** *57*, 239-292.

9. Duan, H.; Kuang, M.; Wang, X.; Wang, Y. A.; Mao, H.; Nie, S., Reexamining the effects of particle size and surface chemistry on the magnetic properties of iron oxide nanocrystals: New insights into spin disorder and proton relaxivity. *The Journal of Physical Chemistry C* **2008,** *112* (22), 8127-8131.

10. Larsen, B.; Haag, M.; Serkova, N.; Shroyer, K.; Stoldt, C., Controlled aggregation of superparamagnetic iron oxide nanoparticles for the development of molecular magnetic resonance imaging probes. *Nanotechnology* **2008,** *19*, 265102.

11. Zou, P.; Yu, Y.; Wang, Y. A.; Zhong, Y.; Welton, A. R.; Galb n, C.; Wang, S.; Sun, D., Superparamagnetic iron oxide nanotheranostics for targeted cancer cell imaging and pH-dependent intracellular drug release. *Molecular pharmaceutics* **2010**.

12. Chen, D. X.; Sun, N.; Gu, H. C., Size analysis of carboxydextran coated superparamagnetic iron oxide particles used as contrast agents of magnetic resonance imaging. *Journal of Applied Physics* **2009,** *106* (6), 063906-063906-9.

13. Bowen, C. V.; Zhang, X.; Saab, G.; Gareau, P. J.; Rutt, B. K., Application of the static dephasing regime theory to superparamagnetic iron oxide loaded cells. *Magnetic Resonance in Medicine* **2002,** *48* (1), 52-61.

14. Gossuin, Y.; Gillis, P.; Hocq, A.; Vuong, Q. L.; Roch, A., Magnetic resonance relaxation properties of superparamagnetic particles. *Wiley Interdisciplinary Reviews: Nanomedicine and Nanobiotechnology* **2009,** *1* (3), 299-310.

15. Linke, H.; Mansson, A., *Controlled nanoscale motion*. Springer.

16. LaConte, L. E. W.; Nitin, N.; Zurkiya, O.; Caruntu, D.; O'Connor, C. J.; Hu, X.; Bao, G., Coating thickness of magnetic iron oxide nanoparticles affects R2 relaxivity. *Journal of Magnetic Resonance Imaging* **2007,** *26* (6), 1634-1641.

17. Anglin, E. J.; Cheng, L.; Freeman, W. R.; Sailor, M. J., Porous silicon in drug delivery devices and materials. *Advanced drug delivery reviews* **2008,** *60* (11), 1266-1277.

18. Gossuin, Y.; Roch, A.; Muller, R. N.; Gillis, P., An evaluation of the contributions of diffusion and exchange in relaxation enhancement by MRI contrast agents. *Journal of Magnetic Resonance* **2002,** *158* (1-2), 36-42

5 T2 TUNABLE BIODEGRADABLE NANOCOMPOSITES FOR QUANTIFYING DRUG RELEASE ON NUCLEAR MAGNETIC RESONANCE

Chapter 5 QUANTIFYING DRUG RELEASE FROM T_2 TUNABLE BIODEGRADABLE NANOCOMPOSITES WITH NUCLEAR MAGNETIC RESONANCE SPECTROSCOPY

5.1 Abstract

5.2 Introduction

5.3 Methods

5.4 Results and Discussion

5.5 Conclusion

5.1 ABSTRACT

Low molecular weight drugs have very low magnetic susceptibility on magnetic resonance imaging. Nanoparticle formulations with an imaging and a therapeutic agent could allow non invasive assessment of low molecular weight drugs releasing from nanoparticles *invivo*. Therefore, using magnetic nanoparticles could enhance the sensitivity of detecting the release of therapeutics from nanoparticles. In this study, we investigate the release of sorafenib tosylate from biodegradable porous silicon iron oxide nanocomposites. A consequence of degradation of the porous silicon matrix is the release of iron oxide nanoparticles. Quantification of iron oxide release, self-diffusion coefficient of protons during degradation of the matrix and transverse relaxation times during 0 to 8hours revealed a mechanism for tuning transverse relaxation during degradation of

porous silicon iron oxide nanocomposite. We observed a linear relationship between the change in transverse relaxation and percentage drug released from the porous matrix over time. We conclude that porous silicon iron oxide nanocomposites can be used to determine concentration of drug released from transverse relaxation measurements.

5.2 INTRODUCTION

Nanotheranostics and image guided drug delivery are important new tools for cancer treatment because they offer the opportunity of visualizing and monitoring of drug release and therefore offer potentially better therapeutic effect at lower doses of toxic drugs. As the vast majority of therapeutic agents used in nanomedicine formulations are inactive when conjugated to or entrapped in the carrier material, it is important to ensure that the agents are actually being released [11]. In vitro, this can generally be done relatively easily, e.g. using HPLC, but in vivo, confirming drug release can be challenging. After harvesting the target organ or tissue, the material needs to be homogenized and the cells need to be lysed to release the agents from certain intracellular compartments. During these processing steps, and especially during cell lysis using detergents such as Triton-X, many types of carrier materials are also destabilized. For example, in the case of liposomes, it is impossible to discriminate between the amount of active agent that was still present within the liposomes at the point of harvesting and homogenization, and the amount that was already released into the extra- and intracellular environment [12]. To overcome this shortcoming, and to enable

noninvasive analysis of (the kinetics of) drug release in vivo, nanotheranostics have been developed in which drugs and imaging agents are co-incorporated into the same delivery system.

The strategy of using radionuclides for this purpose does not allow the distinction between signals from the bound/entrapped and the unbound/free form, therefore these imaging agents are not suitable for visualizing drug release. Magnetic resonance (MR) contrast agents, such as gadolinium and manganese, depend on the interaction with surrounding water molecules to generate a signal. This interaction varies substantially when these agents are present within versus outside of water-impermeable vesicles, such as liposomes, making these MR probes highly suitable for monitoring drug release [12].

An example of this concept has been published by Dewhirst and colleagues, who used manganese sulfate ($MnSO_4$) both to load doxorubicin into liposomes (by means of a method comparable to ammonium sulfate/pH gradient loading) as well as to generate a significant increase in MR signal upon drug and contrast agent release [20, 83]. Both standard (non-thermosensitive; NTSL) and temperature-sensitive liposomes (TSL) were used in these studies, which included both in vitro and in vivo experiments. It was shown that the relaxivity (i.e. the potential for MR signal enhancement) of TSL at temperatures below the transition temperature (T_g) was comparable to that of NTSL, but that it substantially increased upon heating the TSL to temperatures exceeding the T_g (i.e., > 39.5°C), indicating release of Mn^{2+} from the liposomes [83]. These findings were confirmed

in two follow-up analyses, in which contrast agent release from TSL was correlated with doxorubicin release, and in which drug dose painting was performed on the basis of MRI [20].

An understanding of how transverse relaxations measurements are performed in magnetic resonance imaging can further opportunities into creating nanoparticles that possess the function of changing transverse relaxation in response to a certain events. A description of the contribution of iron oxide nanoparticles to transverse relaxation is given below.

In a nuclear magnetic resonance imaging measurement, the T_2 relaxation signal results from the dephasing of proton spins in the sample. Following the application of a radio frequency pulse at 90° to the direction of the field of the magnet $B_0\hat{z}$, the protons precess in phase at the Larmor frequency

$$\omega = \gamma B_0 \quad \text{(Equation 1)}$$

where γ is the gyromagnetic ratio for a particular atom (2.67×10^8 s^{-1} T^{-1} for water protons).

In the absence of magnetic particles, the protons will gradually go out of phase due to proton–proton interactions and inhomogeneties in the field of the magnet. Both of these processes are relatively slow and yield a low characteristic dephasing rate R_2 and long relaxation time T2*(where T2* = 1/R2*). While appropriate for some applications, a much higher R_2 is desirable in the case of

theraneutic applications. The relaxation rate can be greatly enhanced by introducing magnetic particles into the sample. Taking the particles as dipoles, the z component of the magnetic field generated by each particle is given by:

$$B = \frac{\mu_0 M}{3}\left(\frac{R}{r}\right)^3\left(3\cos^2(\theta)-1\right)$$ (Equation 2)

The inclusion of magnetic particles thus introduces a series of local inhomogeneties in the magnetic field. As the precessional frequency is proportional to the magnetic field, this causes protons to precess at different rates and thus yield a high R2* value.

More simply, if we consider [43] the protons all precessing in phase at the Larmor frequency as determined by the external magnetic field, the effect of the particles can be seen as local perturbations which continuously change the phase of individual protons. The evolution of the phase of a particular proton during a time Δt is then given by [63]

$$\Delta\phi = \omega\Delta t = \gamma B\Delta t$$ (Equation 3)

where we neglect proton-proton interaction and assume an ideal magnet (no inhomogeneties) such that B arises only from the net field due to the particles [64]. The phase of a proton in a strong positive field will rapidly increase while the phase of a proton in a strong negative field will rapidly decrease. The net effect is rapid dephasing among the protons near the particle and hence a fast decay

signal. By this mechanism, magnetic particles serve as a highly effective contrast agent by producing a large R2* value for protons in their vicinity [73].

In the small particle limit, the relative distance travelled by diffusion R_D is large compared to the interparticle spacing l(R_D/l > 1) indicating that the proton visits many particles in the relaxation time. If, subsequent to an encounter, the proton diffuses to a region of opposite polarity, the corresponding dephasing will partially refocus the proton. [67]:

$$R_2^* = \frac{16}{45} f \Delta\omega_0^2 \frac{R^2}{D} \quad \text{(Equation 4)}$$

f is the volume fraction, ω is the Larmor frequency, D is the self diffusion coefficient with water. This dephasing mechanism corresponds to the motion averaged regime.

Further, as R_D/l ≳ 1, the small amount of dephasing that does occur may be undone by diffusion to a different magnetic environment. However, also due to diffusion, the proton will eventually come in close range of a particle and at that point undergo rapid and full dephasing. The relaxation rate then corresponds to the frequency of these full dephasing events and this frequency is sufficient to yield an R2* value near the static limit. That is, since the protons are fully dephased in a single encounter, refocusing does not occur and R2* is high. This dephasing regime was named visit limiting mechanism by Brookes [56].

5.3 METHODS:

Porous silicon iron oxide nanocomposite (pSiNC) preparation and drug loading:

For preparation of porous silicon iron oxide nanocomposite 2mg/ml solution of oleic acid coated iron oxide nanoparticles in chloroform (Sigma) was added to dry 20mg porous silicon iron oxide nanoparticles. This solution was agitated for 6 hours on a mechanical shaker to allow iron oxide nanoparticles to infiltrate the pores of porous silicon. The solution was placed next to a magnet to separate the loaded particles and free iron oxides from the unloaded porous silicon nanoparticles. With the magnet in place, the unloaded porous silicon nanoparticles in solution were removed by aspirating with a pipette. 5ml of chloroform was added to the remaining particles and the solution was spun down to separate the mixture of loaded nanocomposites and free iron oxides from the solvent. To remove loosely bound iron oxides on the surface of the porous silicon iron oxide nanocomposite, 1ml of chloroform was added to the particles and sonicated for 10 seconds . The particles were allowed to settle and the supernatant was removed. The oleic acid coated iron oxide particles present higher solubility than the porous silicon iron oxide nanocomposites in chloroform. This process was repeated a few times to ensure complete removal of free iron oxides.

Oxidation of porous silicon iron oxide nanocomposites: Porous silicon iron oxide nanocomposites were oxidized under ambient condition at 200 degrees in a oven (Perkin Elmer Inc) for 5 hours to achieve a Si-OH layer for pegylation purposes.

Loading of Sorafenib tosylate into porous silicon iron oxide nanocomposite: A concentrated solution of sorafenib tosylate (Bioscientific, inc) was made by dissolving 15mg/ml in ethanol (Sigma Aldrich). This solution was added to porous silicon iron oxide nanocomposite particles and agitated for 4 hours to load the sorafenib tosylate drug into the porous silicon iron oxide nanocomposites. The particles were rinsed again in ethanol (Sigma), and dried at 80 degrees to remove ethanol trace left on the particles. The dried nanoparticles were resuspended in absolute ethanol and sonicated for 10 seconds, centrifugated followed by aspirating the supernatant to remove to remove drug molecules loosely bound to the surface of the nanocomposite . This process was repeated three times. The resulting drug loaded nanocomposite was dried in a vaccum oven (Perkin Elmer) at 80 degrees .

Pegylation of nanoparticles: The polyethylene glycol- silane porous silicon iron oxide nanocomposite (Laysan Inc) contains a highly reactive silanol group that can attach to the oxidized porous silicon nanocomposite surface by forming a siloxane bond. The pegylation was achieved by placing the dry drug loaded nanoparticles in a 10mM solution of methoxy-PEG-silane in chloroform. The pegylation process renders the nanocomposite particles stable in serum.

Dynamic Light Scattering (Zetasizer ,Malvern. Inc) was used to confirm that the size of the pegylated drug loaded nanoparticles is still in the nano range. The zeta potential was measured to confirm that the nanoparticles had a neutral surface charge.

Release of sorafenib tosylate from porous silicon iron oxide nanocomposite:

The drug release study was performed in PBS buffer at 37 degrees by dialysis using Slide-A-Lyzer MINI dialysis microtube with a molecular weight cut- off of 10,000K (Pierce, Rockford, IL). To measure the drug release profile of sorafenib tosylate in Phosphate Buffered Solutions drug loaded pSi and pSiNC solutions were split equally into dialysis microtubes (1ml into each tube). Each microtube was placed on a float and then collectively placed in beaker with 1L solution of phosphate buffered saline at 37^0 C. The glass tubes were placed in a large beaker filled with water supported by a Styrofoam holder on a hotplate with gentle stirring to ensure tubes remain at 37 degrees for 24 hours. At each time point 0. 1, 4,6, 8 and 24 hours 3 glass tubes were collected separately and mixed with 100ul of Internal standard (erlotinib tosylate at 25mg/l). 3ml of ethyl acetate was added to the solution to extract the sorafenib tosylate and the internal standard. The tubes were agitated for 10 minutes with a mechanical shaker, transferred to centrifuge tubes and centrifuged for 5min at 4000rpm. The supernatant containing the released drug was transferred in a glass tube and

evaporated to dryness under a fume hood overnight. The residue was dissolved in 120ul of acetonitrile.

Invitro degradation of pSi and porous silicon iron oxide nanocomposite:

A series of samples containing 0.05mg/ml of porous silicon iron oxide nanocomposite particles and porous silicon only nanoparticles in 1ml of PBS solution were incubated at 37degrees. An aliquot of 0.5ml of solution was removed a different time points and filtered with a centrifugal filter (30,000 Da molecular weight cut-off, Millipore, inc.) to remove undegraded porous silicon iron oxide nanocomposites. 0.4ml of filtered solution was diluted in 4.6ml of nitric acid (2%(v/v)) and subjected to analysis by inductively coupled plasma optical emission spectroscopy (ICP-OES, Perkin Elmer Optima 3000DV). The total silicon and iron content in the solution was determined by diluting 0.5ml into 4.5ml nitric acid and measuring silicon content via Inductively Coupled plasma optical emission spectroscopy (ICP-OES) (Figure 1).

Measuring T2 and diffusion coefficient with Nuclear Magnetic Resonance Spectroscopy: The T_2 transverse relaxation behavior of water in the tablets was determined using the Carr–Purcell–Meiboom–Gill (CPMG) pulse sequence [90x–(τ–180y–τ). The n values used were 2 and 16, equivalent to time sequences of 40 and 320 ms. The results were fitted to the equation $I = I_0 \exp(-t/T_2)$. The two-point experiment yielded results consistent with the analysis of a 32-point experiment which showed the same T_2 value to within a few percent.

The T_2 relaxation experiments were performed on a Bruker DRX 400 spectrometer. All relaxation measurements were conducted at 25°C.

The Hahn spin-echo sequence (Toolbox 2.3.1) was used to obtain the self-diffusion coefficient of the sample. The $\pi/2$ pulse width was 9.6 μs. The sequence time interval was 15 s. If the spin-spin relaxation time T_2 of the sample turns out to be short, this sequence is not suitable because the NMR signal would completely decay during the spin-echo time. Assuming T2 of water into porous silicon to be around 500ms is long enough for measurement by the Hahn sequence. The echo signal obtained from the PFG sequence is related to the diffusion coefficient D according to the following equation:

$$A = A_0 \exp(-\gamma^2 g^2 \delta^2 D(\Delta - \frac{\delta}{3})) \quad \text{(Equation 5)}$$

where A is the area of the echo signal, A_0 is the area of that without gradient pulses, γ is the gyromagnetic ratio, g is the amplitude of a gradient pulse of duration δ, and Δ is the time interval between the two gradient pulses. Therefore, the diffusion coefficient can be obtained from the slope of a plot of the logarithm of the signal area $\ln(A/A_0)$ as a function of $\gamma^2 g^2 \delta^2(\Delta - \delta/3)$. Time intervals Δ of 50, 100, and 150 ms were used to evaluate the effects of Δ on the measured diffusion coefficients. After this initial evaluation, Δ was set at 50 ms, and the gradient width δ was varied from 0.1 to 2.0 ms. The coefficients D were extrapolated to infinite dilution, C = 0, to obtain the diffusion coefficient D_0

5.4 RESULTS AND DISCUSSION

(i) Degradation of porous silicon matrix:

One of the key roles of the porous silicon host nanomaterial is to provide a biodegradable and bioresorbable matrix for the components of the composite. The oxide of the silicon host undergoes hydrolysis when in physiological conditions (37^0C) resulting in the degradation of the pSiNC. Oxidized porous silicon degrades in aqueous solution to form a biological inert compound, orthosilicic acid ($Si(OH)_4$) as described in equation 1. Since the pKa-value of orthosilicic acid is as high as 9.5, the fraction of the deprotonated form in body fluids is so small that it is not likely to impede protein delivery or other biological processes susceptible to pH changes.

$Si + O_2 \rightarrow SiO_2$

$SiO_2 + H_2O \rightarrow Si(OH)_4$ (Equation 1)

Initial physical evidence of degradation of the oxidized porous silicon matrix in the experiments is the decrease in size of the nanocomposites over 8 hours under physiological conditions (Fig 5.1a). The pegylated surface, introduced to prevent aggregation and promote stability, could potentially be removed by the degradation process, however, zeta potential measurement of surface charge at time = 0,1,4,6 and 8 hours showed no significant change(Fig 5.1b). The percentage mass of the porous silicon matrix component of pSiNC degrading over time was investigated by degrading 0.05 mg/ml Si of pSiNC at

physiological conditions and analysis by ICP-OES. In addition we compared the nanocomposite to porous silicon nanoparticles of similar size and surface chemistry in physiological conditions (37 ^{0}C/PBS @ pH = 7.4). The samples were filtered to remove non-degraded pSiNC and the concentration of Fe and Si were quantified by ICP-OES (Figure 5.1c). No significant difference of the degradation rate was observed between the porous silicon particles (pSi) and the porous silicon iron oxide nanocomposite (pSiNC), i.e. the iron oxide has no influence on the degradation profiles of pSi nanoparticles and pSiNC.

Table 5.1 shows the hydrodynamic size of the porous silicon nanoparticles at different stages in the preparation of the nano-composite.

Preparation step	Hydrodynamic size [nm]	Polydispersity index	Zeta potential [mV]
Porous silicon nanoparticles (prior to iron oxide loading)	176	0.21	-24.7
After iron oxide loading	183	0.37	/
Pegylation and size exclusion	197	0.43	0.4
Loading of chemotherapeutic	203	0.36	/

Another important observation made upon analyzing the iron component of the undegraded portion of the nanocomposites is the steady decrease in the ratio of Fe_3O_4: pSi ratio in the 24 hour time frame corresponding with an increase in [Fe] concentration observed in the degraded portion of the pSiNC separated by size exclusion.

Previously, we have determined by BET isotherm measurements that sufficient free volume in the pSiNC (i.e. 33%) was available to load drugs. In the case of sorafenib tosylate, the drug loading process involved immersing the porous nanoparticles into a drug solution, forcing the drug to adhere to the pore walls and trapping the drug in the pores by evaporation of the solvent. (Salonen et al., 2005) The measurement of drug concentration loaded into a known concentration of pSi released was performed using high performance liquid chromatography (HPLC). The observed result was 89µg of drug +/- 21µg was loaded per mg of pSi.. The zeta potential measurements of pegylated sorafenib tosylate loaded pSiNC was -2.8mV with a standard deviation of 4.3mV, confirming that the surface charge of the nanoparticles does not change in the presence of sorafenib tosylate.

(ii) Release of sorafenib tosylate upon degradation of porous silicon iron oxide nanocomposites:

Sorafenib tosylate, a hydrophobic chemotherapeutic drug was loaded into the pSiNC with a final mass ratio of 89 µg +/- 21ug of drug/mg of silicon. We determined the concentration of Si using inductively coupled plasma-atomic

emission spectroscopy (ICP-AES) and the concentration of drug using nuclear magnetic resonance spectroscopy (NMR). The pSiNC pore volume of 0.48 cm^3/g as determined by BET adsorption measurements indicating that only 21% of the maximum theoretical pore volume was loaded with the Sorafenib tosylate. The release of the drug from the porous silicon matrix in phosphate buffered saline was studied at 37^0C at t = 0,1,4,6 and 8 hrs and the drug concentration determined by NMR using a calibrated standard curve with an R^2 of 0.997. The values obtained were normalized as a percentage of total drug released in 24 hours (Fig 5.2a). A student's t test describes the difference in release of sorafenib tosylate between pegylated and non pegylated sorafenib tosylate loaded pSiNC as not significant.

Furthermore, we observed no degradation of porous silicon, release of drug or iron oxide nanoparticles at 4^0C. This implies that degradation of the porous matrix is crucial to release of drugs and iron oxide nanoparticles (not shown).

(iii) Change in self diffusion coefficient of water: measuring degradation and transverse relaxation

As described in the introduction, the self diffusion coefficient of water and the time taken for a water molecule to move between magnetic environments determines the relaxation mechanism of protons in the presence of iron oxide nanoparticles. In a previous study, the ability of a porous matrix to change the self diffusion coefficient of water was investigated. This study revealed that differences in self diffusion coefficient of water inside and outside the porous

matrix results in iron oxide nanoparticles presenting different relaxivities. Plot 4.1c in Chapter 4 describes the change in relaxation time with change in diffusion coefficient. The diffusion coefficient (Di/D0) of a degrading porous matrix was observed to increase from 0.35 relative to bulk water at t=0, 0.79 at t=4 and 1 relative to bulk water at t=8 and t=24. Figure 5.3a describes this mechanism in greater detail. Figure 5.3b compares r2 or relaxivity coefficient in a 24 hour time span between degraded nanoparticles and porous silicon nanoparticles that are in the process of degrading.

(iv)Correlating the release of iron oxide nanoparticles and drug: Implications on determining drug release with transverse relaxation measurements

In Figure 5.4a, we plot the change in transverse relaxation with percentage drug released. We observe a linear relationship between change in r2 and percentage sorafenib tosylate released. This implies that release of drug from a porous matrix can be determined with nuclear magnetic resonance spectroscopy. The release of a hydrophillic drug, 5 fluorouracil from porous silicon iron oxide nanocomposites was also studied (Figure 5.4c). We observed a non linear relationship between change in r2 and percentage of 5-fluorouracil released. As a hydrophilic drug, 5-fluorouracil can be released from the porous matrix by diffusion and degradation of porous silicon. Therefore, porous silicon iron oxide nanocomposites would be most suitable in quantifying the release of hydrophobic drugs from porous matrices.

5.5 CONCLUSION

Indirect monitoring of drug release by imaging enables the visualization and also quanitification of drug release. By enabling visualization of drug targeting systems and delivery of pharmacologically active agents to the pathological site and the rate of delivery, theranostic nanomedicine formulations furthermore facilitate the efficacy of combination regimens. Porous silicon iron oxide nanocomposites can be used to enable the temporal and spatial analysis of target site accumulation, and this information can be used to define an optimal timing for combination with other therapeutic modalities. Attempts can be made to correlate the in vitro characteristics of drug carriers to their in vivo capabilities by imaging (the kinetics of) drug release in vivo. Additionally, this technology could be used to load and release other therapeutic agents such as proteins and peptides, although the stability of proteins and peptides in a degrading environment needs to be considered.

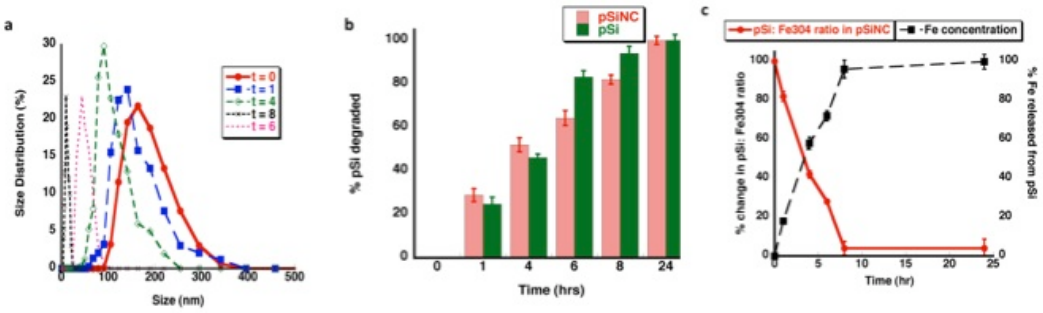

Figure 5.1 : Plot a describes the change in size as the nanocomposite degrades, the hydrodynamic diamter was measured by Dynamic Light scattering at different points during the degradation process. b) This plot describes the percentage porous silicon degrades at 37C in PBS in the time frame of 0-24 hours. The degradation profile for porous silicon and porous silicon iron oxide nanocomposites were compared. c) This plot describes the release of iron during the degradation process as measured by ICP-OES. The ratio of pSi: Fe304 in the nanocomposite and the % of iron released from pSi were shown in this figure.

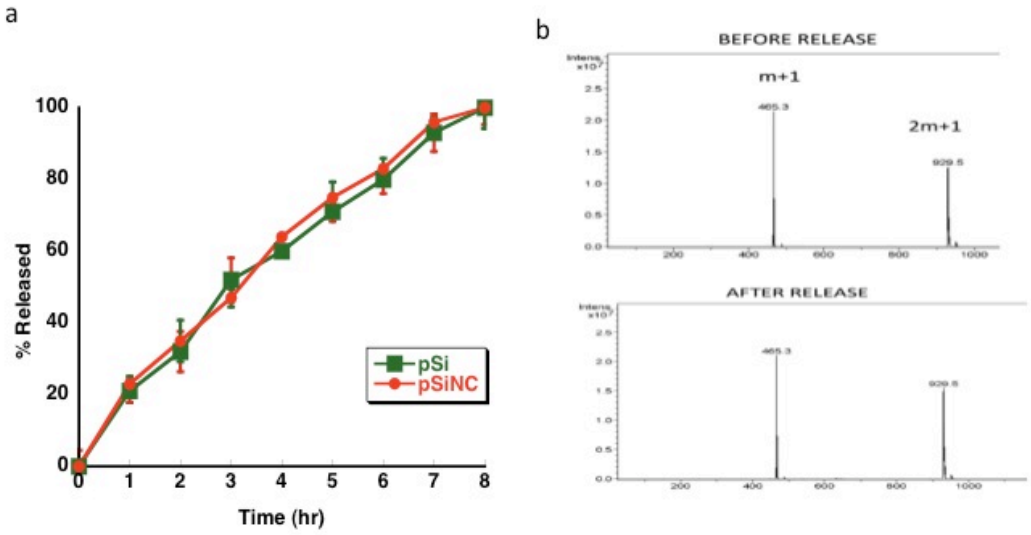

Figure 5.2 a) This plot describes the release of drug sorafenib tosylate from pSi and pSiNC during the time frame 0-24 hr as measured with NMR spectrosocopy. b) This plot confirms that the chemical composition of sorafenib tosylate remains unaltered before and after release.

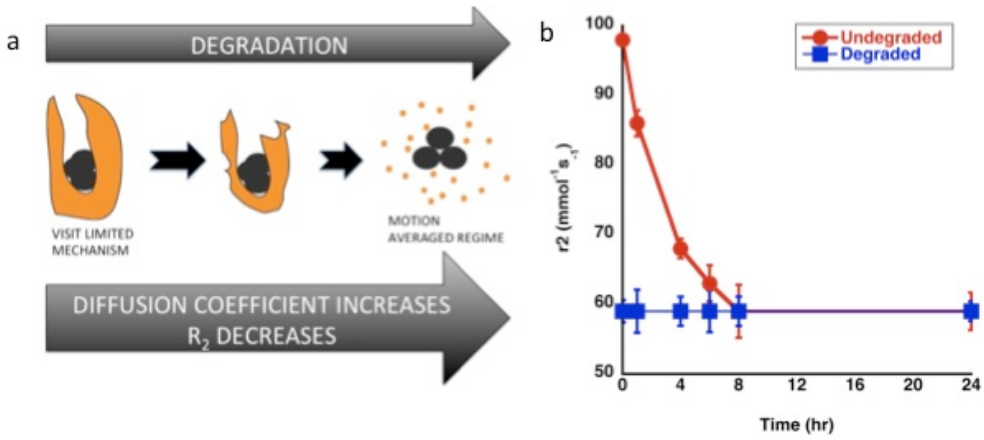

Figure 5.3: a) This schematic describes the change in regime experienced by protons confined within a porous silicon matrix before and after degradation. b) describes the change in r2 once the nanocomposites degrade in the presence of water at 37^0C. The r2 of degraded nanocomposites were compared against degraded nanocomposites.

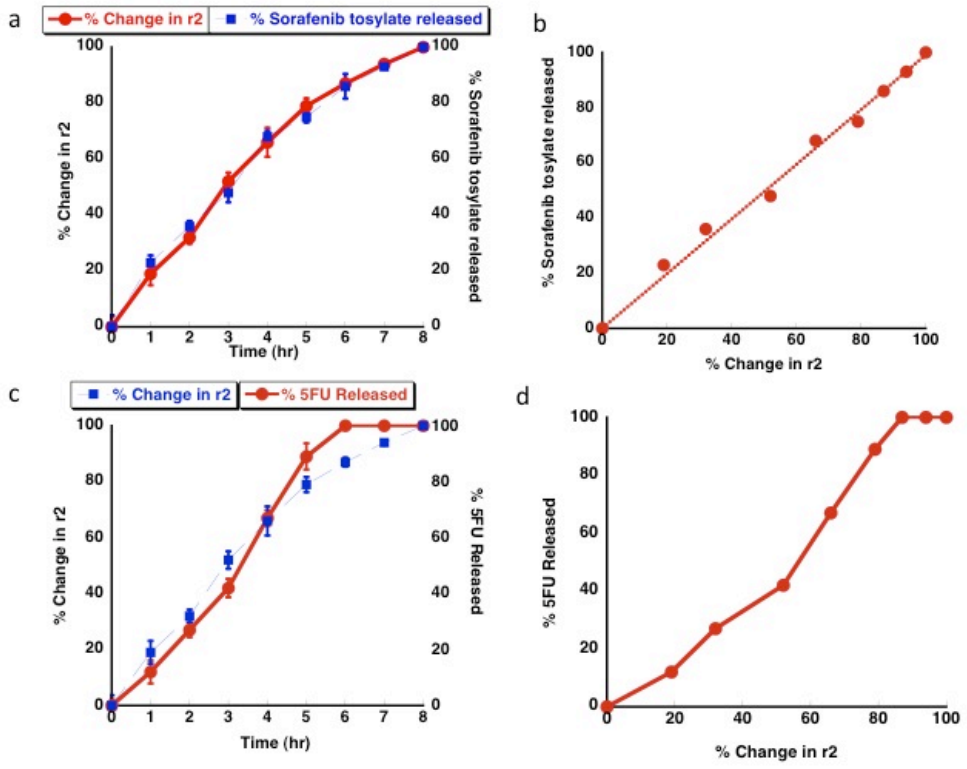

Figure 5.4 a) This figure shows the percentage change in r2 with percentage sorafenib tosylate released over 8 hours. b) The direct relationship between percentage sorafenib tosylate released and percentage change in r2 is shown here. c) This figure shows the percentage change in r2 and percentage change in 5-fluorouracil released over time. d) The direct relationship between percentage 5 fluorouracil released and percentage change in r2 is shown here.

REFERENCES:

[1] S. M. Janib, A. S. Moses, and J. A. MacKay, "Imaging and drug delivery using theranostic nanoparticles," Advanced drug delivery reviews, vol. 62, pp. 1052-1063, 2010.

[2] D. Sun, "Nanotheranostics: integration of imaging and targeted drug delivery," Molecular Pharmaceutics, vol. 7, p. 1879, 2010.

[3] B. L. Viglianti, M. W. Dewhirst, and A. M. Ponce, "MRI imageable liposomes for the evaluation of treatment efficacy, thermal distribution, and demonstration of dose painting," ed: Google Patents, 2010.

[4] B. L. Viglianti, "Target molecular therapies: methods to enhance and monitor tumor drug delivery," Abdominal imaging, vol. 34, pp. 686-695, 2009.

[5] D. W. McRobbie, MRI from picture to proton: Cambridge Univ Pr, 2003.

[6] Y. Gossuin, A. Roch, R. N. Muller, and P. Gillis, "An evaluation of the contributions of diffusion and exchange in relaxation enhancement by MRI contrast agents," Journal of Magnetic Resonance, vol. 158, pp. 36-42, 2002.

[7] A. Roch, Y. Gossuin, R. N. Muller, and P. Gillis, "Superparamagnetic colloid suspensions: water magnetic relaxation and clustering," Journal of Magnetism and Magnetic Materials, vol. 293, pp. 532-539, 2005.

[8] Y. Gossuin, A. Roch, R. N. Muller, P. Gillis, and F. Lo Bue, "Anomalous nuclear magnetic relaxation of aqueous solutions of ferritin: An unprecedented first order mechanism," Magnetic Resonance in Medicine, vol. 48, pp. 959-964, 2002.

[9] Y. Gossuin, P. Gillis, A. Hocq, Q. L. Vuong, and A. Roch, "Magnetic resonance relaxation properties of superparamagnetic particles," Wiley Interdisciplinary Reviews: Nanomedicine and Nanobiotechnology, vol. 1, pp. 299-310, 2009.

[10] P. Gillis, F. Moiny, and R. A. Brooks, "On T2 shortening by strongly magnetized spheres: A partial refocusing model," Magnetic resonance in medicine, vol. 47, pp. 257-263, 2002.

[11] J. Siepmann, K. Podual, M. Sriwongjanya, N. Peppas, and R. Bodmeier, "A new model describing the swelling and drug release kinetics from hydroxypropyl methylcellulose tablets," Journal of pharmaceutical sciences, vol. 88, pp. 65-72, 1999.

6 CONCLUSIONS AND FUTURE DIRECTION

CHAPTER 6 CONCLUSION AND FUTURE DIRECTION

6.1 CONCLUSION

6.2 Future Directions: Improvements to chemical design of contrast agents

6.2.1. Factors to consider for MR Contrast Enhancement

6.2.2. Altering size of magnetic nanoparticles

6.2.3. Altering magnetic dopant in magnetic nanoparticles

6.2.4. Metal-Alloy magnetic nanoparticles

6.3 Potential applications: Applying physiologically based pharmacokinetic modeling towards screening contrast agents

6.4 Potential application of porous silicon iron oxide nanocomposites for diagnosis and treatment for diseases

6.4.1 Imaging Autoimmune Disorders

6.4.2. Therapeutic Applications – radiofrequency ablation

6.1 Conclusion

Image guided drug delivery in cancer is a form of individualized therapy where imaging methods are used in guidance and monitoring of localized and targeted delivery of therapeutics to the tumor. A systematic approach to IGDD requires mechanisms for targeting, delivery, activation and monitoring of the process. While the goal of IGDD is to optimize the therapeutic ratio through personalized

image guided treatments, a major is in the overcoming the biological barriers to the delivery of therapeutics into tumors and cells. Physiological and quantitative imaging techniques may serve as enabling tools that could potentially transform many existing challenges into opportunities for advancement of the field.

The overreaching goal in IGDD is to optimize the therapeutic ratio ideally through optimized biodistribution, pharmacokinetic and pharmacokinetic of drugs and personalization of oncologic therapies. The full implementation of IGDD requires (a) drugs that can be imaged, localized or targeted and activated at the tumor site and (b) imaging techniques that provide anatomic and quantitative functional measures of the process at various spatial and temporal resolutions for active monitoring. Imaging can play a vital role in validating drug delivery but also in PK, PD and biodistribution studies of therapeutic agents.

The difficulties associated with bringing MRI molecular imaging into research practice are apparent when surveying the subset of the experimental strategies that have been validated so far in animals. In most cases, large concentrations of contrast media are required, generally well over 10 μM. Commerical software for pharamcokinetic and pharmacodynamic analysis[84] takes into account the kinetic effects of the agent likely to influence imaging data would be delivery to the site, competing effects between target and background binding rates, biliary and renal clearance rates.Table 7.1 describes a situation where different conditions including target concentration, clearance and plasma protein binding for iron oxide nanoparticles were assessed for imaging feasibility. The simulation

parameters used here were obtained from various parts of the literature[84]. This indicates that even under seemily favorable circumstances, a high concentration of iron oxide is required to generate sufficient contrast for imaging. In this regard, the most successful strategies are those in which molecular imaging agents have been directed at relatively superficial analytes, or where the agents have been able to exploit endogenous mechanisms to reach their targets.

In vivo successes include agents designed to target relatively accessible physiological markers in the vasculature, and genetically encoded agents that avoid the need for exogenous delivery. Strong SPIO T2 contrast agents have been designed to bind vascular epitopes to detect cerebral inflammation [85].

Table 6.1 uses the imaging feasibility criteria described in Chapter 6 to determine the imaging feasibility under different situations involving target concentration, renal and biliary clerance and plasma protein binding.

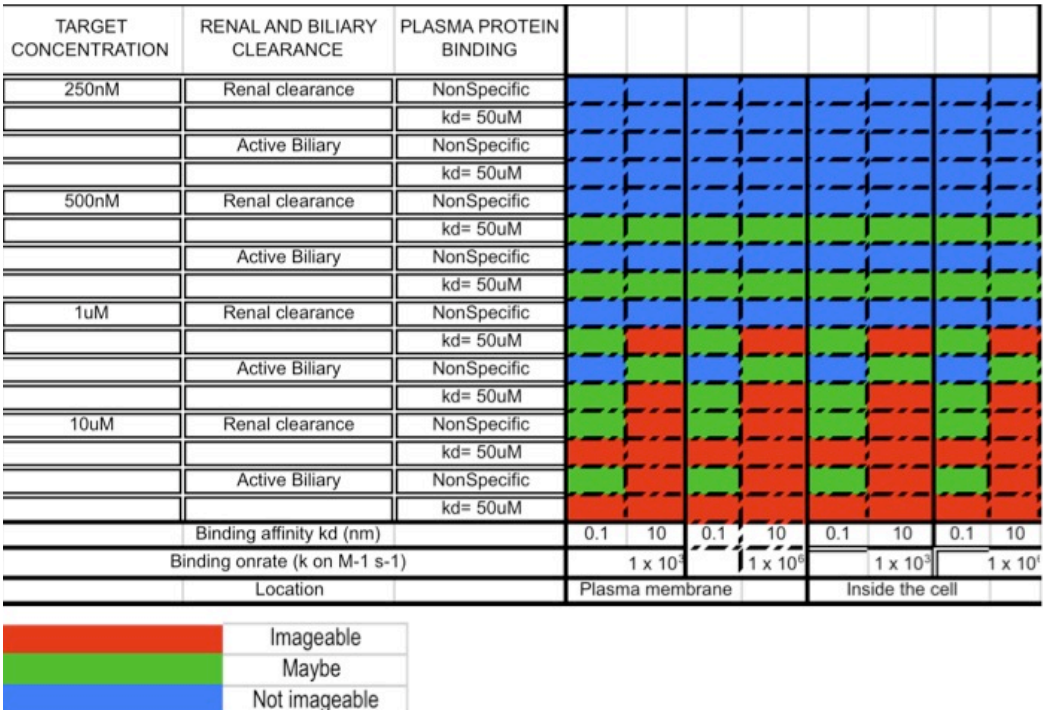

The most broadly applied molecular imaging method is based on injected paramagnetic Mn2+ ions that appear to accumulate in an activity-dependent manner in the brain by promiscuous uptake through neuronal voltage gated calcium channels [86] The ability to stimulate for long periods of time in the presence of Mn2+ has been critical to achieving reliable contrast, indicating [87] that fairly high local concentrations of Mn2+ are necessary for detection [88]. In recent in vivo applications, hyperpolarization-based imaging techniques have been applied to follow 13C-labeled bicarbonate and metabolites [89], each of which is associated with established families of transporters and processing enzymes.

Like Mn2+, and also in analogy to PET tracers, 13C-labeled agents can exploit endogenous uptake mechanisms. Using hyperpolarization methods, the sensitivity with which 13C compounds are detected can be boosted by many orders of magnitude though their potential for imaging applications may be hindered by limits on polarization lifetime. Hyperpolarized 13C agents can be constructed in similar fashion and may be imaged with no noticeable contribution from endogenous 13C but currently only over periods on the order of a minute. Extending the utility of hyperpolarization-based molecular imaging may require nuclei with longer lasting polarization lifetimes [90], or continuous polarization methods [91]. A sensitive technique for molecular imaging based on hyperpolarized 129Xe gas and targeted Xe-binding cryptophane cages has also been proposed and may have interesting advantages.

For the generic MRI molecular imaging agent, which may be highly polar, nanometer sized, or directed toward intracellular targets of exceptional significance, it is clearly not possible to rely on endogenous transport mechanisms for delivery into cells. It may be possible to engineer genetically encoded contrast agents to generate more complex functionality like responsiveness to intracellular signaling genetically encoded species are generally less effective contrast agents than synthetic molecules, and of course could only be used in transgenic or transfected animals. For imaging applications involving exogenous agents, efficient artificial delivery techniques are required.

Molecular functions performed by MRI contrast agents may also induce disruptions. For instance, an MRI probe designed to target a cell surface receptor will almost certainly interfere with receptor transport and binding of the molecule by its natural ligands. Such complications are common to almost all drugs and imaging agents, but are especially severe for MRI molecular imaging probes, because of the high concentrations required. There is therefore a particularly acute need to improve the sensitivity of MRI detection of molecular imaging agents.

To mitigate difficulties associated with delivery, and to reduce potentially adverse effects of agents introduced into the body, a closely related aim is required to improve MRI contrast agents, so that lower concentrations are required for detection. In the remainder of this review, we discuss critical challenges involved with developing effective strategies for molecular MRI, focusing particularly on advances in delivery methodology and sensitivity that may be critical to relatively near-term applications of newly developed molecular imaging agents in live animals.

For all of the delivery techniques, there is a clear advantage to minimizing the amount of contrast agent required for imaging, and where large quantities of contrast agent are required, pathological side effects related to the agents themselves may also be incurred. Many MRI contrast agents incorporate paramagnetic heavy metals such as gadolinium and manganese, which as bare ions are extremely toxic even at low concentrations. Dissociated Gd3+, for

instance, inhibits calcium-dependent processes in cells and induces a nephrotoxicity syndrome at doses of about 0.3 mmol/kg [92]. Chronic exposure to manganese is associated with neurological disorders [93] hepatic failure and cardiac toxicity and Mn2+ doses as low as 93 mg/kg for rats and 38 mg/kg for mice have been shown to cause serious adverse effects [88a]. SPIOs present a risk if iron escapes from nanoparticle cores [94]; chelation and additional treatments may be required in subjects where high doses of iron-containing contrast agents are used [95]

As with imaging agents for other modalities, signal changes produced by MRI contrast agents may be difficult to detect either because they are small compared with scanner-related noise levels, or because of relatively high background from endogenous MRI signals, including physiological sources. The CEST technique provides one way to remove background influences, because the chemical shift of saturation can be varied to excite test or control proton pools [96]. The chemical-shift dependence of CEST has allowed pH mapping, and facilitates creation of CEST molecular imaging probes [97], where analyte measurement does not depend on the concentration of the probe, as well as “multicolor” agents that can be imaged in parallel because they have different saturation frequencies [98]. Heteronuclear imaging agents provide an alternative way to improve molecular imaging performance by minimizing background. 19F is the most common isotope of fluorine and can be detected relatively efficiently by MRI, but is not present endogenously in the body. Both unresponsive and responsive 19F

probes have been synthesized and 19F imaging agents have been used recently where large local 19F levels were obtainable and relatively low resolutions were used for scanning[99]. In some cases, it is possible to synthesize fluorinated analogs of previously characterized compounds to produce MRI-detectable tracers with properties similar to the parent molecules; this approach was used in a recent demonstration of amyloid plaque detection by 19F MRI.

A number of MRI molecular imaging approaches have now been reported to have met the requirements for delivery and sensitivity well enough to be validated in vivo. Although challenges remain, an MRI-based toolbox for noninvasive molecular image guided drug delivery at the whole-body level in animals could be within reach of today's technology.

REFERENCES

1. Pautler, R. G.; Silva, A. C.; Koretsky, A. P., In vivo neuronal tract tracing using manganese enhanced magnetic resonance imaging. Magnetic Resonance in Medicine 1998, 40 (5), 740-748.

2. Aoki, I.; Wu, Y. J. L.; Silva, A. C.; Lynch, R. M.; Koretsky, A. P., In vivo detection of neuroarchitecture in the rodent brain using manganese-enhanced MRI. Neuroimage 2004, 22 (3), 1046-1059.

3. Lee, J. H.; Silva, A. C.; Merkle, H.; Koretsky, A. P., Manganese enhanced magnetic resonance imaging of mouse brain after systemic administration of MnCl2: Dose,Äêdependent and temporal evolution of T1 contrast. Magnetic Resonance in Medicine 2005, 53 (3), 640-648.

4. Koretsky, A. P.; Silva, A. C., Manganese enhanced magnetic resonance imaging (MEMRI). NMR in Biomedicine 2004, 17 (8), 527-531.

5. Golman, K.; Lerche, M.; Pehrson, R.; Ardenkjaer-Larsen, J. H., Metabolic imaging by hyperpolarized 13C magnetic resonance imaging for in vivo tumor diagnosis. Cancer research 2006, 66 (22), 10855-10860.

6. Serres, S.; Anthony, D. C.; Jiang, Y.; Broom, K. A.; Campbell, S. J.; Tyler, D. J.; van Kasteren, S. I.; Davis, B. G.; Sibson, N. R., Systemic inflammatory response reactivates immune-mediated lesions in rat brain. The Journal of Neuroscience 2009, 29 (15), 4820-4828.

7. Van Kasteren, S. I.; Campbell, S. J.; Serres, S.; Anthony, D. C.; Sibson, N. R.; Davis, B. G., Glyconanoparticles allow pre-symptomatic in vivo imaging of brain disease. Proceedings of the National Academy of Sciences 2009, 106 (1), 18-23;

8. Garcia Martin, M. L.; Martinez, G. V.; Raghunand, N.; Sherry, A. D.; Zhang, S.; Gillies, R. J., High resolution pHe imaging of rat glioma using pH,Äêdependent relaxivity. Magnetic Resonance in Medicine 2006, 55 (2), 309-315.

9. McMahon, M. T.; Gilad, A. A.; DeLiso, M. A.; Cromer Berman, S. M.; Bulte, J. W. M.; van Zijl, P., New ‚Äúmulticolor‚Äù polypeptide diamagnetic chemical exchange saturation transfer (DIACEST) contrast agents for MRI. Magnetic Resonance in Medicine 2008, 60 (4), 803-812.

10. Cohen, B.; Ziv, K.; Plaks, V.; Israely, T.; Kalchenko, V.; Harmelin, A.; Benjamin, L. E.; Neeman, M., MRI detection of transcriptional regulation of gene expression in transgenic mice. Nature medicine 2007, 13 (4), 498-503.

11. Goldhawk, D. E.; Rohani, R.; Sengupta, A.; Gelman, N.; Prato, F. S., Using the magnetosome to model effective gene‚Äêbased contrast for magnetic resonance imaging. Wiley Interdisciplinary Reviews: Nanomedicine and Nanobiotechnology 2012.

12. Kuo, P. H.; Kanal, E.; Abu-Alfa, A. K.; Cowper, S. E., Gadolinium-based MR Contrast Agents and Nephrogenic Systemic Fibrosis1. Radiology 2007, 242 (3), 647-649.

13. Chandra, S. V.; Shukla, G. S., Role of iron deficiency in inducing susceptibility to manganese toxicity. Archives of toxicology 1976, 35 (4), 319-323.

14. Longmire, M.; Choyke, P. L.; Kobayashi, H., Clearance properties of nano-sized particles and molecules as imaging agents: considerations and caveats. Nanomedicine 2008, 3 (5), 703-717.

15. Leite, F. P.; Tsao, D.; Vanduffel, W.; Fize, D.; Sasaki, Y.; Wald, L. L.; Dale, A. M.; Kwong, K. K.; Orban, G. A.; Rosen, B. R., Repeated fMRI using iron oxide contrast agent in awake, behaving macaques at 3 Tesla. Neuroimage 2002, 16 (2), 283-294.

16. Sherry, A. D.; Woods, M., Chemical exchange saturation transfer contrast agents for magnetic resonance imaging. Annual review of biomedical engineering 2008, 10, 391.

17. Ward, K.; Aletras, A.; Balaban, R., A new class of contrast agents for MRI based on proton chemical exchange dependent saturation transfer (CEST). Journal of Magnetic Resonance 2000, 143 (1), 79-87.

18. Zhang, S.; Merritt, M.; Woessner, D. E.; Lenkinski, R. E.; Sherry, A. D., PARACEST agents: modulating MRI contrast via water proton exchange. Accounts of chemical research 2003, 36 (10), 783-790.

19. Zabow, G.; Dodd, S.; Moreland, J.; Koretsky, A., Micro-engineered local field control for high-sensitivity multispectral MRI. Nature 2008, 453 (7198), 1058-1063.

20. Higuchi, M.; Iwata, N.; Matsuba, Y.; Sato, K.; Sasamoto, K.; Saido, T. C., 19F and 1H MRI detection of amyloid Œ≤ plaques in vivo. Nature neuroscience 2005, 8 (4), 527-533.

21. Dementyev, A.; Cory, D.; Ramanathan, C., Dynamic nuclear polarization in silicon microparticles. Physical review letters 2008, 100 (12), 127601.

22. Brunner, E.; Haake, M.; Kaiser, L.; Pines, A.; Reimer, J., Gas Flow MRI Using Circulating Laser-Polarized129Xe. Journal of Magnetic Resonance 1999, 138 (1), 155-159.

FUTURE DIRECTIONS

6.2. Improvements to chemical design of contrast agents

This thesis focuses on the physical design of iron oxide nanoparticles to improve contrast in magnetic resonance imaging. Chemical parameters of magnetic materials such as size of magnetic nanoparticles, altering magnetic dopants levels and metal alloy magnetic nanoparticles contribute to an increase in moment of a nanoparticle. The combination of physical and chemical parameters can result in development of higher relaxivity contrast agents than the ones present today.

6.2.1. Factors to consider for MR Contrast Enhancement

The outer sphrere relaxation model with magnetic nanoparticles. R2 of a proton can be determined by: [67]

$$R2 = \frac{1}{T2} = \left(\frac{32\pi}{405}\right)\gamma^2\mu^2\frac{N_A}{1000}\left(\frac{[M]}{rD}\right)\{6.5j_2(\omega_s) + 1.5j_1(\omega_1) + 2j_1(0)\}$$

(Equation 1)

Where, γ_I is the gyromagnetic ratio of protons in water, M is the molarity of the magnetic nanoparticle, r is its radius, μ is the magnetic moment of the nanoparticle, ω_S and ω_I are the Larmor angular precession frequencies of the nanoparticle electric moment and water proton magnetic moment.

$$j_n(\omega,\tau,\tau_{Sn}) = \mathrm{Re}\left(\frac{1+1/4\left(i\omega\tau+\tau/\tau_{Sn}\right)^{1/2}}{1+\left(i\omega\tau+\tau/\tau_{Sn}\right)+\frac{4}{9}\left(i\omega\tau+\tau/\tau_{Sn}\right)+\frac{1}{9}\left(i\omega\tau+\tau/\tau_{Sn}\right)^{\frac{3}{2}}}\right)^2$$

(Equation 2)

The functions $j_n(\omega,\tau)$ are spectral density functions in which Re is the real part of the expression that follows in parenthesis, $\tau = \frac{r^2}{D}$ is the time scale of fluctuations in the particle–water proton magnetic dipolar interaction arising from the relative diffusive motion (D) of a particle with respect to water molecules, and τ_{S1} and τ_{S2} are the lifetimes of the longitudinal and transverse components of μ [67]

To maximize R2: the factors affecting R2 must be considered:

(i) the magnetic moment (μ)

(ii) relaxation processes of the magnetic spin (τ_{S1},τ_{S2})

The magnetic moment (μ) of the nanoparticle is dependent on the

(i) size,

(ii) composition, and

(iii) magneto-crystalline phase of the nanoparticle.

The lifetimes of the longitudinal and transverse components of μ correlate with the magneto-crystalline phase of the nanoparticles [63]. Hence, the above three factors can be modulated to increase R2 and R2* relaxation rate.

Monodisperse magnetic nanoparticles are typically prepared through the thermal decomposition of metal-complex precursors in hot non-hydrolytic organic solution containing surfactants [52]. Thermal decomposition of the precursors generates monomers and their aggregation above a supersaturation level induces nucleation and subsequent nanoparticle growth [100]. During these stages, by tuning growth parameters, such as monomer concentration, crystalline phase of the nuclei, choice of solvent and surfactants, growth temperature and time, and surface energy, it is possible to control the size, composition, and magneto-crystalline phase of magnetic nanoparticles. For example, there have been many reports on the synthesis of metal ferrite nanoparticles from precursors such as iron pentacarbonyl, iron cupferron, iron tris(2,4-pentadionate), and iron fatty acid complexes, in hot organic solvents containing fatty acids and amine surfactants [52].

6.2.2 Altering Size of magnetic nanoparticles

One important parameter for the MR contrast-enhancement effect of magnetic nanoparticles is their size. In the ideal case, all of the magnetic spins in a bulk magnetic material are aligned parallel to the external magnetic field. Surface spin-canting effects of magnetic nanoparticles have a significant influence on their magnetic moments and MR contrast-enhancement effects [52]. A study reported where the variation of their size from 4 nm to 6 nm, 9 mm, and 12 nm resulted in mass-magnetization values of 25, 43, 80, and 101 emu per gram Fe [28]. As the nanoparticle size decreases, the surface effect becomes more

pronounced and is reflected in the reduced net magnetic moment [101]. Such size-dependent magnetism directly influences the MR enhancement effect.

6.2.3. Altering Magnetic-Dopant in magnetic nanoparticles

The magnetism of nanoparticles can be greatly influenced by doping with magnetically susceptible elements. This is demonstrated for MFe_2O_4 nanoparticles in which Fe^{2+} ions are replaced by other transition-metal dopants M^{2+} where M=Mn, Ni, Co [28].Ferrimagnetic Fe_3O_4 has a crystallographically inverse spinel structure constructed of face-centered cubic packed lattice of oxygen atoms with the tetrahedral sites (T_d) occupied by Fe^{3+} ions and octahedral sites (O_h) occupied by Fe^{3+} and Fe^{2+} ions. Under an external magnetic field, the magnetic spins of the ions at the O_h sites align parallel to the external magnetic field but those at T_d sites align antiparallel to the field [101]. Given that Fe^{3+} has a d^5 configuration and Fe^{2+} has a d^6 configuration with a high spin state, the total magnetic moment per unit $(Fe^{3+})(Fe^{2+}Fe^{3+})O_4$ is 4 $\mu_.$ [28].

These metal-doped nanoparticles can induce significant MR contrast increase effects

6.2.4. Metal-Alloy magnetic nanoparticles

Metal alloys magnetic nanoparticles, such as FeCo and FePt have been studied as magnetic probes. In these magnetic nanoparticles all the magnetic spins align parallel to the external magnetic field, as a result they typically have higher magnetic moments than those of ferrimagnetic nanoparticles. For example, the

magnetic moment of FeCo magnetic alloys is approximately 2.4 μ_B per magnetic atom, while that of Fe_3O_4 is approximately 1.3 μ_B per magnetic atom [28].

An example of this would be the development of 7 nm sized FeCo magnetic nanoparticles passivated with a graphite shell. These FeCo magnetic nanoparticles have a high magnetization value of 215 emu per gram metal. The coefficient r2 of has been determined to be 644 mm^{-1} s^{-1}, which is much larger than that of conventional SPIO contrast agents, such as Feridex (ca. 100 mm^{-1} s^{-1}) [102]

6.3. Applying physiologically based pharmacokinetic (PBPK) modeling towards screening contrast agents

One of the most important questions regarding nanoparticle in vivo studies is the transportation kinetics or the extent and rate they distribute among various tissues within the body. Simulation of the experimental data could provide information that cannot otherwise be obtained due to measurement, time limitations and tissues that are not feasible for detection [103].

By PBPK modeling, the ADME (absorption, distribution, metabolism and excretion) of nanoparticles can be systematically described and understood, Essentially, PBPK models could aid in finding factors that influence the nanoparticle distribution and further reducing toxicity and improving efficacy [104].

One of the major applications of PBPK could be the dose determination of nanoparticles for humans from animal data, in cancer therapy and imaging. The

relevance between the data obtained from animal models to human has been a prodidious argument. PBPK models provide the possibility of scale-up data from animal models to humans, which will greatly enhance applications of nanoparticle and PBPK studies can assist in this procees [105].

Nanoparticle properties can be controlled through chemical composition [106], surface engineering, and preparation processes [105]. PBPK models have been utilized to predict the activity based on available information of other similar chemical compounds called quantitative structure−activity relationships [107]. This possibility could find significant application in nanoparticle design and optimization.

Another application with high potential is for nanoparticle drug carrier delivery kinetics.[107]. The PBPK model of nanoparticles and that of the drug can be combined together, linked by the drug release kinetics from the nanoparticles. This model will be able to address the effects of nanoparticle distribution and drug release kinetics on the pharmacokinetics of the encapsulated drugs.

6.4 Potential application of porous silicon iron oxide nanocomposites for diagnosis and treatment for disease.

Porous silicon iron oxide nanocomposites produce a physical amplication of magnetic resonance contrast. These nanoparticles can be utilized to treat diseases that are presently in early stages of research.

6.4.1 Imaging Autoimmune Disorders

Multiple Sclerosis and acute disseminated encephalomyelitis are immune-mediated disorders of the central nervous sytem. In previous studies, SPIO-enhanced MRI reveals areas of hypointensity on T_2*-weighted images correspond to SPIO-laden mononuclear cells within inflammatory lesions. [108]. To validate the use of SPIOs as a noninvasive tool for evaluating therapeutic strategies in this condition, Floris et al treated animals with the immunomodulator, 3-hydroxy-3-methylglutaryl Coenzyme A reductase inhibitor or lovastatin. MRI revealed that the SPIO load in the body was significantly diminished in lovastatin-treated animals and this correlated with improved clinical scores [108]. Improvements in early disease detection are clearly needed in this field and porous silicon iron oxide nanocomposites that are conjugated to vascular cell adhesion molecule-1 may allow for earlier detection, estimates of disease severity, and monitoring of therapy [109].

6.4.2 Therapeutic Applications via radiofrequency ablation

The porous silicon iron oxide nanocomposites can be used for hyperthermic ablation of CNS tumors after direct inoculation into tumors, or IV administration, depending on the agent's biodistribution. Targeted porous silicon iron oxide nanoparticles are exposed to an alternating magnetic field, which produces electrical current and subsequent energy dispersion in the form of heat. Superparamagnetic species with single magnetic domains dissipate heat as a result of relaxation of the domain dipole, a process known as Neel relaxation [110].

Porous silicon iron oxide nanocomposites use 9nm iron oxides and one can presume that it would take a far lower-strength magnetic fields to achieve the same level of heating as larger ferromagnetic agents.

One limitation of this treatment strategy has been target specificity. Postmortem studies of patients with recurring cancer enrolled in the feasibility trial showed that dispersed particles and particle aggregates were phagocytosed mainly by macrophages, whereas glioblastoma (cancer) cells showed uptake to a minor extent. [111] In this regard, targeted porous silicon iron oxide nanocomposites can be used to detect localization and perform radio frequency ablation. Porous silicon iron oxide nanocomposites have a temperature related R2 dependance, this can be used to monitor temperature and also release anti-cancer drugs.

REFERENCES:

1. Peer, D.; Karp, J. M.; Hong, S.; Farokhzad, O. C.; Margalit, R.; Langer, R., Nanocarriers as an emerging platform for cancer therapy. *Nature Nanotechnology* **2007,** *2* (12), 751-760.

2. Park, J. H.; Gu, L.; von Maltzahn, G.; Ruoslahti, E.; Bhatia, S. N.; Sailor, M. J., Biodegradable luminescent porous silicon nanoparticles for in vivo applications. *Nature materials* **2009,** *8* (4), 331-336.

3. Xie, J.; Jon, S., Magnetic Nanoparticle-Based Theranostics. *Theranostics* **2012,** *2* (1), 122.

4. Sawyers, C., Targeted cancer therapy. *Nature* **2004,** *432* (7015), 294-297.

5. Ginsburg, G. S.; McCarthy, J. J., Personalized medicine: revolutionizing drug discovery and patient care. *TRENDS in Biotechnology* **2001,** *19* (12), 491-496.

6. Woodcock, J., The prospects for ‚Äúpersonalized medicine‚Äù in drug development and drug therapy. *Clinical Pharmacology & Therapeutics* **2007,** *81* (2), 164-169.

7. Weissleder, R., Molecular imaging in cancer. *Science* **2006,** *312* (5777), 1168.

8. Kumar, C. S. S. R., *Nanomaterials for medical diagnosis and therapy*. Vch Verlagsgesellschaft Mbh: 2007; Vol. 10.

9. Zou, P.; Yu, Y.; Wang, Y. A.; Zhong, Y.; Welton, A. R.; Galb n, C.; Wang, S.; Sun, D., Superparamagnetic iron oxide nanotheranostics for targeted cancer cell imaging and pH-dependent intracellular drug release. *Molecular pharmaceutics* **2010**.

10. Park, J. H.; Von Maltzahn, G.; Xu, M. J.; Fogal, V.; Kotamraju, V. R.; Ruoslahti, E.; Bhatia, S. N.; Sailor, M. J., Cooperative nanomaterial system to sensitize, target, and treat tumors. *Proceedings of the National Academy of Sciences* **2010,** *107* (3), 981.

11. Janib, S. M.; Moses, A. S.; MacKay, J. A., Imaging and drug delivery using theranostic nanoparticles. *Advanced drug delivery reviews* **2010,** *62* (11), 1052-1063.

12. Sun, D., Nanotheranostics: integration of imaging and targeted drug delivery. *Molecular Pharmaceutics* **2010,** *7* (6), 1879.

13. Hamburg, M. A.; Collins, F. S., The path to personalized medicine. *New England Journal of Medicine* **2010,** *363* (4), 301-304.

14. de Smet, M.; Heijman, E.; Langereis, S.; Hijnen, N.; Gr√ºll, H., Magnetic resonance imaging of high intensity focused ultrasound mediated drug delivery from temperature sensitive liposomes; An in vivo proof-of-concept study. *Journal of Controlled Release* **2010**.

15. Delli Castelli, D.; Dastr√π, W.; Terreno, E.; Cittadino, E.; Mainini, F.; Torres, E.; Spadaro, M.; Aime, S., < i> In vivo</i> MRI multicontrast kinetic analysis of the uptake and intracellular trafficking of paramagnetically labeled liposomes. *Journal of Controlled Release* **2010,** *144* (3), 271-279.

16. Onuki, Y.; Jacobs, I.; Artemov, D.; Kato, Y., Noninvasive visualization of in vivo release and intratumoral distribution of surrogate MR contrast agent using the dual MR contrast technique. *Biomaterials* **2010,** *31* (27), 7132-7138.

17. Mulder, W. J. M.; Strijkers, G. J.; Habets, J. W.; Bleeker, E. J. W.; van der Schaft, D. W. J.; Storm, G.; Koning, G. A.; Griffioen, A. W.; Nicolay, K., MR molecular imaging and fluorescence microscopy for identification of activated tumor endothelium using a bimodal lipidic nanoparticle. *The FASEB journal* **2005,** *19* (14), 2008-2010.

18. Viglianti, B. L.; Ponce, A. M.; Michelich, C. R.; Yu, D.; Abraham, S. A.; Sanders, L.; Yarmolenko, P. S.; Schroeder, T.; MacFall, J. R.; Barboriak, D. P., Chemodosimetry of in vivo tumor liposomal drug concentration using MRI. *Magnetic resonance in medicine* **2006,** *56* (5), 1011-1018.

19. Ponce, A. M.; Viglianti, B. L.; Yu, D.; Yarmolenko, P. S.; Michelich, C. R.; Woo, J.; Bally, M. B.; Dewhirst, M. W., Magnetic resonance imaging of temperature-sensitive liposome release: drug dose painting and antitumor effects. *Journal of the National Cancer Institute* **2007,** *99* (1), 53-63.

20. Viglianti, B. L.; Dewhirst, M. W.; Ponce, A. M., MRI imageable liposomes for the evaluation of treatment efficacy, thermal distribution, and demonstration of dose painting. Google Patents: 2010.

21. Palmer, G. M.; Boruta, R. J.; Viglianti, B. L.; Lan, L.; Spasojevic, I.; Dewhirst, M. W., Non-invasive monitoring of intra-tumor drug concentration and therapeutic response using optical spectroscopy. *Journal of Controlled Release* **2010,** *142* (3), 457-464.

22. Langereis, S.; Keupp, J.; van Velthoven, J. L. J.; de Roos, I. H. C.; Burdinski, D.; Pikkemaat, J. A.; GruÃàll, H., A temperature-sensitive liposomal 1H CEST and 19F contrast agent for MR image-guided drug delivery. *Journal of the American Chemical Society* **2009,** *131* (4), 1380-1381.

23. Xie, J.; Lee, S.; Chen, X., Nanoparticle-based theranostic agents. *Advanced drug delivery reviews* **2010,** *62* (11), 1064-1079.

24. Anglin, E. J.; Cheng, L.; Freeman, W. R.; Sailor, M. J., Porous silicon in drug delivery devices and materials. *Advanced drug delivery reviews* **2008,** *60* (11), 1266-1277.

25. Kim, D.; Zhang, Y.; Voit, W.; Rao, K.; Muhammed, M., Synthesis and characterization of surfactant-coated superparamagnetic monodispersed iron

oxide nanoparticles. *Journal of magnetism and Magnetic Materials* **2001,** *225* (1), 30-36.

26. Kohler, N.; Fryxell, G. E.; Zhang, M., A bifunctional poly (ethylene glycol) silane immobilized on metallic oxide-based nanoparticles for conjugation with cell targeting agents. *Journal of the American Chemical Society* **2004,** *126* (23), 7206-7211.

27. Hwu, J. R.; Lin, Y. S.; Josephrajan, T.; Hsu, M. H.; Cheng, F. Y.; Yeh, C. S.; Su, W. C.; Shieh, D. B., Targeted Paclitaxel by conjugation to iron oxide and gold nanoparticles. *Journal of the American Chemical Society* **2008,** *131* (1), 66-68.

28. Lee, J. H.; Huh, Y. M.; Jun, Y.; Seo, J.; Jang, J.; Song, H. T.; Kim, S.; Cho, E. J.; Yoon, H. G.; Suh, J. S., Artificially engineered magnetic nanoparticles for ultra-sensitive molecular imaging. *Nature medicine* **2006,** *13* (1), 95-99.

29. Jain, T. K.; Richey, J.; Strand, M.; Leslie-Pelecky, D. L.; Flask, C. A.; Labhasetwar, V., Magnetic nanoparticles with dual functional properties: drug delivery and magnetic resonance imaging. *Biomaterials* **2008,** *29* (29), 4012-4021.

30. Yu, M. K.; Jeong, Y. Y.; Park, J.; Park, S.; Kim, J. W.; Min, J. J.; Kim, K.; Jon, S., Drug,ÄêLoaded Superparamagnetic Iron Oxide Nanoparticles for Combined Cancer Imaging and Therapy In Vivo. *Angewandte Chemie International Edition* **2008,** *47* (29), 5362-5365.

31. Piao, Y.; Kim, J.; Na, H. B.; Kim, D.; Baek, J. S.; Ko, M. K.; Lee, J. H.; Shokouhimehr, M.; Hyeon, T., Wrap,Äìbake,Äìpeel process for nanostructural

transformation from Œ≤-FeOOH nanorods to biocompatible iron oxide nanocapsules. *Nature materials* **2008,** *7* (3), 242-247.

32. Cheng, K.; Peng, S.; Xu, C.; Sun, S., Porous hollow Fe3O4 nanoparticles for targeted delivery and controlled release of cisplatin. *Journal of the American Chemical Society* **2009,** *131* (30), 10637-10644.

33. Ito, A.; Shinkai, M.; Honda, H.; Kobayashi, T., Medical application of functionalized magnetic nanoparticles. *Journal of bioscience and bioengineering* **2005,** *100* (1), 1-11.

34. Shinkai, M.; Le, B.; Honda, H.; Yoshikawa, K.; Shimizu, K.; Saga, S.; Wakabayashi, T.; Yoshida, J.; Kobayashi, T., Targeting hyperthermia for renal cell carcinoma using human MN antigenspecific magnetoliposomes. *Cancer Science* **2001,** *92* (10), 1138-1146.

35. Lewinski, N.; Colvin, V.; Drezek, R., Cytotoxicity of nanoparticles. *Small* **2008,** *4* (1), 26-49.

36. Jiang, W.; Kim, B. Y. S.; Rutka, J. T.; Chan, W. C. W., Nanoparticle-mediated cellular response is size-dependent. *Nature Nanotechnology* **2008,** *3* (3), 145-150.

37. Gupta, A. K.; Gupta, M., Cytotoxicity suppression and cellular uptake enhancement of surface modified magnetic nanoparticles. *Biomaterials* **2005,** *26* (13), 1565-1573.

38. Buzea, C.; Pacheco, I. I.; Robbie, K. In *Nanomaterials and nanoparticles: sources and toxicity*, AVS: 2007.

39. Mansfield, P.; Morris, P. G., *NMR imaging in biomedicine*. Academic Press New York: 1982; Vol. 37.

40. Fisher, M. R.; Wall, S. D.; Hricak, H.; McCarthy, S.; Kerlan, R., Hepatic vascular anatomy on magnetic resonance imaging. *American journal of roentgenology* **1985,** *144* (4), 739-746.

41. Callaghan, P. T., *Principles of nuclear magnetic resonance microscopy*. Clarendon Press Oxford: 1993.

42. Hornak, J. P., The basics of MRI. *Disponvel em< http://www. cis. rit. edu/htbooks/mri>. Acesso em* **1996,** *8*.

43. McRobbie, D. W., *MRI from picture to proton*. Cambridge Univ Pr: 2003.

44. Hashemi, R. H.; Bradley, W. G.; Lisanti, C. J., *MRI: the basics*. Lippincott Williams & Wilkins: 2010.

45. Steckel, R. J.; Kagan, A. R., *Diagnosis and staging of cancer: a radiologic approach*. WB Saunders Company: 1976.

46. Bydder, G.; Felix, R.; Bucheler, E., Contrast Media in MRI. *Bussum, The Netherlands, Medicom* **1990**.

47. Westbrook, C.; Roth, C. K.; Talbot, J., *MRI in Practice*. Wiley-Blackwell: 2005.

48. Pekar, J. J., A brief introduction to functional MRI. *Engineering in Medicine and Biology Magazine, IEEE* **2006,** *25* (2), 24-26.

49. Laurent, S.; Forge, D.; Port, M.; Roch, A.; Robic, C.; Vander Elst, L.; Muller, R. N., Magnetic iron oxide nanoparticles: synthesis, stabilization,

vectorization, physicochemical characterizations, and biological applications. *Chemical reviews* **2008,** *108* (6), 2064.

50. Corot, C.; Robert, P.; Idee, J. M.; Port, M., Recent advances in iron oxide nanocrystal technology for medical imaging. *Advanced drug delivery reviews* **2006,** *58* (14), 1471-1504.

51. Bronstein, L. M.; Huang, X.; Retrum, J.; Schmucker, A.; Pink, M.; Stein, B. D.; Dragnea, B., Influence of iron oleate complex structure on iron oxide nanoparticle formation. *Chemistry of materials* **2007,** *19* (15), 3624-3632.

52. Park, J.; An, K.; Hwang, Y.; Park, J. G.; Noh, H. J.; Kim, J. Y.; Park, J. H.; Hwang, N. M.; Hyeon, T., Ultra-large-scale syntheses of monodisperse nanocrystals. *Nature materials* **2004,** *3* (12), 891-895.

53. William, W. Y.; Falkner, J. C.; Yavuz, C. T.; Colvin, V. L., Synthesis of monodisperse iron oxide nanocrystals by thermal decomposition of iron carboxylate salts. *Chemical communications* **2004,** (20), 2306-2307.

54. Canham, L., *Properties of porous silicon*. IEE Books: 1997; Vol. 4.

55. Searson, P.; Macaulay, J.; Prokes, S. M., The formation, morphology, and optical properties of porous silicon structures. *Journal of The Electrochemical Society* **1992,** *139*, 3373.

56. Gillis, P.; Moiny, F.; Brooks, R. A., On T2 shortening by strongly magnetized spheres: A partial refocusing model. *Magnetic resonance in medicine* **2002,** *47* (2), 257-263.

57. Washington, C., Drug release from microdisperse systems: a critical review. *International journal of pharmaceutics* **1990,** *58* (1), 1-12.

58. Edelman, R. R.; Warach, S., Magnetic resonance imaging. *New England Journal of Medicine* **1993,** *328* (10), 708-716.

59. Westbrook, C., *MRI at a glance*. Wiley-Blackwell: 2009; Vol. 17.

60. Mitchell, D. G.; Cohen, M. S., *MRI principles*. Saunders: 1999.

61. Fukushima, E.; Roeder, S. B. W., *Experimental pulse NMR: a nuts and bolts approach*. Addison-Wesley Reading, MA:: 1981.

62. Kim, J.; Kim, H. S.; Lee, N.; Kim, T.; Kim, H.; Yu, T.; Song, I. C.; Moon, W. K.; Hyeon, T., Multifunctional uniform nanoparticles composed of a magnetite nanocrystal core and a mesoporous silica shell for magnetic resonance and fluorescence imaging and for drug delivery. *Angewandte Chemie International Edition* **2008,** *47* (44), 8438-8441.

63. Gossuin, Y.; Roch, A.; Muller, R. N.; Gillis, P., An evaluation of the contributions of diffusion and exchange in relaxation enhancement by MRI contrast agents. *Journal of Magnetic Resonance* **2002,** *158* (1-2), 36-42.

64. Roch, A.; Gossuin, Y.; Muller, R. N.; Gillis, P., Superparamagnetic colloid suspensions: water magnetic relaxation and clustering. *Journal of Magnetism and Magnetic Materials* **2005,** *293* (1), 532-539.

65. Berret, J. F.; Schonbeck, N.; Gazeau, F.; El Kharrat, D.; Sandre, O.; Vacher, A.; Airiau, M., Controlled clustering of superparamagnetic nanoparticles using block copolymers: design of new contrast agents for magnetic resonance imaging. *Journal of the American Chemical Society* **2006,** *128* (5), 1755-1761.

66. Chen, D. X.; Sun, N.; Huang, Z. J.; Cheng, C. M.; Xu, H.; Gu, H. C., Experimental study on T2 relaxation time of protons in water suspensions of iron-

oxide nanoparticles: effects of polymer coating thickness and over-low 1/T2. *Journal of Magnetism and Magnetic Materials* **2010,** *322* (5), 548-556.

67. Gossuin, Y.; Gillis, P.; Hocq, A.; Vuong, Q. L.; Roch, A., Magnetic resonance relaxation properties of superparamagnetic particles. *Wiley Interdisciplinary Reviews: Nanomedicine and Nanobiotechnology* **2009,** *1* (3), 299-310.

68. Brooks, R. A.; Moiny, F.; Gillis, P., On T2,Äêshortening by weakly magnetized particles: The chemical exchange model,Ä†. *Magnetic resonance in medicine* **2001,** *45* (6), 1014-1020.

69. Brooks, R. A., T2,Äêshortening by strongly magnetized spheres: A chemical exchange model,Ä†. *Magnetic Resonance in Medicine* **2002,** *47* (2), 388-391.

70. Cho, K.; Wang, X.; Nie, S.; Shin, D. M., Therapeutic nanoparticles for drug delivery in cancer. *Clinical Cancer Research* **2008,** *14* (5), 1310-1316.

71. Maeda, H.; Wu, J.; Sawa, T.; Matsumura, Y.; Hori, K., Tumor vascular permeability and the EPR effect in macromolecular therapeutics: a review. *Journal of Controlled Release* **2000,** *65* (1-2), 271-284.

72. (a) Duan, H.; Kuang, M.; Wang, X.; Wang, Y. A.; Mao, H.; Nie, S., Reexamining the effects of particle size and surface chemistry on the magnetic properties of iron oxide nanocrystals: New insights into spin disorder and proton relaxivity. *The Journal of Physical Chemistry C* **2008,** *112* (22), 8127-8131; (b) Hardy, P.; Henkelman, R., Transverse relaxation rate enhancement caused by magnetic particulates. *Magnetic resonance imaging* **1989,** *7* (3), 265-275.

73. Gossuin, Y.; Roch, A.; Muller, R. N.; Gillis, P.; Lo Bue, F., Anomalous nuclear magnetic relaxation of aqueous solutions of ferritin: An unprecedented first‚Äêorder mechanism. *Magnetic Resonance in Medicine* **2002,** *48* (6), 959-964.

74. Binder, K., *Monte‚ÄêCarlo Methods*. Wiley Online Library: 1979.

75. Matsumoto, Y.; Jasanoff, A., < i> T</i>< sub> 2</sub> relaxation induced by clusters of superparamagnetic nanoparticles: Monte Carlo simulations. *Magnetic resonance imaging* **2008,** *26* (7), 994-998.

76. Qiu, P.; Jensen, C.; Charity, N.; Towner, R.; Mao, C., Oil phase evaporation-induced self-assembly of hydrophobic nanoparticles into spherical clusters with controlled surface chemistry in an oil-in-water dispersion and comparison of behaviors of individual and clustered iron oxide nanoparticles. *Journal of the American Chemical Society* **2010**.

77. Muller, R.; Vander Elst, L.; Roch, A.; Peters, J.; Csajbok, E.; Gillis, P.; Gossuin, Y., Relaxation by metal-containing nanosystems. *Advances in Inorganic Chemistry* **2005,** *57*, 239-292.

78. Larsen, B.; Haag, M.; Serkova, N.; Shroyer, K.; Stoldt, C., Controlled aggregation of superparamagnetic iron oxide nanoparticles for the development of molecular magnetic resonance imaging probes. *Nanotechnology* **2008,** *19*, 265102.

79. Chen, D. X.; Sun, N.; Gu, H. C., Size analysis of carboxydextran coated superparamagnetic iron oxide particles used as contrast agents of magnetic resonance imaging. *Journal of Applied Physics* **2009,** *106* (6), 063906-063906-9.

80. Bowen, C. V.; Zhang, X.; Saab, G.; Gareau, P. J.; Rutt, B. K., Application of the static dephasing regime theory to superparamagnetic iron‚Äêoxide loaded cells. *Magnetic Resonance in Medicine* **2002,** *48* (1), 52-61.

81. Linke, H.; Mansson, A., *Controlled nanoscale motion*. Springer.

82. LaConte, L. E. W.; Nitin, N.; Zurkiya, O.; Caruntu, D.; O'Connor, C. J.; Hu, X.; Bao, G., Coating thickness of magnetic iron oxide nanoparticles affects R2 relaxivity. *Journal of Magnetic Resonance Imaging* **2007,** *26* (6), 1634-1641.

83. Viglianti, B. L., Target molecular therapies: methods to enhance and monitor tumor drug delivery. *Abdominal imaging* **2009,** *34* (6), 686-695.

84. Barrett, P. H. R.; Bell, B. M.; Cobelli, C.; Golde, H.; Schumitzky, A.; Vicini, P.; Foster, D. M., SAAM II: simulation, analysis, and modeling software for tracer and pharmacokinetic studies. *Metabolism* **1998,** *47* (4), 484-492.

85. Serres, S.; Anthony, D. C.; Jiang, Y.; Broom, K. A.; Campbell, S. J.; Tyler, D. J.; van Kasteren, S. I.; Davis, B. G.; Sibson, N. R., Systemic inflammatory response reactivates immune-mediated lesions in rat brain. *The Journal of Neuroscience* **2009,** *29* (15), 4820-4828.

86. Pautler, R. G.; Silva, A. C.; Koretsky, A. P., In vivo neuronal tract tracing using manganese‚Äêenhanced magnetic resonance imaging. *Magnetic Resonance in Medicine* **1998,** *40* (5), 740-748.

87. Lee, J. H.; Silva, A. C.; Merkle, H.; Koretsky, A. P., Manganese‚Äêenhanced magnetic resonance imaging of mouse brain after systemic administration of MnCl2: Dose‚Äêdependent and temporal evolution of T1 contrast. *Magnetic Resonance in Medicine* **2005,** *53* (3), 640-648.

88. (a) Koretsky, A. P.; Silva, A. C., Manganese,Äêenhanced magnetic resonance imaging (MEMRI). *NMR in Biomedicine* **2004,** *17* (8), 527-531; (b) Gallagher, F. A.; Kettunen, M. I.; Day, S. E.; Hu, D. E.; Ardenkj√ ¯ ¶ r-Larsen, J. H., Magnetic resonance imaging of pH in vivo using hyperpolarized 13C-labelled bicarbonate. *Nature* **2008,** *453* (7197), 940-943.

89. Golman, K.; Lerche, M.; Pehrson, R.; Ardenkjaer-Larsen, J. H., Metabolic imaging by hyperpolarized 13C magnetic resonance imaging for in vivo tumor diagnosis. *Cancer research* **2006,** *66* (22), 10855-10860.

90. Dementyev, A.; Cory, D.; Ramanathan, C., Dynamic nuclear polarization in silicon microparticles. *Physical review letters* **2008,** *100* (12), 127601.

91. Brunner, E.; Haake, M.; Kaiser, L.; Pines, A.; Reimer, J., Gas Flow MRI Using Circulating Laser-Polarized129Xe. *Journal of Magnetic Resonance* **1999,** *138* (1), 155-159.

92. Kuo, P. H.; Kanal, E.; Abu-Alfa, A. K.; Cowper, S. E., Gadolinium-based MR Contrast Agents and Nephrogenic Systemic Fibrosis1. *Radiology* **2007,** *242* (3), 647-649.

93. Chandra, S. V.; Shukla, G. S., Role of iron deficiency in inducing susceptibility to manganese toxicity. *Archives of toxicology* **1976,** *35* (4), 319-323.

94. Longmire, M.; Choyke, P. L.; Kobayashi, H., Clearance properties of nano-sized particles and molecules as imaging agents: considerations and caveats. *Nanomedicine* **2008,** *3* (5), 703-717.

95. Leite, F. P.; Tsao, D.; Vanduffel, W.; Fize, D.; Sasaki, Y.; Wald, L. L.; Dale, A. M.; Kwong, K. K.; Orban, G. A.; Rosen, B. R., Repeated fMRI using iron oxide

contrast agent in awake, behaving macaques at 3 Tesla. *Neuroimage* **2002,** *16* (2), 283-294.

96. Sherry, A. D.; Woods, M., Chemical exchange saturation transfer contrast agents for magnetic resonance imaging. *Annual review of biomedical engineering* **2008,** *10*, 391.

97. Ward, K.; Aletras, A.; Balaban, R., A new class of contrast agents for MRI based on proton chemical exchange dependent saturation transfer (CEST). *Journal of Magnetic Resonance* **2000,** *143* (1), 79-87.

98. McMahon, M. T.; Gilad, A. A.; DeLiso, M. A.; Cromer Berman, S. M.; Bulte, J. W. M.; van Zijl, P., New ‚Äúmulticolor‚Äù polypeptide diamagnetic chemical exchange saturation transfer (DIACEST) contrast agents for MRI. *Magnetic Resonance in Medicine* **2008,** *60* (4), 803-812.

99. Higuchi, M.; Iwata, N.; Matsuba, Y.; Sato, K.; Sasamoto, K.; Saido, T. C., 19F and 1H MRI detection of amyloid Œ≤ plaques in vivo. *Nature neuroscience* **2005,** *8* (4), 527-533.

100. Asmatulu, R.; Zalich, M. A.; Claus, R. O.; Riffle, J. S., Synthesis, characterization and targeting of biodegradable magnetic nanocomposite particles by external magnetic fields. *Journal of Magnetism and Magnetic Materials* **2005,** *292*, 108-119.

101. Lu, A. H.; Salabas, E. L.; Sch√ºth, F., Magnetic nanoparticles: synthesis, protection, functionalization, and application. *Angewandte Chemie International Edition* **2007,** *46* (8), 1222-1244.

102. Seo, W. S.; Lee, J. H.; Sun, X.; Suzuki, Y.; Mann, D.; Liu, Z.; Terashima, M.; Yang, P. C.; McConnell, M. V.; Nishimura, D. G., FeCo/graphitic-shell nanocrystals as advanced magnetic-resonance-imaging and near-infrared agents. *Nature materials* **2006,** *5* (12), 971-976.

103. Nestorov, I., Whole-body physiologically based pharmacokinetic models. **2007**.

104. Willmann, S.; H√ ∂ hn, K.; Edginton, A.; Sevestre, M.; Solodenko, J.; Weiss, W.; Lippert, J.; Schmitt, W., Development of a physiology-based whole-body population model for assessing the influence of individual variability on the pharmacokinetics of drugs. *Journal of pharmacokinetics and pharmacodynamics* **2007,** *34* (3), 401-431.

105. Fallon, M. S.; Varshney, M.; Dennis, D. M.; Chauhan, A., A physiologically-based pharmacokinetic model of drug detoxification by nanoparticles. *Journal of pharmacokinetics and pharmacodynamics* **2004,** *31* (5), 381-400.

106. Lee, H. A.; Leavens, T. L.; Mason, S. E.; Monteiro-Riviere, N. A.; Riviere, J. E., Comparison of quantum dot biodistribution with a blood-flow-limited physiologically based pharmacokinetic model. *Nano letters* **2009,** *9* (2), 794-799.

107. Li, M.; Al-Jamal, K. T.; Kostarelos, K.; Reineke, J., Physiologically based pharmacokinetic modeling of nanoparticles. *ACS nano* **2010**.

108. Floris, S.; Blezer, E.; Schreibelt, G.; D√ ∂ pp, E.; van der Pol, S.; Schadee,ÄêEestermans, I.; Nicolay, K.; Dijkstra, C.; De Vries, H., Blood,Äìbrain

barrier permeability and monocyte infiltration in experimental allergic encephalomyelitis. *Brain* **2004,** *127* (3), 616-627.

109. McAteer, M. A.; Sibson, N. R.; von zur Muhlen, C.; Schneider, J. E.; Lowe, A. S.; Warrick, N.; Channon, K. M.; Anthony, D. C.; Choudhury, R. P., In vivo magnetic resonance imaging of acute brain inflammation using microparticles of iron oxide. *Nature medicine* **2007,** *13* (10), 1253-1258.

110. Hartman, K. B.; Wilson, L. J.; Rosenblum, M. G., Detecting and treating cancer with nanotechnology. *Molecular Diagnosis &# 38; Therapy* **2008,** *12* (1), 1-14.

111. van Landeghem, F. K. H.; Maier-Hauff, K.; Jordan, A.; Hoffmann, K. T.; Gneveckow, U.; Scholz, R.; Thiesen, B.; Br√¯ºck, W.; von Deimling, A., Post-mortem studies in glioblastoma patients treated with thermotherapy using magnetic nanoparticles. *Biomaterials* **2009,** *30* (1), 52-57.

APPENDIX

```
/*********MONTE CARLO SIMULATION*************************/


/* This program uses Monte Carlo random walk simulation to find  T2* value of*/

/* iron oxide particles. Written by Shalini Ananda*/

/* 1.  Field */

/* 2. Particle Radius */

/* 3. MRI Sequence Type */

/* 4. Length */

/* 5. Magnetic Suspectibility outside the particle */

/* 6.  Magnetic  Susceptibility inside the particle */

/* 7. STEPLENGTH */

/* 8. TE */

/* 9. NUM_PROTONS */

/* */

/************************************************************************/
```

```
/**** EDIT FOLLOWING*******/

#define FIELD       3// Background magnetic field (in Tesla)

#define MEAN_RADIUS   9// Radius of particle (nm)

#define LENGTH 2048 // Length of model (nanometers)

#define CONCENTRATION 0.00001 // Particle concentration

#define MU_1 1.000000 // Magnetic susceptibility outside

#define MU_2 1.000006 // Magnetic susceptibility inside

#define STEPLENGTH 128 // Gridsize (nanometers)



/*Defining constant for Monte Carlo simulation*/

#define SEQTYPE 0 // Sequence type (1 for spin-echo , 0 for gradient echo)

#define TE 100 // Echo time (milliseconds)

#define NUM_PROTONS 500 // Number of protons in simulation

#define D 1300000  // Diffusion coefficient (nanometers^2/milliseconds)

#define dt 0.02 //     Step time (seconds)

#define RESOLUTION 1 // Resolution for diffusion length
```

```
/*********************************************************************/

/* Include files*/

#include <stdio.h>

#include <stdlib.h>

#include <math.h>

#include <time.h>

/*Declare program arrays*/

double fieldarray
[LENGTH/STEPLENGTH][LENGTH/STEPLENGTH][LENGTH/STEPLENGTH];

int
particlearray[LENGTH/STEPLENGTH][LENGTH/STEPLENGTH][LENGTH/STEP
LENGTH];

double startloc [3][NUM_PROTONS];

double phasearray[NUM_PROTONS][5001];

double cumulativephase [NUM_PROTONS];

double cosarray [NUM_PROTONS];

double sinarray[NUM_PROTONS];
```

```
/*Initialize variables */

double standard_dev=1 // Standard deviation of particle size

double pi = 3.141;

double phase, cos_sum, sin_sum;



/***********PICKING THE STARTING LOCATION OF EACH PROTON**********/

int pickstart(int offset, double mean_rad)  {

        int repick = ceil (NUM_PROTONS/20);

        double xstart[repick];

        double ystart [repick];

        double zstart [repick];



/*Clear all variables */

double xnew = 0;

double ynew = 0;

double znew  = 0;
```

```
int k, m, x0, y0, z0;

/*Randomly choose proton starting locations*/

for (k=0; k<repick: k++) {

xstart[k] = drand48()*LENGTH;

ystart[k] = drand48()*LENGTH;

zstart[k] = drand48()*LENGTH;



}



/**Repicking starting locations if proton is located inside a particle**/

for (m=0; m<repack; m++)                {



x0 = floor(xstart[m]/STEPLENGTH);

y0 = floor(ystart[m]/STEPLENGTH);

z0 = floor(zstart[m]/STEPLENGTH);



while (particlearray[x0][y0][z0] == 1)   {
```

```
x0 = floor(xstart[m]/STEPLENGTH);

y0 = floor(ystart[m]/STEPLENGTH);

z0 = floor(zstart[m]/STEPLENGTH);




//Randomly select next proton position

double xg = drand48()  - 0.5;

double yg = drand48() -  0.5;

double zg = drand48() - 0.5;


xnew = xstart[m] + (xg * ((sqrt(2*D*dt))) *  RESOLUTION);

ynew= ystart[m] + (yg * ((sqrt(2*D*dt))) * RESOLUTION);

znew = zstart[m] + (zg * ((sqrt(2*D*dt))) * RESOLUTION);

xstart[m] = xnew ;  ystart[m] = ynew ; zstart[m]= znew;


}
```

```
// Calculate new proton locations

startloc[1][m] = xstart[m]  *  RESOLUTION + offset;

startloc[2][m] = ystart[m]  * RESOLUTION + offset;

startloc[3][m] = zstart[m]  * RESOLUTION + offset;



}



return 0;



}



/********************* THE MONTE CARLO WALK*****************************/

int walksim(int offset) {



/*INITIALIZE SETTINGS*/

int err,  indicator,  j,  k;
```

```
double xnew, ynew, znew, xold, yold, zold;



/*Step proton */

for (j=1; j<NUM_PROTONS; j++)  {

int index = ceil (j/20);

xnew  =  startloc[1][index];

ynew  =  startloc[2][index];

znew  =  startloc[3][index];



int accumphase = 0;

for (k=1; k<ceil(TE/(2*dt)); k++) {



        err = 1;

        indicator =1;

        while (err == 1) {
```

```
xold = xnew;

yold = ynew;

zold = znew;



// Randomly select next proton position

double xg = drand48() – 0.5;

double yg = drand48() – 0.5;

double zg = drand48() – 0.5;



xnew = xold + (xg  *  ((sqrt(2*D*dt))) * RESOLUTION);

ynew = yold + (yg  *  ((sqrt(2*D*dt))) * RESOLUTION);

znew = zold + (zg  *  ((sqrt(2*D*dt))) * RESOLUTION);



//Perform data check

if (floor(xnew  >= LENGTH) { xnew = (LENGTH) -1; err=0; }

if (floor(ynew  >= LENGTH) { ynew = (LENGTH) -1; err =0 }

if(floor(znew  >= LENGTH) {  znew =(LENGTH )-1 ; err=0; }
```

```
if (xnew < 0)  { xnew = 0 ; err =0; }

if (ynew < 0)  {ynew = 0; err =0; }

if (znew < 0)  {znew =0;  err= 0; }




int xloc = floor(xnew/STEPLENGTH);

int yloc = floor(ynew/STEPLENGTH);

int zloc = floor(znew/STEPLENGTH);



err = particlearray[xloc][yloc][zloc]



        }



// Calculate new phase of proton



evalphase(xnew, ynew, znew, xold, yold, zold, indicator, offset);

phasearray[j][k] = phase;
```

```
xold = xnew;

yold = ynew;

zold = znew;



}



// Repeat walk and also flipping phase for spin echo sequence

for (k=(ceil(TE/ (2*dt)) +1);  k<ceil(TE/dt); k++)   {



        err =1;



if (SEQTYPE  == 1) {    indicator = -1;  }

else  { indicator=1; }

        while (err == 1) {



xold = xnew;
```

```
yold = ynew;

zold = znew;



// Random selection of the next proton position

double xg= drand48() – 0.5;

double yg = drand48() – 0.5;

double zg = drand48() – 0.5;



xnew = xold + (xg * ((sqrt (2*D*dt))) * RESOLUTION);

ynew = yold + (yg * ((sqrt(2*D*dt))) *  RESOLUTION);

znew = zold + (zg * ((sqrt(2*D*dt))) * RESOLUTION):



// Perform data check

if (floor(xnew) >= LENGTH { xnew = (LENGTH)-1 ; err = 0; }

if (floor(ynew) >= LENGTH { ynew = (LENGTH) -1; err =0; }

if(floor(znew) >= LENGTH  {znew = (LENGTH) -1 ; err =0; }

if (xnew < 0 ) { xnew = 0; err = 0; }
```

```
if (ynew < 0 ) { ynew= 0; err= 0; }

if (znew < 0)  {znew = 0; err = 0; }



int xloc  =  floor(xnew/STEPLENGTH);

int yloc  =  floor(ynew/STEPLENGTH);

int zloc  =  floor(znew/STEPLENGTH);



err = particlearray[xloc][yloc][zloc];



        }



// Calculate new phase of proton



evalphase(xnew,ynew, znew, xold, yold, zold, indicator, offset);

phasearray[j][k] = phase;



xold = xnew;
```

```
yold = ynew;

zold = znew;

}



        }



return 0;



}



/************************To calculate acquired phase*******************/

int evalphase(double xn, double yn, double zn, double xo, double yo, double zo,

int indicator, int offset)

{



int xnew =  abs(floor(xn/STEPLENGTH));

int ynew=  abs (floor(yn/STEPLENGTH));
```

```
int znew=  abs(floor (zn/STEPLENGTH));

int xold =  abs(floor  (xo/STEPLENGTH));

int yold = abs (floor (yo/STEPLENGTH));

int zold = abs (floor (zo/STEPLENGTH));

double gamma = 267510;

double averageB = (fieldarray[xnew][ynew][znew] + fieldarray[xold][yold][zold]) /2 ;



phase = gamma * averageB  *dt * indicator;

return 0;



}



int builduniverse(double mean_rad)

{



/* Declare variables*/

double accumulator;
```

```
double accumulatorold;

double temporary;

double diameter;

double P;

double denominator;

int sphere;

int x,y,z,n,m;



/*INITIALIZE*/

double Bfield = FIELD

double sphere_radius = mean_rad;



/*INITIALIZE SETTINGS*/



int arraysize = LENGTH;

double arraysize_float = LENGTH;

int step_length = STEPLENGTH;
```

```
int numspheres =
ceil(arraysize_float*arraysize_float*arraysize_float*CONCENTRATION/
(4*pi*pwrf(sphere_radius,3)/3));


/*Declare arrays*/


int xpos[numspheres];
in ypos[numspheres];
int zpos[numspheres];


/********** Randomly choose locations of iron oxide particles ********/
srand( (unsigned) time (NULL ) );
for (m=0; m<numspheres; m++) {
        xpos[m] = rand()%arraysize;
        ypos[m] = rand()% arraysize;
        zpos[m] = rand() % arraysize;
```

```
}

/***** Create array of spaced intervals and specify location of iron oxide *****/

for  (sphere=0; sphere<numspheres; sphere++) {
for (x=xpos[sphere]-ceil(sphere_radius); x < (xpos[sphere]+ceil(sphere_radius));
x++) {
for (y=ypos[sphere]-ceil(sphere_radius); y < (ypos[sphere]+ceil(sphere_radius));
y++) {
for (z=zpos[sphere]-ceil(sphere_radius); z < (zpos[sphere]+ceil(sphere_radius));
z++) {
if  ((0 < x) & (arraysize > x) & (0 < y) & (arraysize > y) & (0 < z) & (arraysize > z))
{
if (sqrt(pwr(x-xpos[sphere],2) + pwr (y-ypos[sphere],2)+pwr(z-zpos[sphere],
2)) <=sphere_radius)  {

                int xr = floor(x/step_length);
                int yr = floor (y/step_length);
```

```
                int zr = floor (z/step_length)

                particlearrary[xr][yr][zr] = 1;

                }

        }

}




                }

        }

}


/********** Determine magnetic field values*****************/

for (x=0; x< arraysize;  x+= step_length) {

        for  (y=0; y < arraysize; y+= step_length) {

                for  (z=0; z<arraysize; z+=step_length) {


int xr = floor(x/step_length);
```

```
int yr = floor (y/step_length);

int zr = floor (z/ step_length);

if (particlearray [xr][yr][zr] == 1 ) {

fieldarray[xr][yr][zr] = Bfield*(1+ (MU_OUTSIDE -1)/3);

}



else if (particlearray[xr][yr][zr] < 1) {

accumulator = 0;

for (sphere =0, sphere<numspheres; sphere++) {

accumulatorold = accumulator;



if ((pwr(x-xpos[sphere],2) + pwr(y-ypos[sphere],2) + pwr(z-zpos[sphere],2)) < 1) {

temporary = 0;



}
```

```
else if  ((pwr(x-xpos[sphere],2) + pwr(y-ypos[sphere],2) + pwr(z-zpos[sphere],2))
> 0) {


denominator =sqrt(pwr(x-xpos[sphere],2) + pwr(y-ypos[sphere],2) +pwr(z-
zpos[sphere],2));


temporary = (((MU_2 -1)/3 )+ (MU_2-
MU_1*(sphere_radius*sphere_radius*sphere_radius)*((pwr(x-xpos[sphere],2) +
pwr(y-ypos[sphere],2) -2*pwr(z-zpos[sphere],2))) / (3*pwrf(denominator,5)) );
}


accumulator = temporary + accumulatorold;



}


fieldarray[xr][yr][zr] =Bfield*(1+ accumulator);
}
                    }
```

```
        }
}
return 0;



}

/******* The function computes power of a float*******************************/
int pwrf (double value, int power) {
        int i;
        double result  = 1;
        for (i=0, i<power, i++)  {
        result = result * value;
}
return result;


}
```

```
/************ This function computes power of an integer************************/

int pwr(value, power) {

        int i:

        int result =1;

        for (i=0; i<power, i++) {

        result = result * value;

}



return result;



}



/********************** This function sums phases for each proton**************/

int sum_phase (void) {

        int i, j;

        for (i=0; i< NUM_PROTONS; i++) {

        cumulativephase [i] = 0;
```

```
        for (j=0; j<ceil (TE/dt); j++) {

        cumulativephase [i] = cumulativephase[i] + phasearray [i][j];

        }

}



return 0;









/************* To calculate the real part of proton phases******************/

int get_cos_array(void) {

        int i;

        for (i=0, i< NUM_PROTONS; i++) {

        cosarray[i] = cos(cumulativephase[i]);

        }
```

```
return 0;




}



/****** To calculate all imaginary components of  proton phases****************/

int get_sin_array(void) {

        int i;

        for (i=0, i< NUM_PROTONS; i++) {

        sinarray[i] = sin(cumulativephase [i]);

}



return 0;



}
```

```
/************************To sum all  real components of proton phase**********/

int sum_cosarray(void)  {

        int i;

        cos_sum  = 0;

        for (i=0, i< NUM_PROTONS; i++) {

        cos_sum = cos_sum + cosarray[i]

}



return 0;



}



/****************To sum all imaginary components of proton phases***********/



int sum_sinarray(void) {

        int i;
```

```
        sin_sum =0;

        for (i=0; i< NUM_PROTONS, i++) {

        sin_sum = sin_sum + sinarray[i]

        }


return 0;



}

/********** COMPUTATION*****************************************/


int main(void) {


/****************** Seed random number generator ******************/

srand( (unsigned)time(NULL ) ) ;

srand48( (unsigned) time (NULL) );


/**************Initialize Variables*************************************/
```

```
int offset = ceil(LENGTH/2);

double mean_rad= MEAN_RADIUS

double numprotons= NUM_PROTONS;



/*Call subroutines to simulate monte carlo  random walk*/

builduniverse (mean_rad);

printf (“Model constructed \n”);

pickstart(offset, mean_rad);

walksim(offset);

printf(“Simulation complete\n”);



sum_phase();

get_cos_array();

get_sin_array();

sum_cosarray();

sum_sinarray();
```

```
/*Calculate T2 VALUE */

double signal = (1.0/numprotons) * sqrt(pwrf(cos_sum,2) + pwrf(sin_sum,2));

double R2 = -log(signal) * 1000 / TE;

double T2 = 1/R2;

printf("T2",T2);



}



/* END */
```